The Pennsylvania State University
The Graduate School

DIE COMPACTION SIMULATION: SIMPLIFYING THE APPLICATION OF A COMPLEX CONSTITUTIVE MODEL USING NUMERICAL AND PHYSICAL EXPERIMENTS

A Thesis in
Engineering Science and Mechanics
by
Gautam S Wagle

Submitted in Partial Fulfillment
of the Requirements
for the Degree of

Doctor of Philosophy

December 2006

The thesis of Gautam S Wagle was reviewed and approved* by the following:

Renata S. Engel
Professor of Engineering Science and Mechanics
Thesis Advisor, Chair of Committee

Randall M. German
Professor of Engineering Science and Mechanics
Brush Chair Professor in Materials

Joseph L. Rose
Paul Morrow Professor of Engineering Science and Mechanics

E. Amine Lehtihet
Professor of Industrial and Manufacturing Engineering

David J. Green
Professor of Ceramic Science and Engineering

Judith A. Todd
Head of the Department of Engineering Science and Mechanics
P. B. Breneman Department Head Chair

*Signatures are on file in the Graduate School.

Abstract

The die compaction process is a rapid net-shape manufacturing process that yields low strength parts which are then sintered to create a functional part. The sintering stage induces shrinkage inversely proportional to the density of the part and distortion if density gradients are present. For an accurate description of the final shape and size, the amount of shrinkage and distortion must be anticipated and incorporated into the original tool design. Numerical modeling tools can be used to develop protocols to attain desired compact properties.

The die compaction process is a complex process as the material undergoes particle rearrangement followed by plastic deformation. Modeling the process requires the use of a complex material model. The modified Drucker-Prager "cap" model can describe the loose powder response and the particle deformation under compaction loads. This research looks at simplifying the application of a numerical finite element model defined using this complex model. The significance of the parameters that define the material model on the results has been determined using a robust sensitivity analysis technique. The results from the analysis have been used to identify the critical parameters for density predictions. Since the recommended testing procedures used to characterize the material parameters are expensive and difficult to perform, alternative testing methods have been investigated for ease in industrial application. A testing protocol using a test method proposed by Coube and Riedel (2000) and a technique proposed in this research has been developed for characterizing the material parameters for the "cap" model.

The protocol has been applied for characterizing two commonly used metal powders for die compaction applications: a water atomized A1000C iron powder and a water atomized 316L stainless steel powder. A numerical finite element model with the characterized parameters has been verified for application to predict density gradients in a die compacted part by comparing the numerically predicted density distribution to the density field obtained from physical measurements. The results of the verification establishes a good predictive capability of the numerical model and the testing protocol developed in this research.

Table of Contents

List of Figures

List of Tables

List of Symbols

A	Area of cross-section
α	Transition parameter
α_1	Positive material constant for Drucker-Prager yield function
β	Material angle of friction
D	Diameter of cylindrical specimen
d	Material cohesion
$d\varepsilon_{ij}^{pl}$	Incremental plastic strain vector
$d\sigma_{ij}$	Incremental stress vector
E	Modulus of Elasticity
ε_{vol}^{pl}	Volumetric plastic strain
$\varepsilon_{vol}^{pl}\|_0$	Initial volumetric plastic strain
$\epsilon_{\theta\theta}\|_{r=r_o}$	Hoop strain at outer die wall
F_c	Failure load in uniaxial compression
F_{axial}	Axial load on thick-walled cylinder
J_1	First stress invariant
J_{2D}	Second stress invariant of the deviatoric stress
K	Ratio of stress in triaxial tension to flow stress in triaxial compression

k	Positive material constant for Drucker-Prager yield function
λ	Positive factor of proportionality (Flow rule)
P	Failure load for Brazilian disk test
p	Equivalent pressure stress
$p_a(\varepsilon_{vol}^{pl})$	Volumetric plastic strain-driven hardening law
p_b	Hydrostatic compression yield stress
p_i	Internal radial pressure
p_0	Initial isotropic state of stress
Q	Plastic potential function
q	Deviatoric stress
R	Cap eccentricity parameter
r_i	Inner radius of thick-walled cylinder
r_o	Outer radius of thick-walled cylinder
ρ	Density (or Relative density)
ρ_0	Initial relative density
s_{ij}	Deviatoric stress tensor
σ_c	Compressive failure stress
σ_{oct}	Hydrostatic stress
σ_r	Radial stress
σ_t	Tensile failure stress
σ_z	Axial stress
T	Height of cylindrical specimen
t	Deviatoric stress measure

Acknowledgments

First of all, I would like to express my deepest gratitude to my advisor, Dr. Renata S. Engel, for her guidance. Her constant motivation and understanding in the field of Finite Element analysis were invaluable for my doctoral research. I will always be indebted to her for the amount of time she spent discussing the problem in-spite of her busy schedule spanning various appointments. I would also like to thank Dr. Randall M. German for sharing his knowledge in the field of powder metallurgy and highlighting the industrial challenges. I sincerely thank my colleagues and the staff members of the CISP lab especially Ravi Kumar Ennetti, Ravi Bollina, Guneet Sethi and Tracy Potter for their help furnished during the course of my research work.

I am grateful to the National Science Foundation (NSF) for supporting this research work under Grant No. 0200554 - Protocol Development for Net Shape Powder Metal Part Production Via Cold Compaction.

I want to acknowledge the support of my friends Subash, Ram, Anup, Ramesh, Garg, Viren and all other friends from the cricket club for keeping me sane through my doctoral studies. Least but not the least I would like to thank my family for providing me with their unwavering moral support. I would like to thank my aunt's family for being there as a family here in the US and giving me an opportunity to pursue graduate studies. I dedicate this thesis to my grandfather, Shri Kashinath P. Nadkarni.

Chapter 1

Introduction

1.1 Powder Die Compaction

Powder metallurgy is a widely used net shape manufacturing technique in the metalworking industry. Uniaxial die compaction is the most typical form of consolidation process in powder metallurgy. In this process, loose powder particles are compressed in a die cavity by the application of pressure to form a solid "green" part of relatively high density that conforms to the shape of the cavity. The pressure is applied along one axis whereas the cavity into which the powder is pressed gives it a lateral constraint as shown in Figure 1.1. This process is extremely fast and has great potential for mass production of parts such as those in the automobile industry.

The higher the pressure applied during compaction, the higher is the density of the green part. With standard tool steel or cemented carbide dies and punches, densities close to 90% of the theoretical are possible in green parts without tool damage. This modest density, modest strength green part is fragile and may break upon impact and therefore needs to be sintered in a furnace under controlled atmosphere at a temperature approximately 80% of the melting temperature of the material to attain the desired strength. During sintering, the powder particles bond together. This particle bonding can result in dimensional distortion of the green part. It has been shown that the dimensional change is inversely dependent on the density of the green part (German, 1994); therefore density gradients if present in the green part will produce shape distortion.

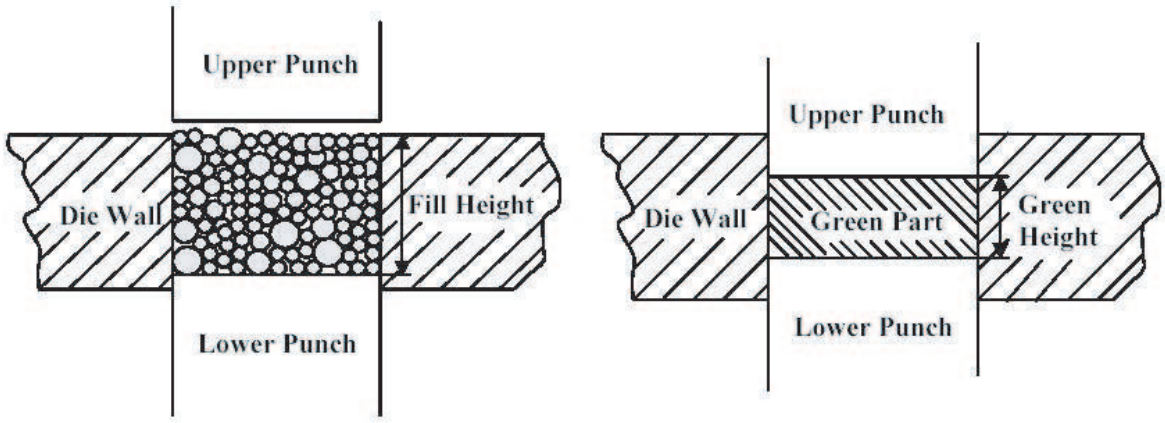

Figure 1.1. Schematic of a uniaxial die compaction process

During compaction, the axial forces applied by the compaction load result in radial forces being generated at the die walls. In spite of high degrees of surface finish on the die wall and the punch faces, friction exists between the powder and the tool components. These frictional forces result in the applied pressure along the die wall to decrease along the depth of the powder column. A differential and non-uniform pressure distribution during the compaction process produces a density gradient in the green parts. During the subsequent sintering process, these density gradients lead to non-symmetrical dimensional changes. Regions of high density near the punch faces exhibit small dimensional changes whereas lower density regions away from the punch faces exhibit larger dimensional change. This results in a loss of dimensional precision on the finished component. Hence, in order to ensure uniformity in dimensions and properties after sintering, variations in green density need to be minimized and understood.

The effects of friction during compaction can be reduced by adding lubricants to the powder or the die-wall surface thereby minimizing density gradients. The use of a double action or a floating die press is another means of reducing the density gradients in tall and slender green parts as pressure is more uniformly distributed in the compact. However friction cannot be eliminated completely and hence accurate prediction of density gradients is significant in predicting the final compact properties. Numerical simulation of the die compaction process provides a cost-effective means of predicting the density profile of the green part depending on the processing parameters.

1.2 Necessity of the Research

One of the main goals of research in powder metallurgical industrial production is to develop protocols to attain desired compact properties and to establish tolerances in a traditional compaction and sintering process to eliminate the need for additional machining operations. Numerical methods such as the Finite Element Method (FEM) and the Discrete Element Method (DEM) are typical tools used to simulate the processes. Additionally they can provide an efficient method to establish the desired protocols rather than using trial and error type approaches. Hence developing protocols via computational methods to establish dimensional tolerances, requires an accurate simulation of the die compaction process and an appropriate material model.

During the compaction process, the material changes from a loose aggregate of discrete particles varying in shape and size to a low strength skeleton structure that behaves like a continuum. Hence modeling of a powder subjected to uniaxial die compaction can be achieved either from a micromechanical approach to understand and predict particle interactions and deformations, or a continuum approach to predict response in a system of particles. The latter approach is favored for most industrial applications of die compaction modeling.

Understandably, the behavior of the representative continuum material can be described by models developed from soil research. Soils have been studied in great detail in the field of geomechanics and their mechanical behavior under compacting loads has been well formulated. There are many soil constitutive models such as the original Drucker-Prager model (Drucker and Prager, 1952), the modified Drucker-Prager "cap" model (Drucker et al., 1957) and the Cam-clay model (Roscoe et al., 1925) that can be used to describe the behavior of the material undergoing compaction. Previous studies investigating the applicability of these models to the compaction process for iron and stainless steel powders (Wagle et al., 2000, He et al., 2001), illustrate the importance of a model that can describe the loose powder response and the particle deformation.

The use of models for industrial problems is only as effective as the ability to determine the material model parameters. Parameter specification presents a challenge as the complexity of the material model increases. This research looks at developing a numerical tool using the Drucker-Prager "cap" model which is commonly used to describe the material behavior of a metal powder undergoing compaction to predict the density distribution in a green part. Furthermore, the research focuses on balancing the use of this complex material model with appropriate simplification to obtain the material model parameters.

1.3 Research Objectives

Industrial application of a numerical tool to accurately predict the density gradients developed during compaction requires an accurate description of the material model used to simulate the process. This requires a good understanding of the consolidation phase of particulate material models. The current research focuses on understanding the yield behavior of the modified Drucker-Prager "cap" model with regards to its application for the compaction process. The overarching objective of this research has been to develop a process for applying the Drucker-Prager "cap" model to predict density field during die compaction. As a result, this research focuses on determining efficient and effective methods for establishing parameters, and applying the parameters in a finite element analysis. A set of numerical and simple physical experiments has been identified to describe the physical response of particulate materials under die compaction loads. In combination, these experiments determine the constitutive model parameters. The procedure for determining the system parameters and the application of a numerical finite element model to determine the density distribution in a green part for various powder metals can be used in industrial applications. The overarching objective of the research has been met by satisfying the following intermediate objectives.

- Understand the modified Drucker-Prager "cap" material model particularly the yield cap surface as it relates to a metal powder undergoing compaction. [Chapter 2]
- Identify the significant parameters used to define the compaction response of the material. [Chapter 3]

- Develop numerical and simple physical experiments to determine the identified parameters. [Chapter 4, 5]
- Apply the material parameter characterization technique to two powder metals. [Chapter 4, 5]
- Refine the die compaction simulation to provide a confident prediction of the density gradients and validate the numerical model using experimental density data. [Chapter 6]
- Develop a test protocol for characterizing material model parameters for any powder material.

1.4 Organization of the Thesis

Chapter 2 reviews the original Drucker-Prager soil constitutive model and its development into the modified Drucker-Prager "cap" model as applied in ABAQUS (2001). The features that make the model suitable for application to simulation of die compaction of metal powders are identified during this review.

Chapter 3 discusses the current understanding of the material model parameters, their significance and characterization. This chapter also includes a variety of statistical numerical studies to refine the focus of the proposed research. It is shown that though the material model is complex as it requires seven parameters to characterize the material behavior under compaction loading, the resulting density field prediction is sensitive to only two of the material parameters. Current methods for determining the parameters are complex, making it inappropriate for industry to apply the model to a wide variety of materials and material systems.

Chapter 4 and 5 present the proposed alternative methods for determining the material parameters of the constitutive model for high strength particulate materials. The results of these experimental methods for different powder systems are also presented. Chapter 4 features the failure surface parameters characterization and chapter 5 features the cap

eccentricity parameter.

The material parameters determined from the simple tests for two metal powders are used to refine the die compaction simulation by comparing the numerically predicted density gradients with experimentally measured density gradients in Chapter 6. Chapter 7 summarizes the research work and concludes with a test protocol for applying the Drucker-Prager "cap" model to predict density gradients in die compacted powder metal parts.

Chapter 2

Material Model for the Powder Compaction Process

2.1 Introduction

Accurate finite element simulation of the powder metallurgy die compaction process requires a well defined material behavior during the process. During the process loose powder particles undergo displacement followed by elastic deformation and then plastic deformation to form a continuum structure with pores. Two types of continuum approaches are usually employed to define the material behavior. The first and the more popular approach for modeling die compaction considers the powder as a granular material with weak cohesive forces. This approach includes constitutive models developed for soil plasticity problems such as the Drucker-Prager "cap" model (Drucker et al., 1957) and the Cam-clay plasticity model (Roscoe et al., 1925). The other approach for modeling powder behavior is to consider the powder as a porous material. This approach is more suitable for high density compacts and sintered part modeling. Examples of material models considered under this approach are the Shima-Oyane model (Shima and Oyane, 1976) and Gurson's model (Gurson, 1977).

This research uses the approach of defining the powder metal as a granular material and the modified Drucker-Prager "cap" model is used to define the constitutive behavior of the material during simulation. Prior to discussing the simulation, a thorough understanding of the development of the model is presented in the following sections.

2.2 The Drucker-Prager Soil Plasticity Model

The original Drucker-Prager soil plasticity model was developed by Drucker and Prager (1952). In this model, the authors proposed to modify the von Mises yield criterion in metal plasticity to study the bearing capacity of soil foundations. While the metal plasticity models are independent of the first stress invariant, particulate materials exhibit the type of behavior characterized by frictional materials in that the strength of these materials depends on the hydrostatic stress. The model assumes that the material will behave elastically up to some state of stress at which yielding occurs. The shear stress required for yielding to occur depends on the cohesion of the material and the normal pressure on the failure surface.

The original Drucker-Prager yield criterion modified the von Mises yield criterion by introducing a dependence on the mean (hydrostatic) stress, p. The Drucker-Prager yield function is given by:

$$f(J_1, J_{2D}) = \sqrt{J_{2D}} - \alpha_1 J_1 - k = 0 \tag{2.1}$$

where J_1 is the first stress invariant ($J_1 = \sigma_{ii} = \sigma_1 + \sigma_2 + \sigma_3$),
J_{2D} is the second invariant of the deviatoric stress, s_{ij} ($J_{2D} = \frac{1}{2} s_{ij} s_{ij}$), and
α_1 and k are positive material constants at each point of the material.

The parameter α_1 modifies the von Mises yield surface (which is plotted in the principal stress space) from an infinitely long cylinder to a cone. The criterion is therefore also called the extended von Mises criterion. For $\alpha_1 > 0$, the Drucker-Prager yield surface is a right circular cone with its axis equally inclined to the co-ordinate axes and its apex in the tension octant in the principal stress space. The failure surface defined by the Drucker-Prager failure criterion in the principal stress space and the meridional (p–q) plane is as shown in Figure 2.1. The parameters α_1 and k physically denote the angle of internal friction and cohesion respectively when plotted in the meridional plane.

While the original proposed Drucker-Prager failure surface is the straight edge of a right

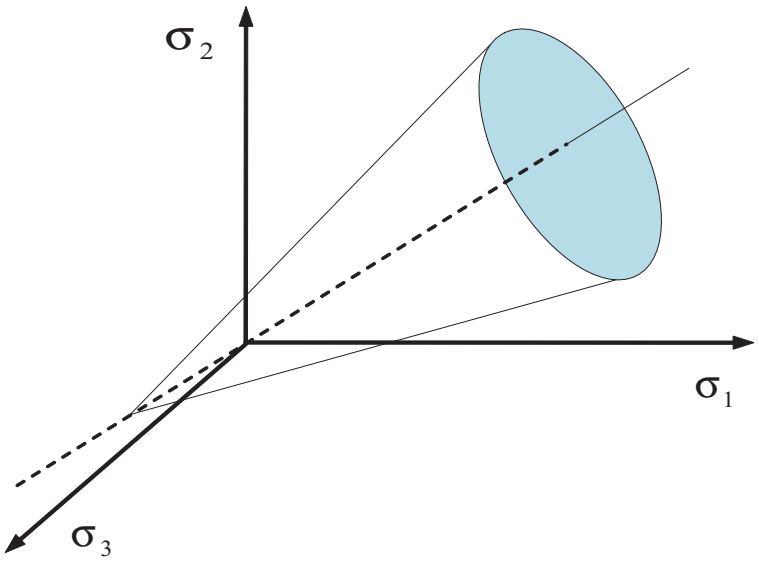

(a) Principal stress space

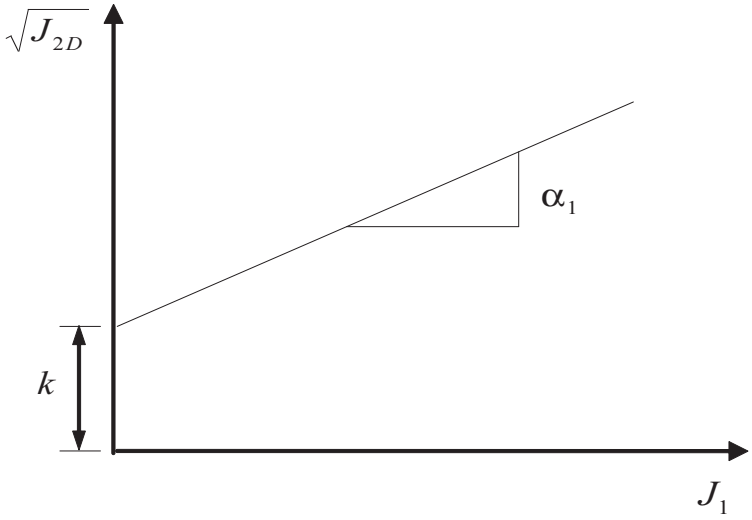

(b) Meridional plane

Figure 2.1. The original Drucker-Prager failure surface

circular cone, some researchers have proposed that at higher stresses, the particulate system behaves as a liquid and its strength approaches the von Mises surface at these stresses. Hence the failure surface can be assumed to be composed of an initial portion of the Drucker-Prager envelope joined smoothly to the subsequent von Mises surface that prescribes the strength of the material at 100% relative density as shown in Figure 2.2.

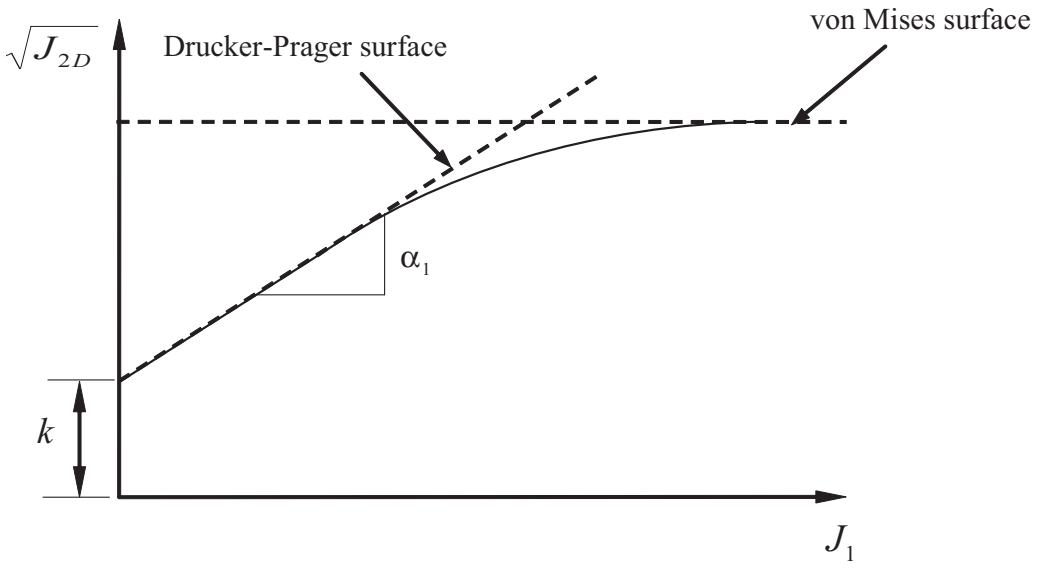

Figure 2.2. Proposed Drucker-Prager failure surface for higher stresses

2.3 Flow Rule

When the state of stress reaches the yield criterion, the material undergoes plastic deformation. A flow rule is prescribed to define the direction of the plastic strain vector. A plastic potential function, Q, is assumed to exist and the incremental strain vectors are assumed to be orthogonal to this function as given by the following expression:

$$d\varepsilon_{ij}^{pl} = \lambda \frac{\partial Q}{\partial \sigma_{ij}} \tag{2.2}$$

where λ is a positive factor of proportionality. This expression is referred to as the normality rule. For some materials, the plastic potential function is assumed to be the same as the yield function. Such materials are said to follow the associative flow rule of plasticity. Substituting the expression for the yield function given by (2.1) in the normality rule (2.2), we get

$$d\varepsilon_{ij}^{pl} = \lambda(\frac{s_{ij}}{2\sqrt{J_{2D}}} - \alpha_1 \delta_{ij}) \tag{2.3}$$

where s_{ij} is the deviatoric stress tensor. From equation (2.3), it is noted that the plastic rate of cubical dilation is

$$d\varepsilon_{ii}^{pl} = -3\alpha_1\lambda \tag{2.4}$$

As seen, the volumetric component is negative indicating that shear failure along the Drucker-Prager failure surface is accompanied by volume increase or dilation. However experimental data on particulate materials suggests that dilation predicted by the Drucker-Prager model is usually larger than that found in practice. For some materials, deformation occurs at constant volume or is accompanied by a decrease in volume. This discrepancy may be due to an invalid assumption of the normality rule. But discarding the normality rule would imply a material that violates the stability postulates proposed by Drucker (1950). Another reason for the discrepancy may be because the particulate material may not behave as a perfectly plastic body, an underlying assumption of the failure surface definition. This is the basis of the modified Drucker-Prager yield criterion which suggests treating the particulate material system as a work-hardening material which could reach the perfectly plastic state. In order to understand the shape of the yield surfaces for a work hardened material, it is essential to understand the concept of work hardening and what it implies.

2.4 Work Hardening and Its Implications (Desai and Siriwardane, 1984)

The concept of work hardening is introduced to explain the behavior of material under plastic loading beyond its yield criterion but prior to failure. If an external agent causes added stresses on a body, work hardening of the material ensures that the material remains in stable equilibrium by absorbing the work done by these added stresses on the strains that result. Work hardening is governed by the following two postulates:

1. During the application of stresses, the work done by the external agency will be positive. This is expressed mathematically as:

$$d\sigma_{ij}d\varepsilon_{ij} > 0 \tag{2.5}$$

2. Over a cycle of application and removal of stresses, the work done by the external

agency will be zero or positive. This is expressed as:

$$d\sigma_{ij} d\varepsilon_{ij}^{pl} \geq 0 \tag{2.6}$$

In addition to the concept of work hardening, certain conditions need to be satisfied to ensure an appropriate description of the physical process involving plastic deformation. These conditions were formulated by Prager (1949) and are:

1. *Condition of continuity*: Given a state of stress that lies on the yield surface, an infinitesimal change of stress $d\sigma_{ij}$ causes unloading if the stress path is directed towards the interior, loading if the path is directed towards the exterior and neutral loading if the stress path is tangential to the yield surface. The condition of continuity states that neutral loading does not cause any plastic deformations.

2. *Condition of uniqueness*: This condition states that for a given state of a material and a system of infinitesimal increments of surface tractions, the resulting increments of stresses and strains are unique.

3. *Condition of irreversibility*: Since the plastic deformations are irreversible, this condition states that the work done on plastic deformations will be positive.

4. *Condition of consistency*: This condition requires the yield condition to be satisfied as long as the material is in a plastic state.

Based on the above postulates and conditions, we can study what the implications of assuming a work hardening material are on the yield surfaces. Consider a state of stress σ that lies on the yield surface. Consider an infinitesimal increment in stress $d\sigma$ whose stress path is directed towards the exterior of the yield surface as shown in Figure 2.3. The incremental stress can be decomposed into a tangential and a normal component, $d\sigma^{(t)}$ and $d\sigma^{(n)}$ respectively.

Assuming that the relation between the infinitesimal changes of stress and plastic strain is linear, the incremental plastic strain caused by $d\sigma$ will be equal to the vector sum of the incremental plastic strains caused individually by $d\sigma^{(t)}$ and $d\sigma^{(n)}$. By imposing the condition of continuity that requires the plastic strain due to neutral (or tangential) loading to be zero, we find that the incremental plastic strain $d\varepsilon^{pl}$ due to $d\sigma$ is dependent only on the

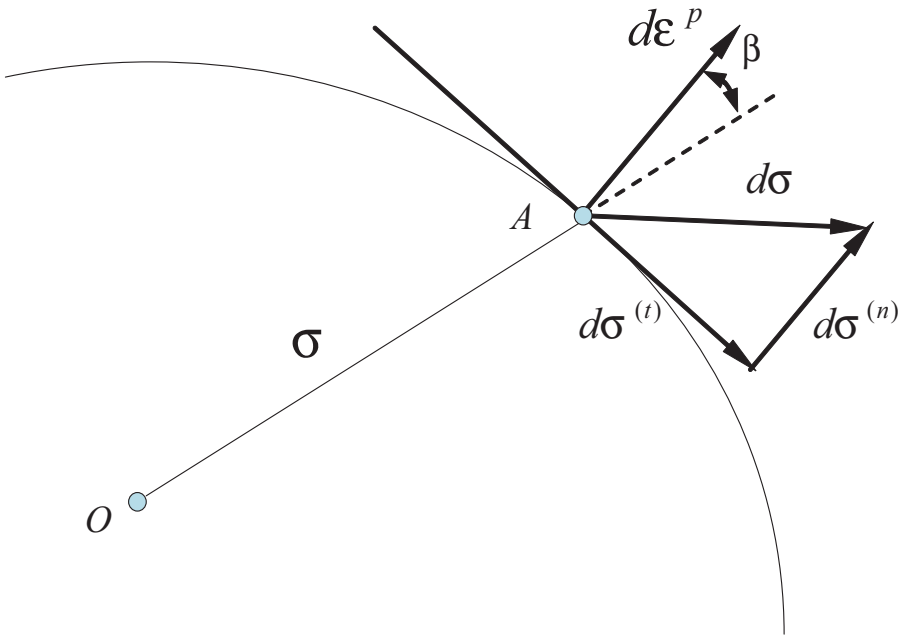

Figure 2.3. Implication of work hardening

normal component $d\sigma^{(n)}$. This implies the normality rule i.e. the incremental strain vector is normal to the yield surface. Thus it is seen that for a work hardened material, the yield function follows the normality rule and ensures that the material is stable.

Another implication of the condition of irreversibility is that the work done due to plastic deformation is positive which is expressed as

$$\sigma \cdot d\varepsilon^{pl} > 0 \tag{2.7}$$

or

$$|\sigma| \cdot |d\varepsilon^{pl}| \cos\beta > 0 \tag{2.8}$$

This means that the radius vector should make an acute angle β with the incremental plastic strain vector. However from the previous discussion, we see that the incremental plastic strain vector is normal to the yield surface. Thus the concept of work hardening and the condition of irreversibility requires the radius vector to make an acute angle with an exterior normal to the yield surface. That is the yield surface has to be convex. In order to describe the behavior of particulate materials as a work hardening material, Drucker et al.

(1957) defined a series of spherical yield surfaces, the simplest convex surface possible. This idea of successive yield surfaces can explain the hardening or consolidation behavior of particulate materials and permit the use of the normality rule of plasticity. This description underlies the criterion commonly referred to as the modified Drucker-Prager "cap" model discussed in the following section.

2.5 Modified Drucker-Prager "Cap"Model

The "cap" model first proposed by Drucker et al. (1957) assumed the particulate material to behave as a work hardening material that may approach the idealized perfectly plastic state. It takes into consideration the fact that many particulate materials experience plastic deformation or yielding prior to reaching the ultimate failure state defined by the Drucker-Prager shear failure surface. The criterion also accounts for plastic deformation under pure hydrostatic loading. In their work, Drucker et al. proposed the yield curve to be approximated by two straight lines described by the Drucker-Prager failure criterion given by equation (2.1) and a circular arc closure corresponding to placing a spherical cap on the open end of the cone as shown in Figure 2.4. The spherical yield surface changes with the hydrostatic pressure to depict work hardening.

If the material is consolidated hydrostatically up to state of stress A and then unloaded, it will behave elastically up to state A and then start experiencing plastic deformations. During successive yielding, the material hardens. When the stress point moves beyond the current yield surface at A, a new yield surface is established at B. The region in which the material now behaves elastically will encompass the sector OBD. The new yield surface at B intersects the Drucker-Prager failure surface at D. The experimentally observed volumetric behavior of particulate materials can be explained by assuming the incremental plastic strain vector to be normal to the cap surface at its point of intersection. In addition, the incremental plastic strain vector needs to be normal to the hydrostatic axis at the point of intersection to ensure that no hardening takes place when the state of stress reaches a point on the yield surface that is locally parallel to the hydrostatic axis since no plastic volumetric changes occur at such a point. This is similar to the critical state concept in which the material does not change in volume when it reaches the critical state. Also the

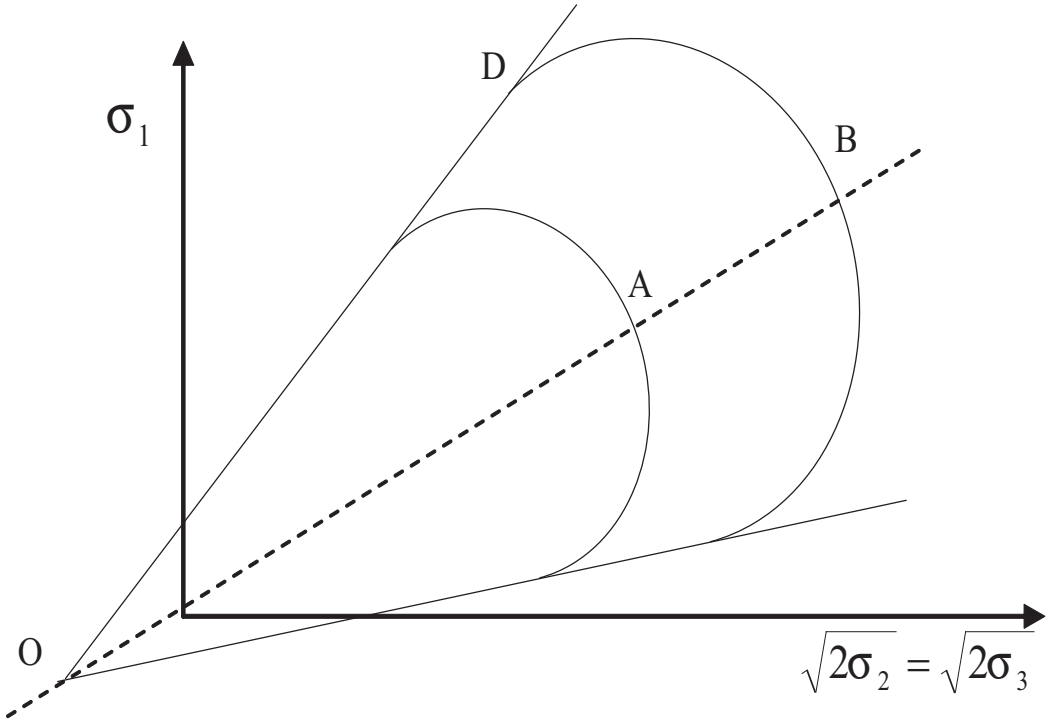

Figure 2.4. Drucker-Prager "cap" yield surfaces

cap yield surface intersects the hydrostatic axis at right angles to guarantee that no shear deformations take place under pure hydrostatic compression.

Drucker et al. (1957) proposed a spherical yield surface, the simplest convex yield surface as required from the concept of work hardening. The shape of these yield surfaces has been assumed to be different by different researchers. The shape of the yield surface for a particulate material needs be determined from appropriate laboratory tests. Cap models suggested by DiMaggio and Sandler (1971) and Lade (1977) suggest a series of elliptical yield surfaces. A simple elliptical yield function referred to as the modified Drucker-Prager yield function given by Chen (1994) is expressed as:

$$f(J_1, J_{2D}, k_1) = (J_1 - l)^2 + R^2 J_{2D} - (x(k_1) - l)^2 = 0 \tag{2.9}$$

where R is the aspect ratio of the ellipse, l is the location of the intersection of the Drucker-Prager surface and the cap, and x is a hardening parameter and a function of k_1 that defines the deformation history. This parameter k_1 is usually taken as the volumetric plastic strain.

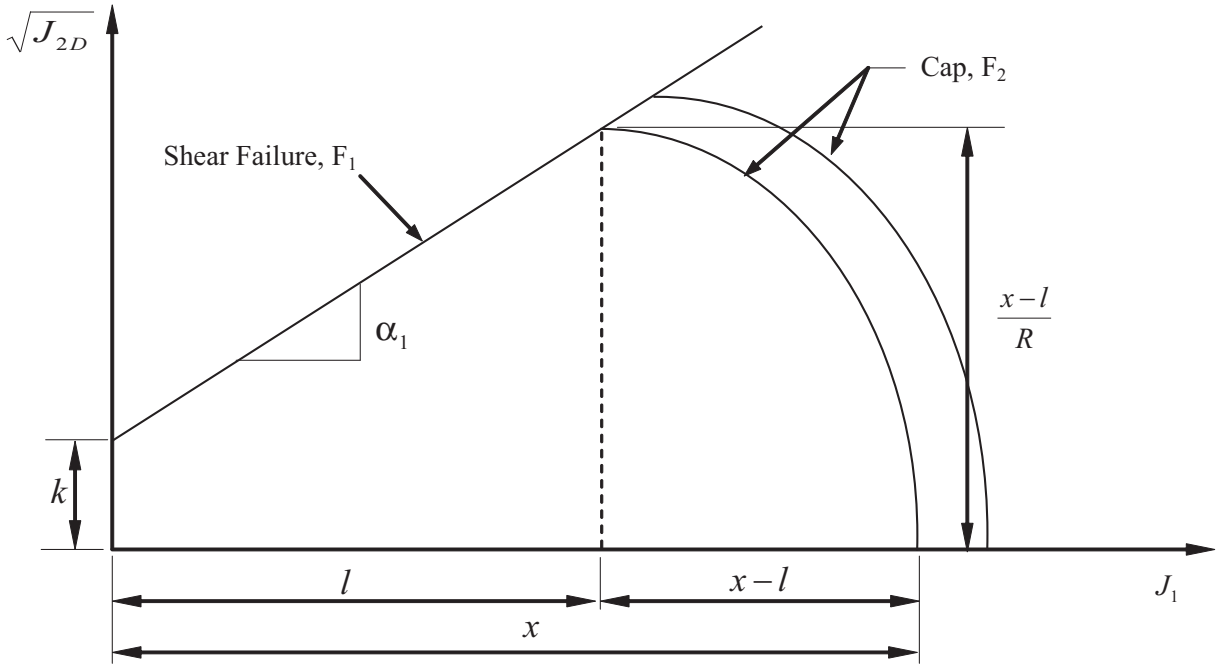

Figure 2.5. Modified Drucker-Prager "cap" model

Thus the yield surface defined by the hardening parameter represents a locus of points with the same volumetric plastic strains. A series of cap yield surfaces defined by equation (2.9) are shown in Figure 2.5 that intersect the original Drucker-Prager failure surface as per the assumptions.

The Drucker-Prager "cap" model as defined in ABAQUS is described and the model parameters are identified along with the experimental methods to determine them for a particulate system in the following chapter.

Chapter 3

Constitutive Model Parameters

3.1 Introduction

The applicability of a constitutive model to predict the behavior of a structure under certain physical conditions depends significantly on the ability to experimentally determine the parameters that define the model for a particular material. Different experimental techniques are used to determine the parameters for a certain model under the applicable physical condition. The Drucker-Prager "cap" model was developed by researchers interested in problems in soil mechanics. Hence the experimental methods used to determine the parameters that define the model have evolved from tests done on soils to study their behavior under uniaxial, biaxial or multiaxial loading. A detailed look at the various experimental testing methods used to characterize a Drucker-Prager "cap" model is carried out in this chapter. The parameters defining the model are identified and the current existing testing methods for each of these parameters are discussed. A parameter sensitivity analysis to determine the parameter that affects the density gradient most significantly is discussed to focus the research, particularly to determine physical and numerical experimental procedures to determine these parameters.

3.2 "Cap" Model in ABAQUS

In ABAQUS (2001) the modified Drucker-Prager "cap" model is characterized by three principal segments: a pressure-dependent Drucker-Prager shear failure surface F_s, a series

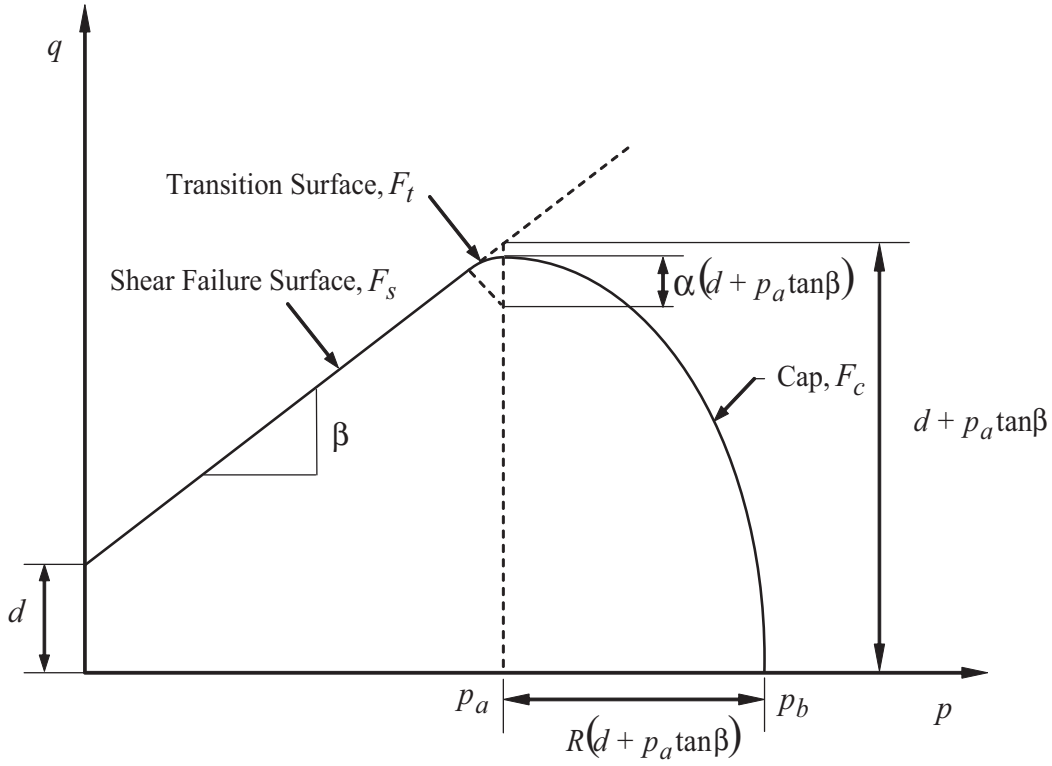

Figure 3.1. Surfaces defined by the modified Drucker-Prager "cap" model

of compression yield surfaces F_c, and a transition surface F_t. Volumetric strain hardening is defined by moving the cap along the hydrostatic axis. The purpose of the transition surface is to remove any singularities during numerical computations when moving from the yield surface to the failure surface. Figure 3.1 shows the surfaces defined by the "cap" model described in ABAQUS (2001) in the $p - q$ $(J_1/3 - \sqrt{3J_2})$ plane.

The three surfaces are described by:

$$F_s = t - p\tan\beta - d = 0 \tag{3.1}$$

$$F_c = \sqrt{[p - p_a]^2 + [\frac{Rt}{(1 + \alpha - \alpha/\cos\beta)}]^2} - R(d + p_a \tan\beta) = 0 \tag{3.2}$$

$$F_t = \sqrt{[p - p_a]^2 + [t - (1 - \frac{\alpha}{cos\beta})(d + p_a \tan\beta)]^2} - \alpha(d + p_a \tan\beta) = 0 \tag{3.3}$$

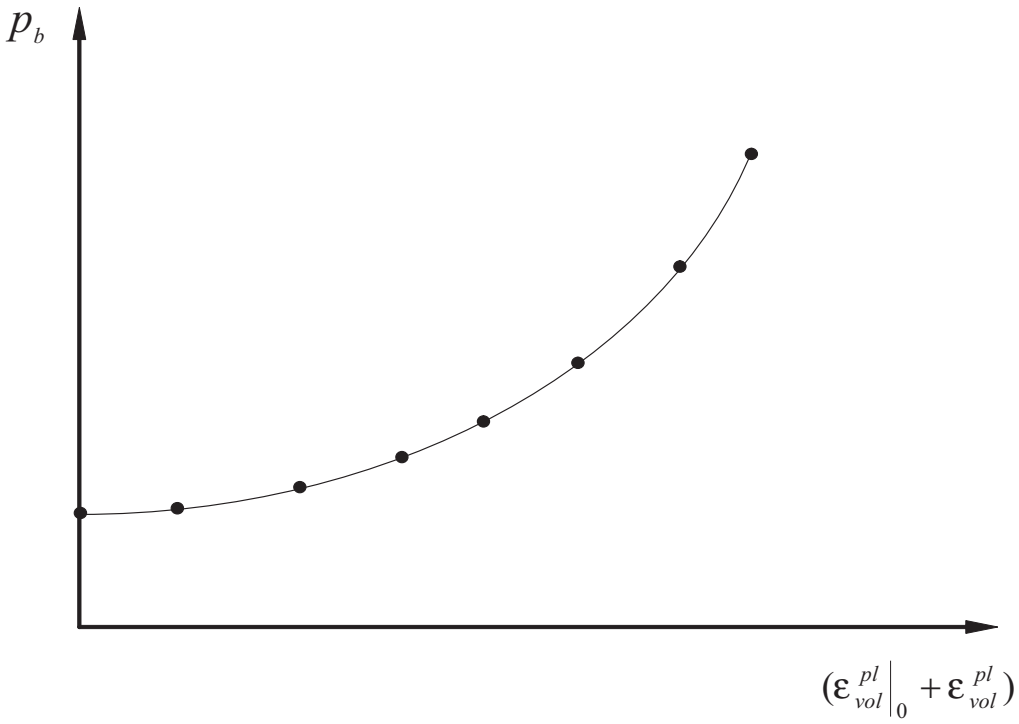

Figure 3.2. Cap Hardening

where β is the angle of internal friction,
d is the material cohesion,
t is the deviatoric stress measure,
p is the equivalent pressure stress,
R is the cap eccentricity parameter,
$p_a(\varepsilon_{vol}^{pl})$ represents the volumetric plastic-strain-driven hardening, and
α is the transition parameter.

The hardening law is defined by a piecewise linear function relating the hydrostatic compression yield stress, p_b, to the volumetric plastic strain ε_{vol}^{pl} as shown in Figure 3.2. $\varepsilon_{vol}^{pl}|_0$ is the initial volumetric plastic strain beyond which the the work hardening yield surfaces are defined.

The evolution parameter, p_a is related to p_b by

$$p_a = \frac{p_b - Rd}{(1 + R\tan\beta)} \tag{3.4}$$

3.3 "Cap" Model Parameters

The Drucker-Prager "cap" model parameters can be identified as characterizing two different aspects of the cap:

- The plasticity parameters that describe the shape of the shear failure surface and the yield caps. The plasticity parameters can be further differentiated into two categories:
  - *Failure surface parameters*: These parameters define the shape of the shear failure surface. The two failure surface parameters are the material cohesion or the intercept of the failure surface with the deviatoric stress axis, d, and the angle of internal friction or the slope of the failure surface with the hydrostatic axis, β.
  - *Yield surface parameters*: These parameters define the location and shape of the yield caps or loci of constant volumetric strain. The yield surface parameters comprise the aspect ratio of the elliptic caps, R, and the location of the intersection of the cap surface with the shear failure surface.
- The work hardening parameters that describe the evolution of the yield caps with compaction The location of intersection of the cap surface with the hydrostatic axis is prescribed by defining the work hardening parameter in terms of pairs of the hydrostatic compression yield stress, p_b, and volumetric plastic strain during the consolidation process, ε_{vol}^{pl}.

The parameters are determined by subjecting a specimen made of a desired material to loading conditions that would ensure that the material is loaded to failure under shear as it undergoes compaction. Some of the originally developed experimental methods to determine these parameters for soils along with any specifications are discussed in the following

sub-sections. Applications of these techniques for metal and ceramic powders are well documented in literature (Zeuch et al. (2001), Aydin et al. (1996), Pavier and Doremus (1999), Brown and Abou-Chedid (1994)).

3.3.1 Failure Surface Parameters

The failure surface parameters can be determined by performing a set of two or more triaxial compression tests. These tests determine the strength and the stress-strain relationships of a cylindrical specimen made of particulate material. Specimen are isotropically consolidated and sheared in compression at a constant rate of axial deformation. The experimental equipment setup and procedure for the triaxial compression test follows the ASTM Standard D4767-95 (1995). Figure 3.3 shows a schematic of the triaxial test apparatus.

The test apparatus consists of an axial loading device capable of providing a prescribed rate of axial strain on the specimen by means of a piston. The loading device is equipped with an axial load measuring device. A deformation indicator is used to measure the vertical deformation of the specimen by measuring the travel of the piston. A triaxial compression chamber consisting of top and base plates separated by a cylindrical pressure vessel is used to house the cylindrical specimen during testing. The chamber is constructed of any material capable of withstanding the applied pressures. Usually a transparent material is used to allow observation of the specimen during testing. The chamber is outfitted with pressure controlling and measuring devices as well as a volume measuring device to measure the volumetric strain.

The specimen tested in triaxial compression is cylindrical with a minimum diameter of 33 mm. The average height-to-diameter ratio recommended as per standard is between 2 and 2.5. The test begins with a consolidation phase which allows the specimen to reach equilibrium at the effective consolidation pressure. The axial load piston is lowered and brought in contact with the specimen and the reading of the deformation indicator is recorded. After recording, the piston is raised a small distance and locked in place. The chamber pressure is then increased until it reaches the desired effective consolidation pressure. The specimen is then allowed to consolidate and the volume readings are recorded

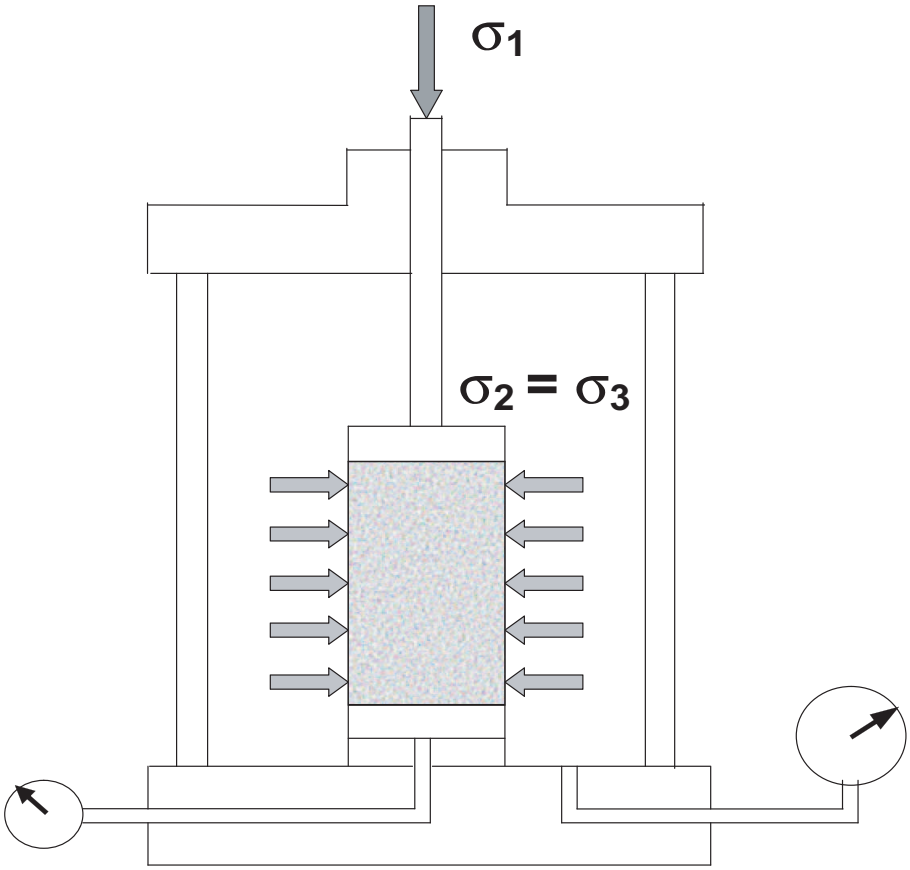

Figure 3.3. Schematic of triaxial test apparatus

at increasing intervals of time. After an initial time period the piston is allowed to contact the specimen cap and the corresponding axial deformation is also measured along with the volume readings for the time increments. Consolidation is allowed to continue for at least one overnight period after 100% primary consolidation has been achieved.

Once consolidated, the specimen is then axially loaded at a constant confining pressure to cause shear failure. The axial load piston is brought in contact with the specimen and proper seating and alignment of the specimen with the piston is verified to prevent the application of a lateral force on the piston. An axial load is applied to the specimen at a desired rate of axial strain. The load and the deformation of the specimen is recorded at increments of strain to define the stress-strain curve until the material undergoes shear. After shear is completed, the axial load is removed and the pressure in the triaxial cham-

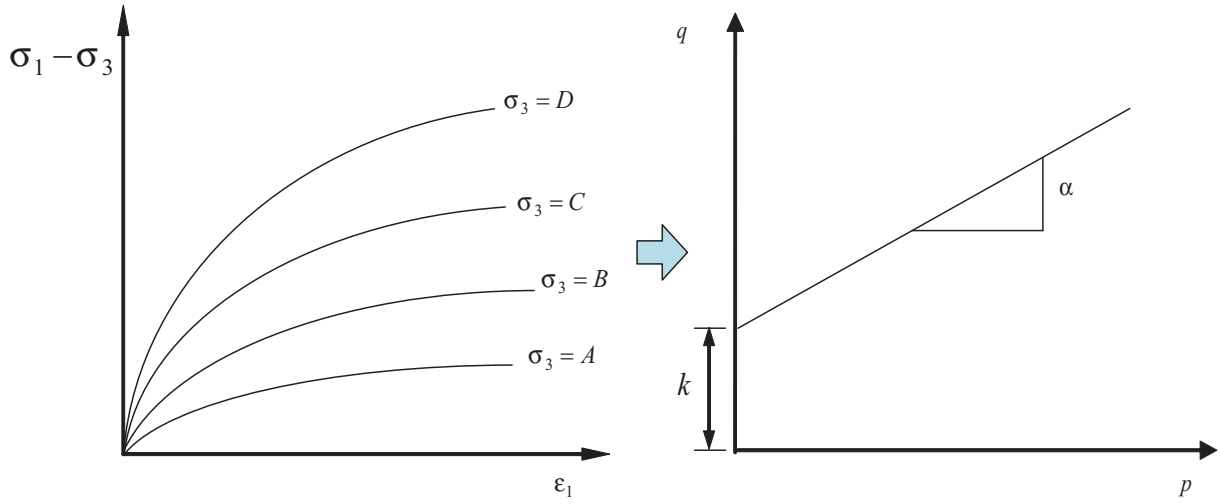

Figure 3.4. Results of a set of triaxial compression tests

ber is reduced to zero. The specimen is removed from the chamber and its size is measured.

In order to plot the shear failure line, a minimum of two triaxial compression tests (i.e tests at two consolidation pressures) are sufficient. However usually the test is carried out at more than two consolidation pressures to get a better fit and reduce errors. Figure 3.4 shows the typical results plotted from a triaxial compression test at different consolidation pressures ($\sigma_3 = A, B, C, D, \ldots$) in the form of deviator stress against axial strain, ε_1, and the shear failure surface plotted in the meridional plane by determining the failure stresses.

3.3.2 Yield Surface Parameters

The cap eccentricity parameter (aspect ratio of the elliptic yield surfaces) is determined by a true triaxial compression test. It allows for the application of different stresses in the three orthogonal directions allowing for any loading path to be followed in the three-dimensional stress space. No standard exists for the true triaxial compression test. The parameter can be determined by using a cylindrical triaxial compression test described in the previous section with more care to obtain different loading paths leading to consolidation without shear

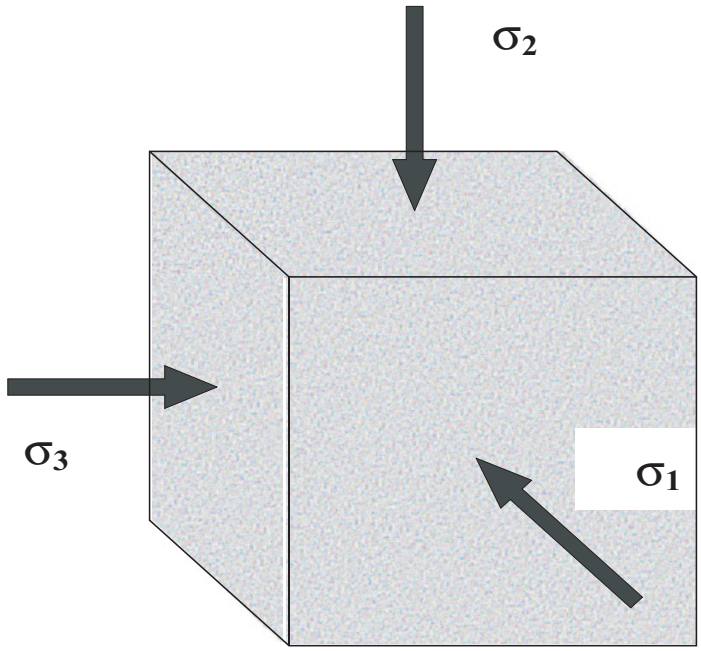

Figure 3.5. Schematic of a true triaxial test loading for cubical specimen

of the specimen. The recommended testing device is a cubical triaxial tester that allows for independent normal loading to be applied in the three principal directions. Figure 3.5 shows a schematic of a true triaxial test loading condition for a cubical triaxial tester.

The specimen powder is loaded into a flexible holder. The test is carried out with the application of different stresses in the three orthogonal directions to allow consolidation of the specimen without shear. The three resulting principal stresses and the three principal logarithmic strains are measured during consolidation. The bulk densities and the corresponding stress states are then calculated during consolidation. Since the initial mass of powder poured into the cubical cavity is known, the relative density, ρ, is easily calculated for any deformation state. At each value of ρ obtained from the different stress states, the equivalent pressure stress, p, and deviatoric stress measure, q, are calculated as:

$$p = \frac{-1}{3}(\sigma_1 + \sigma_2 + \sigma_3) \tag{3.5}$$

$$q = \sqrt{\frac{1}{2}[(\sigma_1 - \sigma_2)^2 + (\sigma_2 - \sigma_3)^2 + (\sigma_1 - \sigma_3)^2]} \tag{3.6}$$

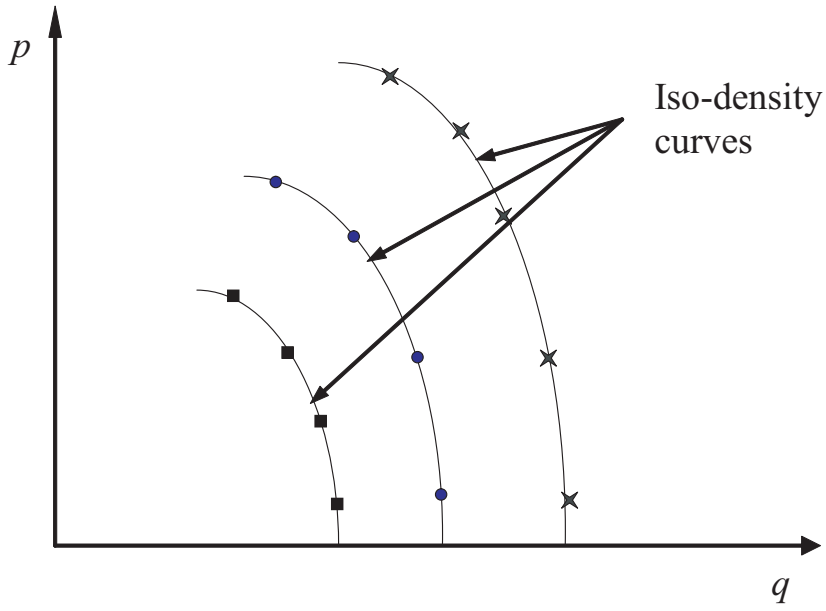

Figure 3.6. Iso-density curves representing Drucker-Prager yield caps in the $p-q$ plane

Using all of the stress-strain curves obtained from the triaxial compression experiments, values of $p-q$ at different densities are plotted to get yield surfaces or loci of constant volumetric strain (iso-density curves) as shown in Figure 3.6. The cap eccentricity parameter, R, is then determined as the aspect ratio of the best fit ellipse through these points. The intersection of the yield caps with the shear failure surface plotted for parameters can be obtained from plotting the failure surface with the parameters determined from the tests described in the previous section.

3.3.3 Hardening Parameter

The hardening parameter is used to define the hardening law or the evolution of yield surfaces ("caps") with increasing volumetric strains. As explained earlier, yield surfaces are loci of constant volumetric strain. The hardening law is defined by a piecewise function relating the hydrostatic compression yield stress i.e. the intersection of the yield surface with the hydrostatic axis, p_b, and the volumetric plastic strain, ε_{vol}^{pl}. The hardening law is usually determined by a hydrostatic compression test (also known as isotropic triaxial compression test) in which the specimen is consolidated by loading it on a stress path along

the space diagonal in the principal stress space with no shear. The test can be performed by using either a cylindrical or a cubical triaxial test device explained in the previous sections.

The hydrostatic compression test begins with the specimen at an initial isotropic state of stress ($p_0 = \sigma_0$). The corresponding physical state is defined by initial relative density ρ_0. The specimen is then consolidated by loading it in increments of hydrostatic stress i.e. by applying equal increments of stress in the three orthogonal directions in a cubical triaxial tester. The mean (hydrostatic) stress is measured as the stress applied on each face of the cubical triaxial tester. The corresponding volumetric strain is measured for each increment of the hydrostatic stress as the sum of the three principal strains. Typically during a hydrostatic compression test, the specimen is unloaded at various intervals during the test in order to determine the bulk modulus for describing the elastic behavior of the material. A graph is then plotted depicting variation of hydrostatic stress with volumetric strain as shown in Figure 3.7(a). The plot indicates that the specimen was unloaded twice during the test. The hardening law can then be defined as a piecewise function of the volumetric strain by fitting a function to the plotted data as shown in Figure 3.7(b).

Loading high strength particulate material specimens hydrostatically can be difficult and the set-up expensive. An alternative testing method to determine the hardening law for such materials is to instead load the material in a rigid die under compaction loads. Figure 3.8 shows a schematic of a uniaxial die pressing set-up. The set-up consists of an axial loading punch with pressure transducers mounted on it to measure the axial stress. Displacement transducers such as LVDT on the punch measure the longitudinal displacement and hence the axial strain or relative bulk density of the specimen.

The radial strain is assumed to be zero since the die is a rigid body and the plastic volumetric strain is assumed to be approximately equal to the total volumetric strain since the elastic part of the volumetric strain is very small for high strength particulate materials. The effect of friction can be decoupled by using lubricants at the die wall or admixed with particulate material. The specimen particulate material is loaded axially and the axial stress and displacement are measured to give a plot of relative density versus the axial stress. The hydrostatic compression stress, p_b, is related to the axial stress, σ_z, by the following expression given by Zipse (1997):

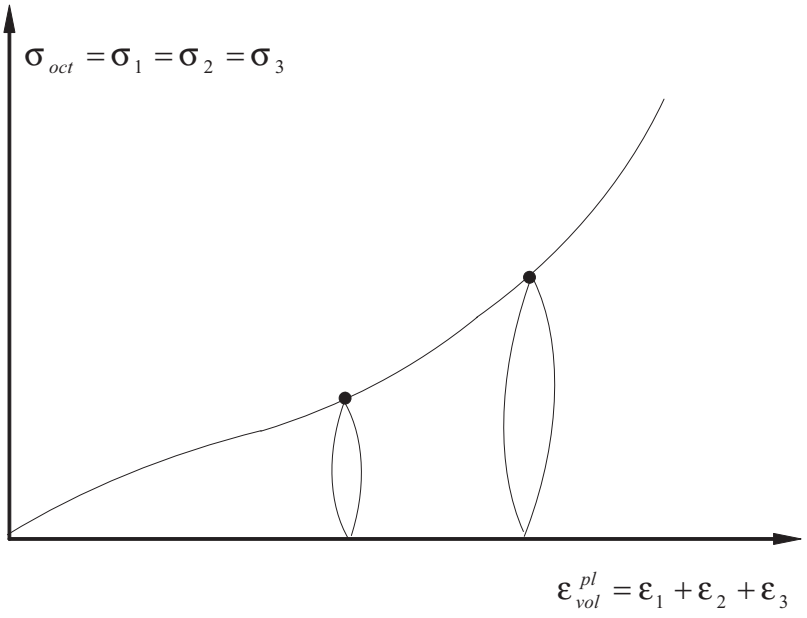

(a) Hydrostatic stress vs volumetric strain

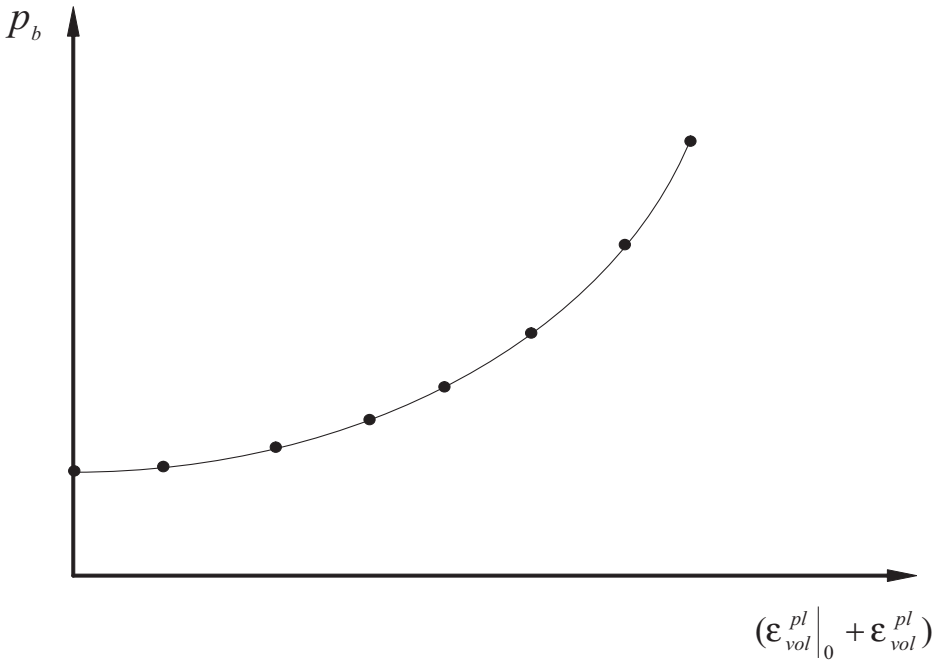

(b) Hardening law

Figure 3.7. Determination of the hardening parameter from hydrostatic compression tests

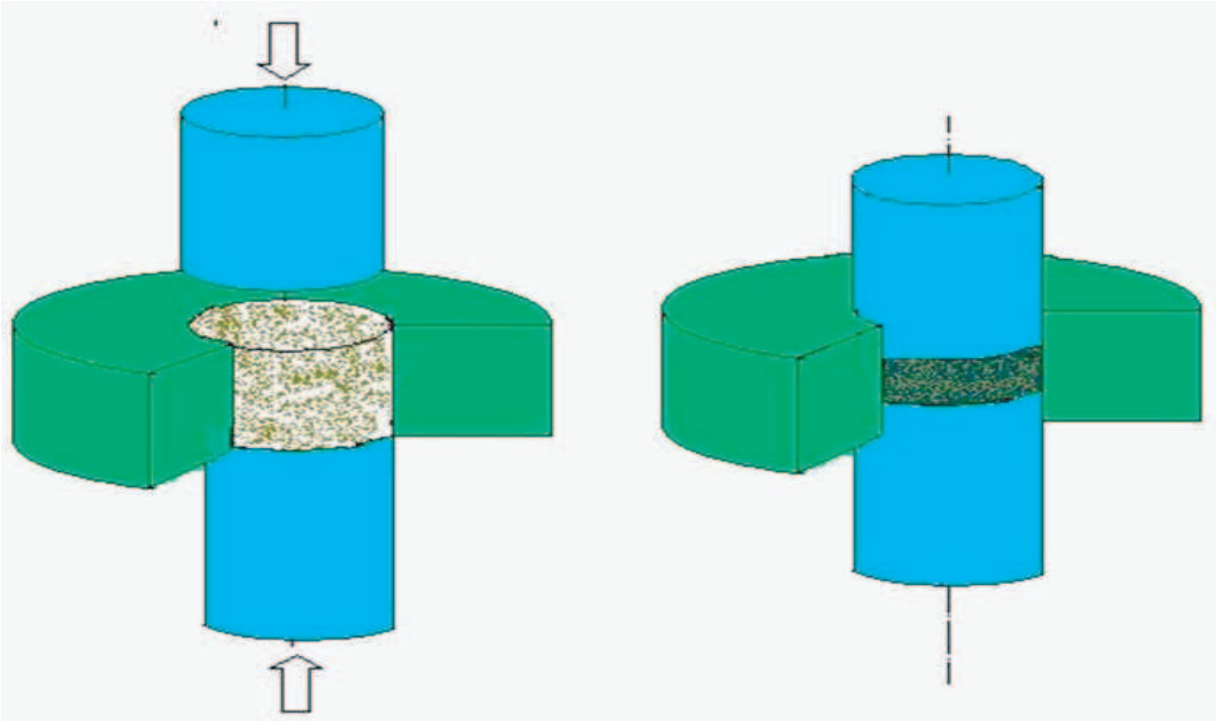

Figure 3.8. Schematic of a uniaxial die pressing experiment

$$p_b = \frac{(1 + R\tan\beta)\sigma_z}{1 + R\tan\beta\sqrt{1 + (\frac{2}{3R})^2}} \tag{3.7}$$

The volumetric strain is derived from the relative density, ρ, as:

$$\varepsilon_{vol}^{pl} = \ln(\frac{\rho}{\rho_0}) \tag{3.8}$$

where ρ_0 is the initial relative density.

Figure 3.9(a) shows the density-stress plot while Figure 3.9(b) shows the corresponding hardening law for the Drucker-Prager "cap" model.

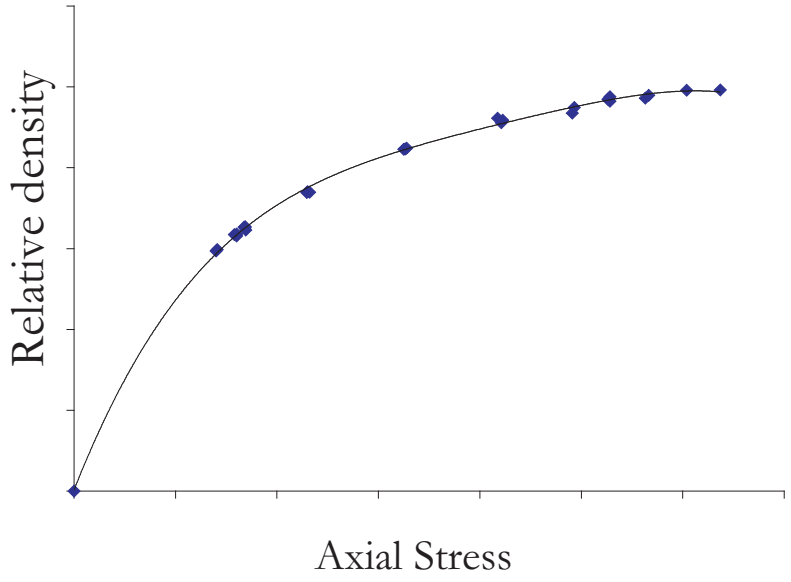

(a) Relative density - Axial stress plot

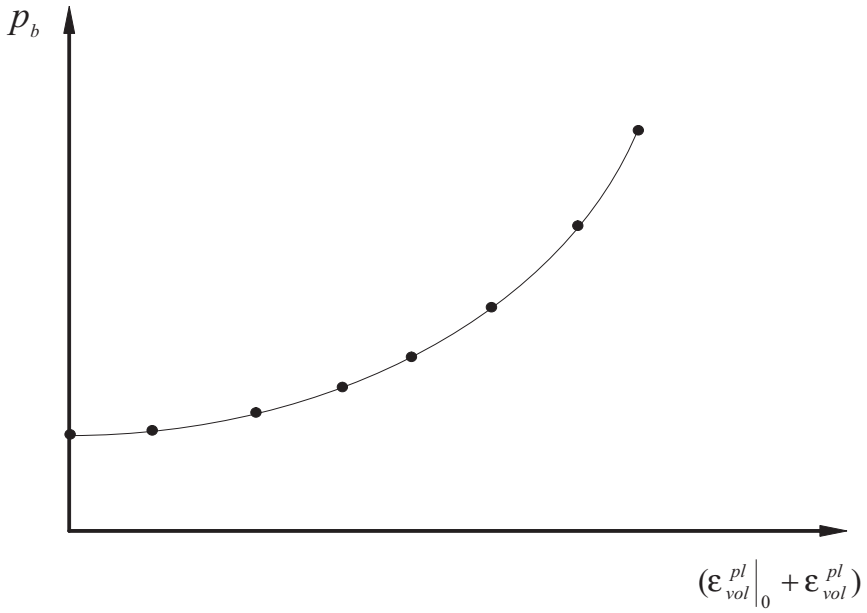

(b) Hardening law

Figure 3.9. Hardening parameter determined by uniaxial die pressing experiment for high strength materials

3.4 Statistical Sensitivity Analysis of "Cap" Model Parameters

In order to use a numerical tool in industry for simulating the powder compaction process, the material parameters need to be characterized. For metal powders, the loads for triaxial and hydrostatic tests can be very high making the triaxial test apparatus and set-up very expensive. Very few high strength triaxial test set-ups are commercially available and are not easily accessible to industry for material characterization. Hence a parameter sensitivity study was performed numerically to determine the effect of the model parameters on numerically predicted density gradients.

Some sensitivity analysis of "cap" model parameters has been reported in literature previously. He et al. (2001) studied the effect of the Cap plasticity parameters such as d, β , R and α on the density gradients achieved after compaction to show that the cap eccentricity parameter is the most significant in producing density gradients for a given set of parameters. However, the approach involved studying the effect of one factor at a time. The effect of two factors interacting on the density gradient was not considered. Chtourou et al. (1996) used a series of Taguchi planned simulations to address friction-free uniaxial strain compression tests described by the Cap model. In their work, the relative influence was determined in terms of the contributing percentage and the Fisher factor, F, of each parameter by applying the ANOVA (Analysis of Variance) method. They showed that the hardening parameters and the elastic moduli were most influential. While the design considered interaction effect of factors, the ANOVA method cannot be applied in numerical simulations since there is no error (or variance) between replications.

3.4.1 Numerical Model for Sensitivity Analysis

The model complexity makes it challenging for implementing it in industrial applications to a range of products and material systems unless the number of parameters can be reduced or their significance on the results be identified. A statistical analysis using a two-level factorial design approach was conducted to determine the effect of the model parameters and their interactions on the density predictions for a compacted part. A

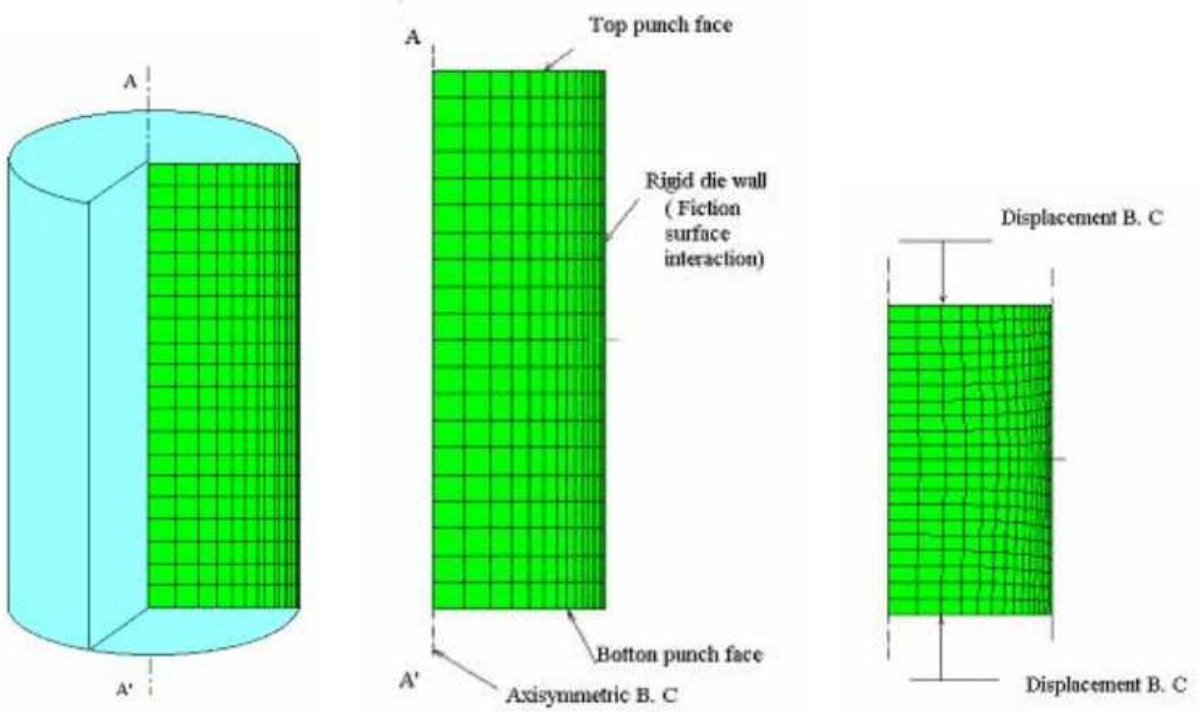

(a) Cylindrical model (b)Before compaction (c) After compaction

Figure 3.10. ABAQUS finite element mesh to simulate double-action die compaction

simple axisymmetric geometry was chosen for simulating compaction. The specimen was modeled in ABAQUS using a 300 element mesh made up of axisymmetric 8-noded bi-quadratic elements. The die wall was modeled as a rigid surface. A clearance of 0.001mm was prescribed between the compact and die-wall. The friction between the boundary elements and the die wall was modeled as a friction surface interaction with a classical isotropic Coulomb friction model. Figure 3.10 shows the mesh before and after compaction along with the boundary conditions. Only half of the cylinder was modeled to account for the symmetry about the longitudinal axis. For a double acting pressing, the displacement boundary conditions were specified on both the top and bottom model surfaces.

3.4.2 Factorial Design Approach to Sensitivity Analysis

Most of the sensitivity analysis conducted in the past considers a one factor at a time approach in which everything is held constant while only one factor is varied at a time.

In a designed experimental approach (Montgomery, 2001), factors are allowed to vary simultaneously and the respective data is gathered and analyzed. This analysis can not only detect differences between the sample means, but the effect of the interactions between two or more variables. Many experiments involve the study of the effects of two or more factors. In such cases, the following types of factorial experiments are conducted to test the effect of factors and their interactions.

- Full Factorial Design - This approach tests the effect of each factor at all levels of the other factors and determines whether or not this effect changes as the other factors change. Thus it tests not only for the effects of the factors separately, but also for interactions.

- Two-level Factorial Designs - As the number of factors increase, running the experiments at all possible levels of all factors becomes expensive. In such cases, an initial factor screening experiment is conducted to determine which factors are important. Referred to as a two-level factorial design, the approach uses k number of factors, each run at only two levels. Hence the size of the experiment is 2^k.

- Two-level Fractional Factorial Designs - If the higher order interactions are assumed to be negligible, information on the main effects and the low-order interactions can be obtained by running only a fraction of the complete factorial experiment to further reduce experimental costs. A major use of these experiments is to screen out the non-affecting factorial. Some of these experiments include half fractional (2^{k-1}), quarter fractional (2^{k-2}), etc.

The higher the fraction of the experiment, the lower is the resolution of the design, i.e., its inability to predict if the effect is due to a main effect or an interaction and if an interaction, which one. It is therefore crucial to select a fractional design such that the effect of the main effects and the lower order interactions such as the two factor interactions and the three factor interactions can be predicted clearly.

In this chapter a study of the parameters that define the Drucker-Prager "cap" model is conducted with their effect on predicting density gradients. As described in the previous chapter, there are six plasticity parameters (d, β , R, $\varepsilon_{vol}^{pl}|_0$, α, and K) and a hardening

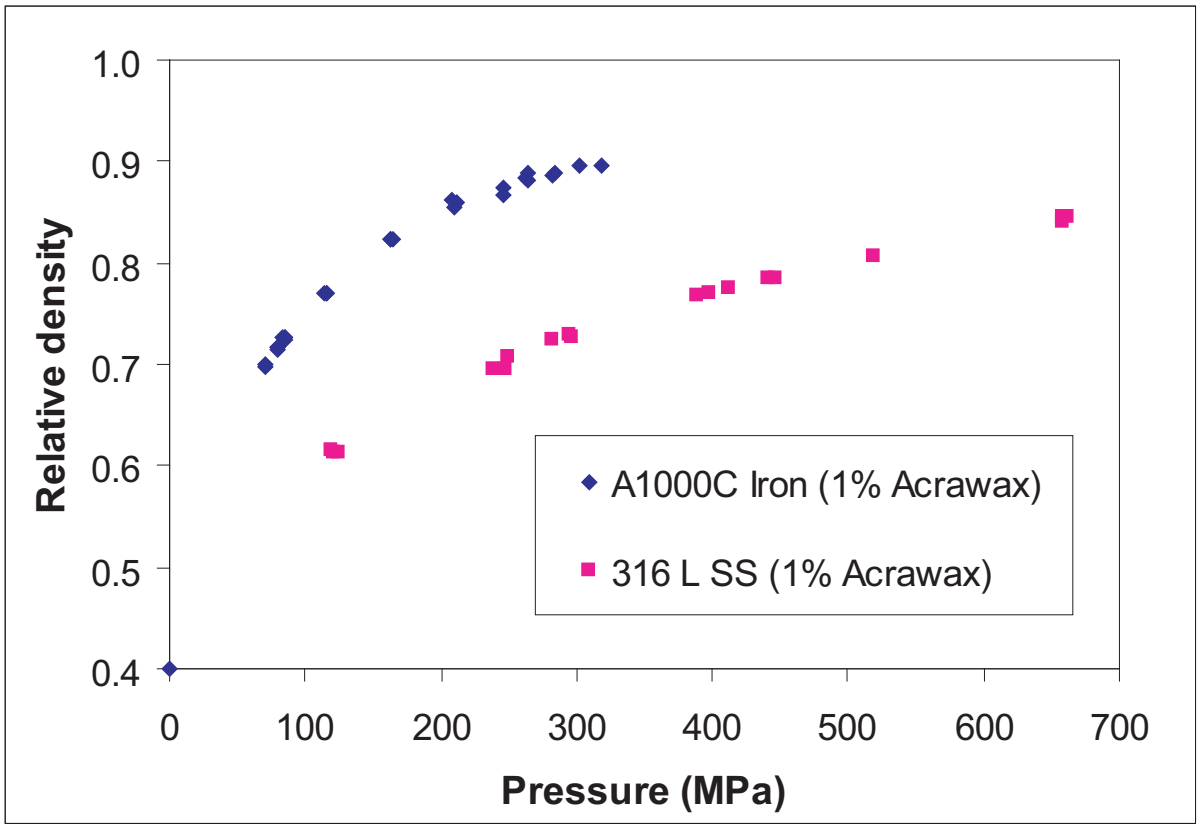

Figure 3.11. Experimental pressure-density plot for metallic grade of powders

law. The ratio of the stress in triaxial tension to the flow stress in triaxial compression, K, was assumed to be 1. Hence, our design has six factors. A two-level factorial design would require 64 runs in a 2^6 design to have all possible combinations of the factors. Since this is set as a screening experiment to find out which factors affect density gradient, we select a one-half fraction 2^{6-1} design with 32 runs. In this design all the main effects and the two-factor interactions are independent of other main effects and two-factor interactions. The three factor interactions are aliased with other three factor interactions. However they can be separated if necessary based on the Ockham's razor principle. The set-up of the numerical runs as obtained from the statistical software MiniTab is shown in Table 3.1.

The actual values of the parameters were selected to cover the range of values reported in the literature for different grades of powders. The study was divided into two grades of powders depending on their hardening behavior: Metallic grade describing the hardening

Table 3.1. Half fractional (2^{6-1}) design with 32 numerical runs(Note: -1 - Low value; 1 - High value)

Std. Order	d	β	R	p_b **vs** ε_{vol}^{pl}	α	$\varepsilon_{vol}^{pl}\vert_0$
1	-1	-1	-1	-1	-1	-1
2	1	-1	-1	-1	-1	1
3	-1	1	-1	-1	-1	1
4	1	1	-1	-1	-1	-1
5	-1	-1	1	-1	-1	1
6	1	-1	1	-1	-1	-1
7	-1	1	1	-1	-1	-1
8	1	1	1	-1	-1	1
9	-1	-1	-1	1	-1	1
10	1	-1	-1	1	-1	-1
11	-1	1	-1	1	-1	-1
12	1	1	-1	1	-1	1
13	-1	-1	1	1	-1	-1
14	1	-1	1	1	-1	1
15	-1	1	1	1	-1	1
16	1	1	1	1	-1	-1
17	-1	-1	-1	-1	1	1
18	1	-1	-1	-1	1	-1
19	-1	1	-1	-1	1	-1
20	1	1	-1	-1	1	1
21	-1	-1	1	-1	1	-1
22	1	-1	1	-1	1	1
23	-1	1	1	-1	1	1
24	1	1	1	-1	1	-1
25	-1	-1	-1	1	1	-1
26	1	-1	-1	1	1	1
27	-1	1	-1	1	1	1
28	1	1	-1	1	1	-1
29	-1	-1	1	1	1	1
30	1	-1	1	1	1	-1
31	-1	1	1	1	1	-1
32	1	1	1	1	1	1

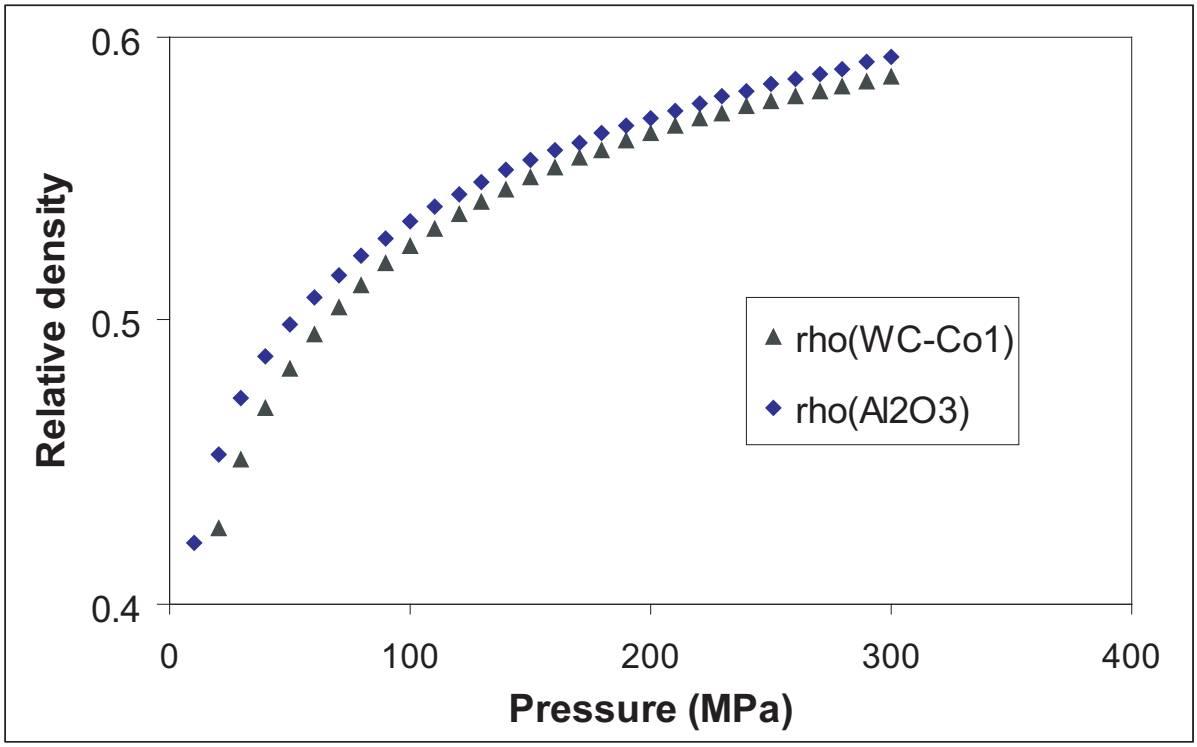

Figure 3.12. Pressure-density plot for ceramic grade of powders(Ref: Secondi (2002))

behavior for powders such as iron, steel, copper and ceramic grade of powders describing the hardening law for powders such as alumina, tungsten carbide. The pressure-density plots for the metallic grade powders and the ceramic grade powders (Secondi, 2002) are shown in Figures 3.11 and 3.12 respectively. The values are also based on certain limitations on parameters due to values of the other parameters. e.g. while the description of the transition parameter, α, says it is a small number, it has a higher limit based on the material angle of friction imposed in ABAQUS due to geometric considerations. The output metric considered for the statistical analysis was defined as:

$$OutputMetric = \frac{Max.density - Min.density}{1/2(Max.density + Min.density)} \tag{3.9}$$

3.4.3 Sensitivity Analysis Results

Table 3.2 and Table 3.3 show the low and high values of the parameters selected for the metallic grade and the ceramic grade of powders respectively.

Table 3.2. Parameter values for metallic grade of powders

Parameters	**Term**	**Low value**	**High value**
Material cohesion, d	A	0.01 MPa	1.0 MPa
Material angle of friction, β	B	60°	71.5°
Cap eccentricity, R	C	0.1	0.87
Hardening law	D	A1000C (Fe)	316 L (St. steel)
Transition surface radius parameter, α	E	0.01	0.1
Initial volumetric plastic strain, $\varepsilon_{vol}^{pl}\|_0$	F	0.01	0.1

Table 3.3. Parameter values for ceramic grade of powders

Parameters	**Term**	**Low value**	**High value**
Material cohesion, d	A	0.01 MPa	0.015 MPa
Material angle of friction, β	B	60°	71.5°
Cap eccentricity, R	C	0.1	0.87
Hardening law	D	Al_2O_3 (Alumina)	WC-Co
Transition surface radius parameter, α	E	0.01	0.1
Initial volumetric plastic strain, $\varepsilon_{vol}^{pl}\|_0$	F	0.01	0.1

Figures 3.13 show the normal probability plots for the two grades of powders. Individual letters represent the effect of an individual parameter while a string of letters represents the effect of interaction between the parameters indicated by the letters (e.g., BC implies an effect of interaction of the material angle of friction, β, and the cap eccentricity parameter, R). Based on the deviation from the normal effects line and the values of estimated effects, it was seen that the density gradient is sensitive to the following parameters in the following rank:

1. Cap eccentricity, R,
2. Material angle of internal friction, β, and
3. Combination of R and β

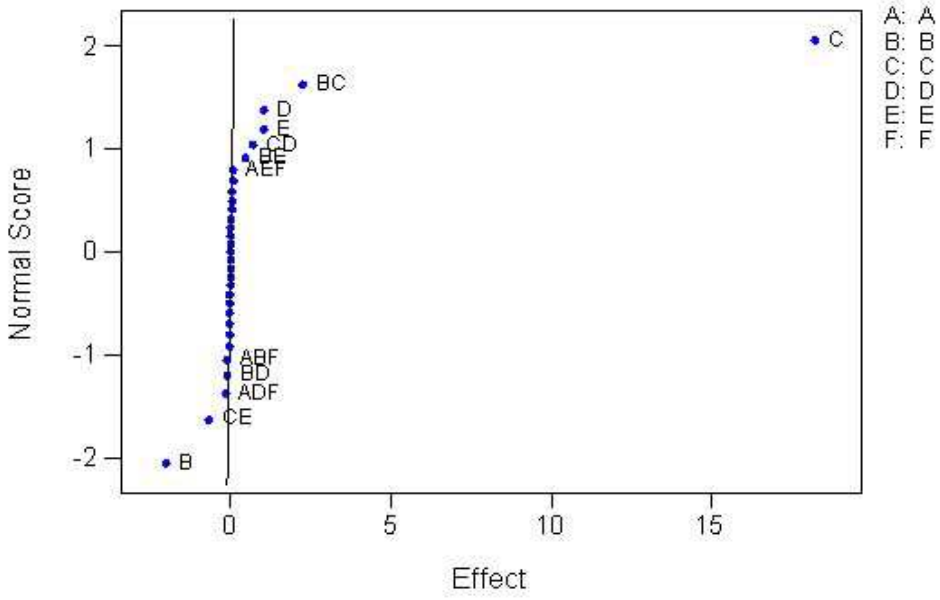

(a) Metallic grade powders

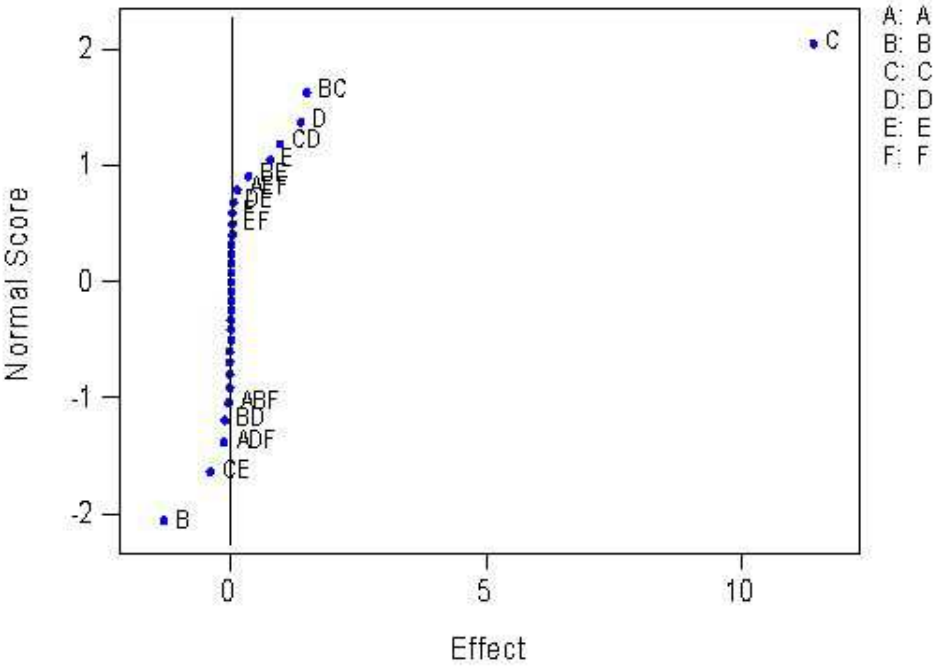

(b)Ceramic grade powders

Figure 3.13. Normal probability plots

This implies that the cap eccentricity parameter and the material angle of friction are the most influential parameters that affect the density gradient in a compacted part. Hence to accurately predict the density gradient using numerical simulations, it is essential that these parameters be accurately determined for a given powder. This is consistent with the findings from He et al. (2001) who indicate the importance of the eccentricity parameter on density difference. However due to a one factor-at-a-time approach, that work was unable to predict the effect of the material angle of friction and its interaction effect with the eccentricity parameter on the density gradient.

In summary, the complex Drucker-Prager "cap" model which is able to model the compaction process from the particle rearrangement stage through the particle deformation stage contains seven parameters. The sensitivity of density predictions depends on the accuracy of two parameters. Specifically, the cap eccentricity parameter, R, and the material angle of friction, β, must be accurately determined as variation in those parameters produce significant variation in the density field prediction. Earlier in this chapter the triaxial test method was described to provide a physical description of the parameters. While that technique is most robust, it is also expensive and not easily accessible due to the limited number of high load triaxial test apparatus available. Thus alternative simpler testing methods are required to determine the "cap" model parameters used in numerical simulations. An alternative experimental method to determine the failure surface parameters using a combination of uniaxial compression test and Brazilian disk test has been proposed by Coube and Riedel (2000) and is discussed in the following chapter. An alternative method for determining the cap eccentricity parameter for metal powders is proposed as part of this research and is presented in Chapter 5.

Chapter 4

Failure Surface Parameters for High Strength Materials

4.1 Introduction

For high strength materials such as metallic powders, it is difficult and expensive to build a triaxial compression apparatus due to the excessively high consolidation pressures. Coube and Riedel (2000) have proposed an alternative testing methodology in a combination of uniaxial compression test and a Brazilian disk test (splitting tensile test) to determine the failure surface parameters at lower loads due to the absence of high confining pressures in the radial direction. In this chapter, the method is described and the results of the uniaxial compression tests and Brazilian disk test are presented for three powder-lubricant systems and the failure surface parameters determined for different densities of compaction.

4.2 Failure Surface Characterization Tests

The uniaxial compression and Brazilian disk represent two load scenarios which exhibit shear failure; therefore the results from these tests can be used to establish a failure surface. Figure 4.1 shows the schematic of uniaxial compression and Brazilian disk test.

The uniaxial compression test (schematic Figure 4.1(a)) is not governed by any standard.

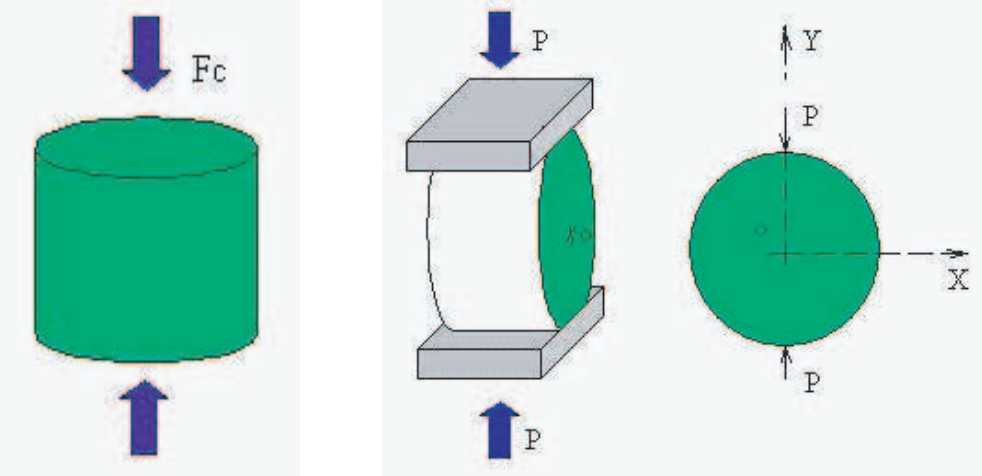

(a) Uniaxial compression test (b) Brazilian disk test

Figure 4.1. Schematic of compression and splitting tensile tests

However according to Kuhn (2000), the specimen is cylindrical in shape with a recommended height-to-diameter ratio of less than 2. Coube and Riedel (2000) use a height-to-diameter ratio of 1 for their cylindrical specimen. Specimens are loaded axially without any radial constraint until the specimens fail in shear. The stress at failure, σ_c, mean stress, p, and the deviatoric stress, q are calculated as:

$$\sigma_c = \frac{F_c}{A} \tag{4.1}$$

$$p = \frac{\sigma_c}{3} \tag{4.2}$$

$$q = \sigma_c \tag{4.3}$$

where F_c is the axial load at failure, and A is the area of cross-section.

The Brazilian disk test (schematic Figure 4.1(b)) is performed as per ASTM Standard D3967-95a (2001). The specimen is circular in cross-section with a height-to-diameter ratio between 0.2 and 0.75. The apparatus consists of a loading device to apply and measure axial load on the specimen. Bearing surfaces in contact with the specimen can be flat or curved. Assuming plane stress, failure occurs due to maximum tensile failure stress at the

center of the disk. According to a theoretical study by Timoshenko and Goodier (1969), the state of stress at the center of the disk in terms of the tensile failure stress, σ_t, and the corresponding compressive stress, σ_c, is given by:

$$\sigma_t = \frac{2P}{\pi DT} \tag{4.4}$$

$$\sigma_c = \frac{-6P}{\pi DT} \tag{4.5}$$

where P is the load at failure, D is the diameter of the specimen, and T is the height of the specimen.

The mean stress, p, and the deviatoric stress, q, can then be calculated as:

$$p = \frac{2\sigma_t}{3} \tag{4.6}$$

$$q = \sqrt{13}\sigma_t \tag{4.7}$$

The $p - q$ points from the two tests are then plotted in the meridional plane for different densities as shown in Figure 4.2. The Drucker-Prager shear failure surface is then determined as the best fit line passing through these two points.

4.3 Powder-Lubricant Systems

Three powder-lubricant systems were studied for the determination of the failure surface parameters. The powders were selected to constitute commonly used materials used for die compaction applications. The corresponding lubricant was admixed with the powder to reduce die wall friction and facilitate ejection.

A water atomized iron powder was selected as it is the most commonly used material for die compaction. The powder selected is Hoeganaes A1000C (Fe + 0.8%C). The particles are irregular in shape and of different sizes and thus suitable for die compaction. Fig-

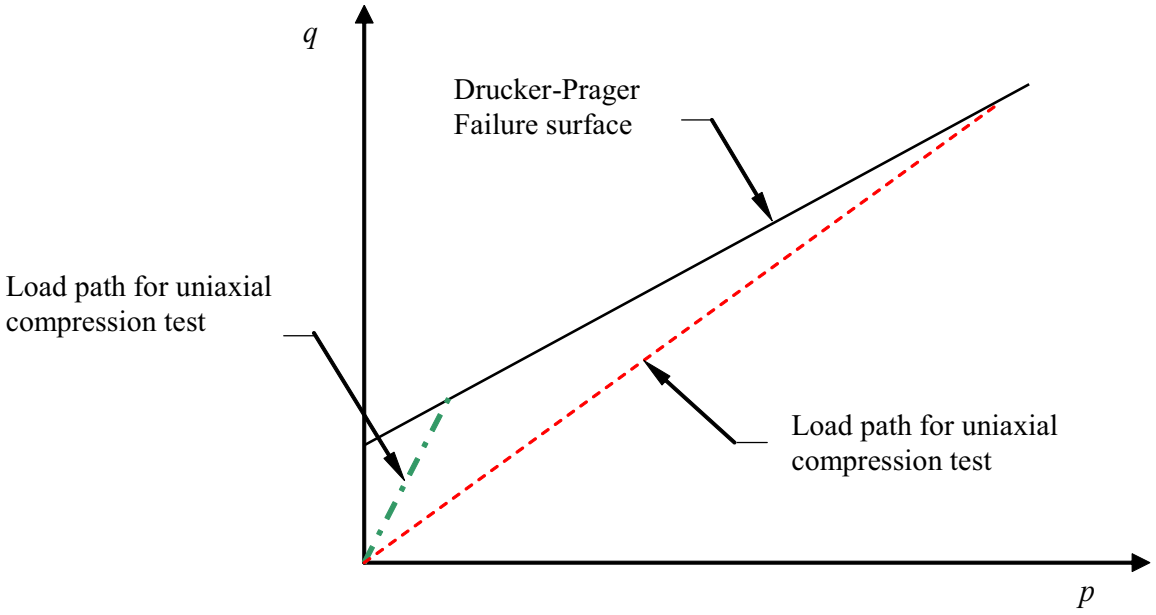

Figure 4.2. Load paths for uniaxial compression test and Brazilian disk test

ure 4.3 shows the SEM image of the irregular shaped powder particles. The particle size distribution D_{10}, D_{50} and D_{90} for the powder is 59μm, 136μm and 226μm, respectively. Lubrication was provided by blending 1% Acrawax C lubricant by weight to the powder. The apparent density and pycnometer density are 2.8 g/cm^3 and 7.86 g/cm^3, respectively.

In order to compare the effect of strength of material on the failure surface parameters, a water atomized stainless steel powder was selected. The material is 316L stainless steel and the powder was provided by *Höganäs*. It is a chemical composite of 0.01% carbon, 0.01% sulfur, 2.3% molybdenum, 12.7% nickel, 66.66% iron, 0.1% manganese, 17.1% chromium, 0.8% silicon, 0.242% oxygen and 0.079% nitrogen. It is suitable for corrosion resistant applications. Figure 4.4 shows the SEM image of the powder particles. The particles are irregular in shape similar to the iron powder. The particle size distribution D_{10}, D_{50} and D_{90} for the powder is 22μm, 48μm and 93μm, respectively. Thus it can be seen that the particle size distribution is smaller compared to the iron powder. The apparent density and pycnometer density are 3.1 g/cm^3 and 7.87 g/cm^3, respectively. Lubrication was again provided by blending 1% Acrawax C lubricant by weight to the powder.

Finally to compare the effect of lubricant, ethylene vinyl acetate (EVA) a copolymer of poly-

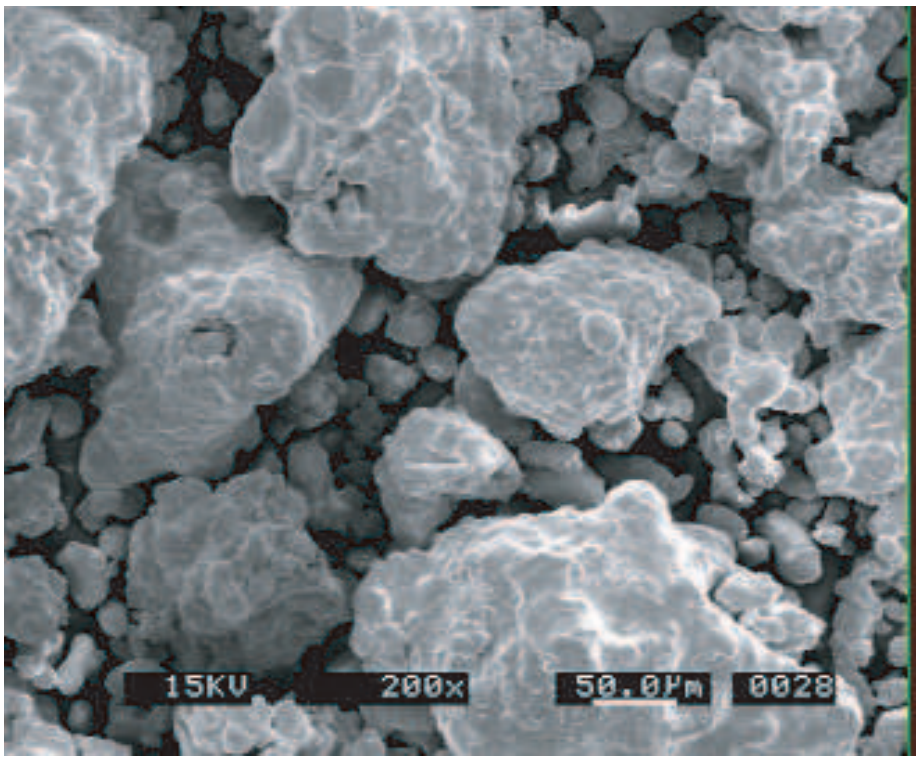

Figure 4.3. SEM image of Hoeganaes A1000C iron powder

ethylene was admixed with the powder as per the procedure prescribed by Enneti (2005). The procedure was prescribed to facilitate compaction of gas atomized 316L stainless steel powder. However in this study, the procedure was used with water atomized 316L stainless steel powder. A polymer emulsion corresponding to the final required amount of 1% EVA polymer was placed in a glass beaker. The emulsion was diluted by adding distilled water of five times its weight. The solution was stirred and the powder was then added to the diluted emulsion. The diluted emulsion along with the metal powder was stirred to obtain a slurry of metal particles and diluted polymer. The slurry was then dried at 100°C in an oven for 3 hrs to remove the water. The dried mix was fed into a granulator (model: ZM 100, supplier: Glen Mills Inc., Clifton, NJ) to obtain the admixed powder-polymer system. The admixed powder was then sieved for 30 minutes to break the soft agglomerates and the -100 mesh powders was used for compaction. A flow diagram of the mixing process is shown in Figure 4.5.

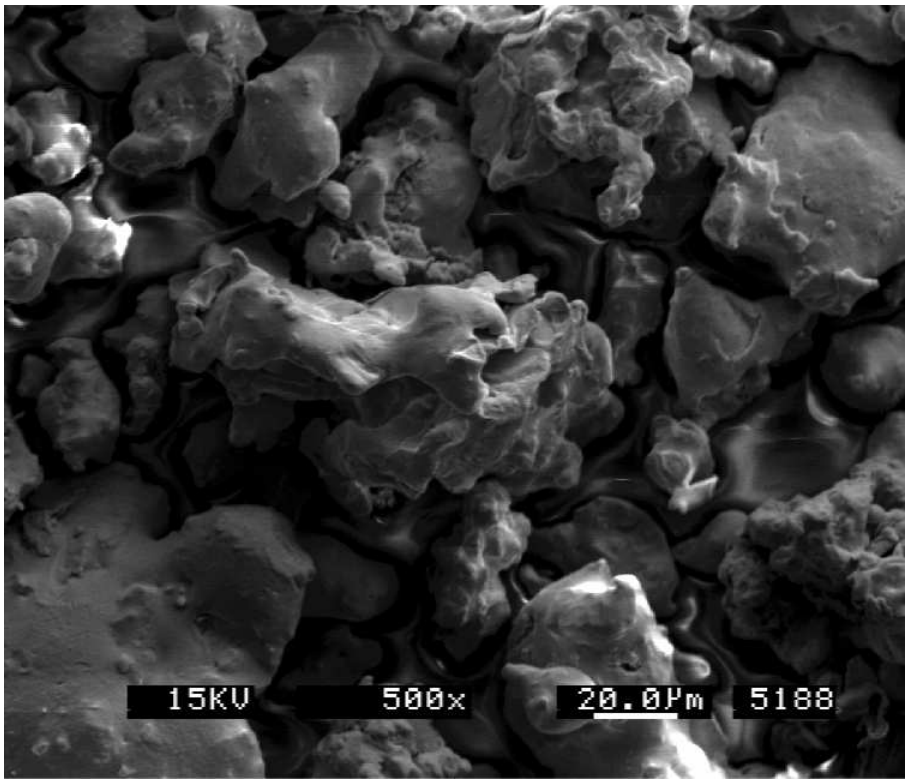

Figure 4.4. SEM image of *Höganäs* 316L stainless steel powder

4.4 Sample Preparation

For the uniaxial compression test, the samples were compacted manually in a cylindrical die. The diameter of the samples was 12.7 mm (0.5 in) while the heights of the samples ranged from approximately 12 mm to 14 mm in order to achieve various density compacts and still satisfy the required height-to-diameter ratio of approximately 1. The samples were compacted to relative densities varying from 70% to 78%. This range of densities was selected due to tool constraints for further tests.

For the Brazilian disk tests, the compaction was carried out on a 60 ton hydraulic press (Gasbarre Products, PA). The diameter of the samples was 31.75 mm (1.25 in) while the heights varied from 18 mm to 20 mm for a height-to-diameter ratio of approximately 0.6 which was in the range of 0.2 - 0.75 as required per ASTM Standard D3967-95a (2001).

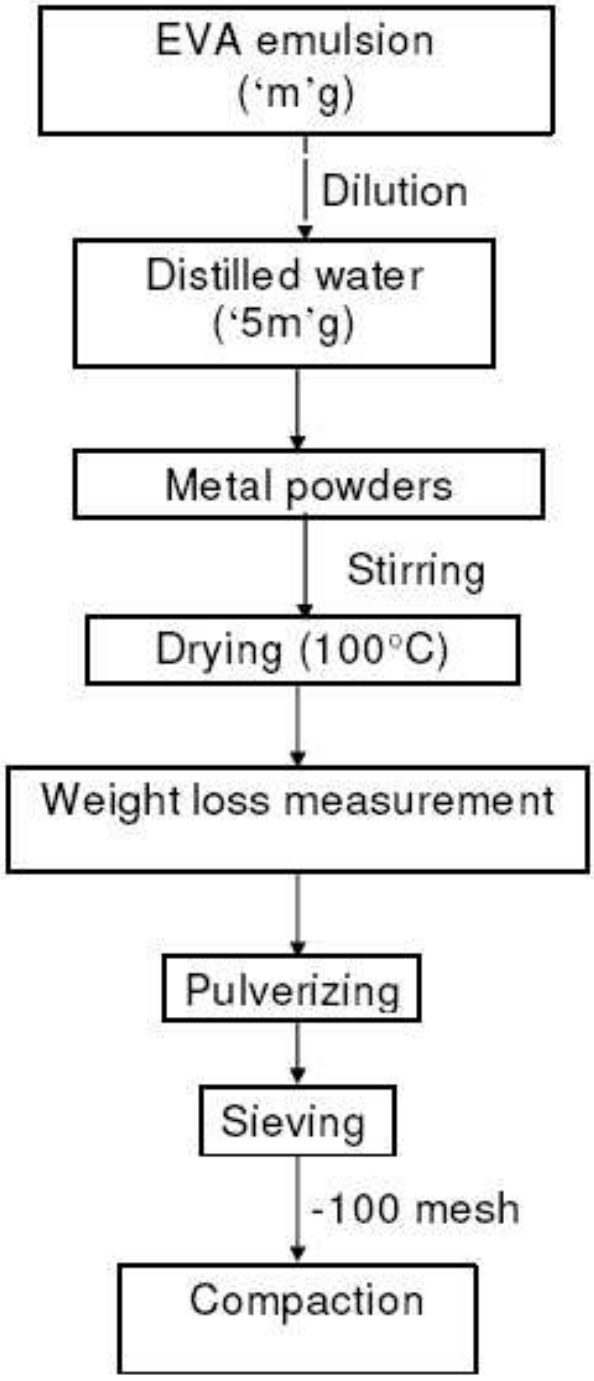

Figure 4.5. Flow diagram for mixing 316L stainless steel powder with EVA

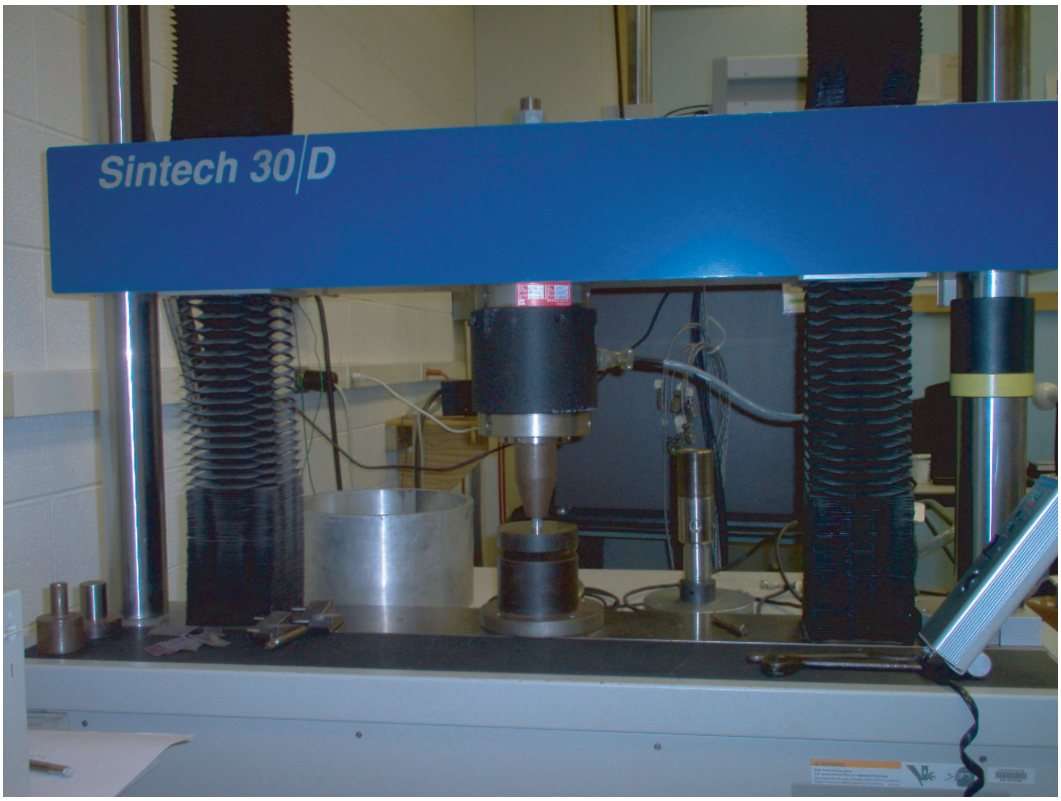

Figure 4.6. Uniaxial compression test set-up on a Sintech machine

The uniaxial compression test and Brazilian disk test were carried out on a Sintech 30D Hydraulic press. Figure 4.6 shows the set-up of the machine for a uniaxial compression test. A 30 kPa load cell was used for data acquisition and the load-deflection curves were obtained for the samples until failure. For the uniaxial compression tests, a universal block was used as the bottom support to ensure the application of axial load while for the Brazilian disk tests, the lower platen was used to support the sample. Care was taken to ensure central loading during the Brazilian tests and a steel sleeve was used around the sample for safety in case of off-center loading which could cause the sample to be shot off as a projectile. While previous studies (He et al., 2001) have used marking strips to determine the area upon which the load is applied during the Brazilian disk test, in this study a concentrated load is assumed for ease of calculation.

4.5 Results

Figure 4.7 shows the failure compressive stress versus relative density of the compacts during the uniaxial compression tests for the three powder-lubricant systems. It can be seen that the failure stresses are least for the iron powder while they are higher for the stainless steel powder systems. This is expected due to the difference in the strength of the materials. Figure 4.8 shows the failure surface of the compacts under uniaxial tests indicating that the the samples have failed in shear.

The plot of the failure tensile stress versus the relative density of the compact during the Brazilian tests is shown in Figure 4.9 for the three powder-lubricant systems. Again it can be seen that the tensile stresses required to shear a stainless steel compact are higher than those for iron powder. In addition it is also seen that higher stresses are required to break the sample with the EVA polymer compared to the Acrawax C admixed powder samples implying that the EVA polymer in addition to acting as lubricant also provides an inherent strength to the green compact.

4.6 Failure Surface Parameters

The failure surface parameters, cohesion (d) and material angle of friction (β) are calculated from equations 4.1 - 4.7 and have been tabulated for the three powder-lubricant systems in Tables 4.1 - 4.3.

The variation of the failure surface parameters for the three powder-lubricant systems with relative density of compact can be seen in Figure 4.10. It is seen that the material angle of friction does not vary much with density and it is slightly lower at higher density as expected since the material should behave like a von Mises material at 100% density. The material cohesion increases with relative density since the particle contact surface area increases. Again it is seen that the cohesion for stainless steel powder is higher than that for the iron powder. However, for the numerical simulation purposes where initial material cohesion at tap density is input, the value will be small and similar for either material. The material angle of friction does not vary much with relative density of compact. And

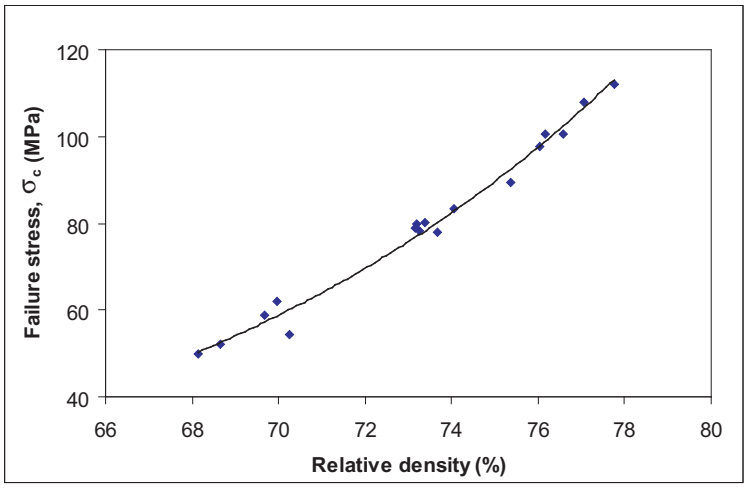

(a) A1000C iron powder + 1% Acrawax C

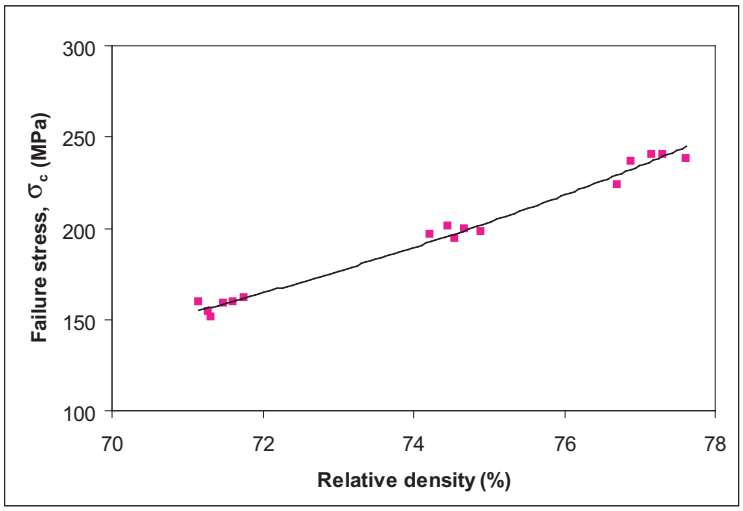

(b) 316L stainless steel powder + 1% Acrawax C

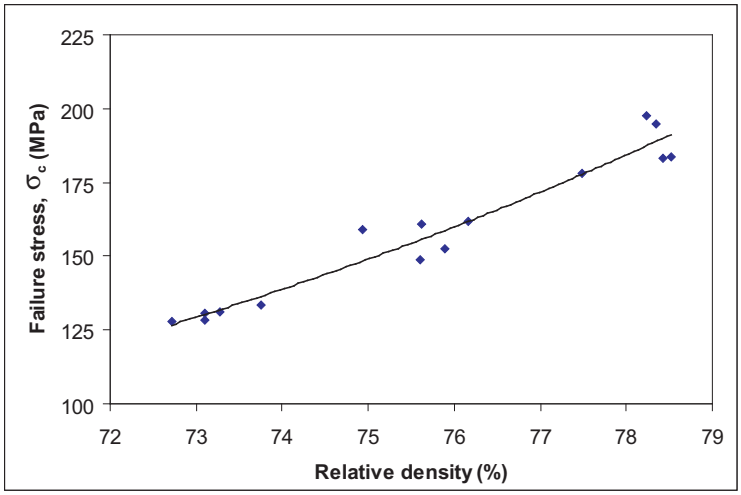

(c) 316L stainless steel powder + 1% EVA

Figure 4.7. Uniaxial compression test: Failure compressive stress vs relative density

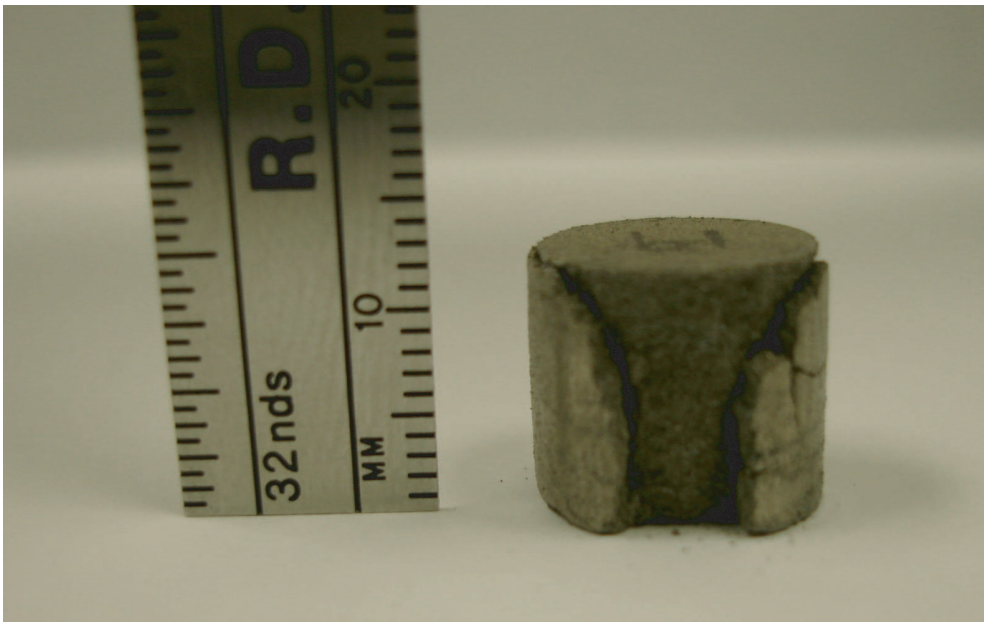

Figure 4.8. Shear failure of specimen under uniaxial compression test

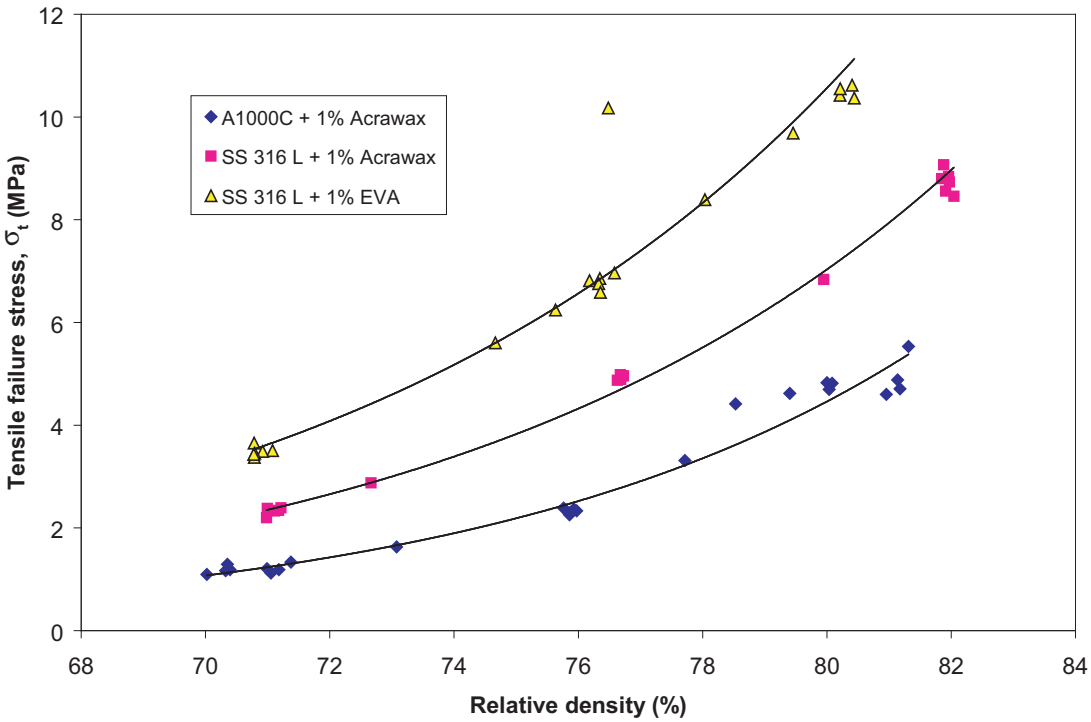

Figure 4.9. Brazilian disk test: Failure tensile stress vs relative density

Table 4.1. Cohesion and Material Angle of Friction for A1000C iron powder + 1% Acrawax C

ρ	**Uniaxial Compression**			**Brazilian Test**			**d**	β
	F_c **(N)**	**p (MPa)**	**q (MPa)**	**P (N)**	**p (MPa)**	**q (MPa)**	**(MPa)**	
70	7440	20	59	1002	0.72	3.88	1.79	71.03
72	8807	23	70	1327	0.95	5.15	2.39	70.95
74	10424	27	82	1757	1.27	6.85	3.20	70.87
76	12338	32	97	2326	1.69	9.11	4.28	70.78
78	14604	38	115	3081	2.24	12.12	5.73	70.67
80	17286	45	136	4080	2.98	16.12	7.68	70.55

Table 4.2. Cohesion and Material Angle of Friction for 316L stainless steel powder + 1% Acrawax C

ρ	**Uniaxial Compression**			**Brazilian Test**			**d**	β
	F_c **(N)**	**p (MPa)**	**q (MPa)**	**P (N)**	**p (MPa)**	**q (MPa)**	**(MPa)**	
70	18135	48	143	2245	1.34	7.22	3.31	71.15
72	20889	55	165	2871	1.70	9.21	4.23	71.11
74	24062	63	190	3672	2.17	11.75	5.42	71.06
76	27716	73	219	4697	2.77	14.99	6.94	71.01
78	31926	84	252	6007	3.54	19.13	8.89	70.93
80	36775	97	290	7683	4.51	24.40	11.39	70.85

Table 4.3. Cohesion and Material Angle of Friction for 316L stainless steel powder + 1% EVA

ρ	**Uniaxial Compression**			**Brazilian Test**			**d**	β
	F_c **(N)**	**p (MPa)**	**q (MPa)**	**P (N)**	**p (MPa)**	**q (MPa)**	**(MPa)**	
70	13273	35	105	3598	2.20	11.88	5.64	70.59
72	15295	40	121	4584	2.79	15.07	7.20	70.48
74	17625	46	139	5839	3.53	19.11	9.21	70.36
76	20310	53	160	7438	4.48	24.24	11.78	70.21
78	23404	62	185	9474	5.69	30.75	15.09	70.05
80	26970	71	213	12068	7.21	39.00	19.33	69.87

even though it was one of the identified parameters from the sensitivity analysis presented in chapter 3, the value does not vary significantly for the material system. In summary, the values of material cohesion, d, and material angle of friction, β, that will be used in the simulation are 0.1 MPa and 71.5°.

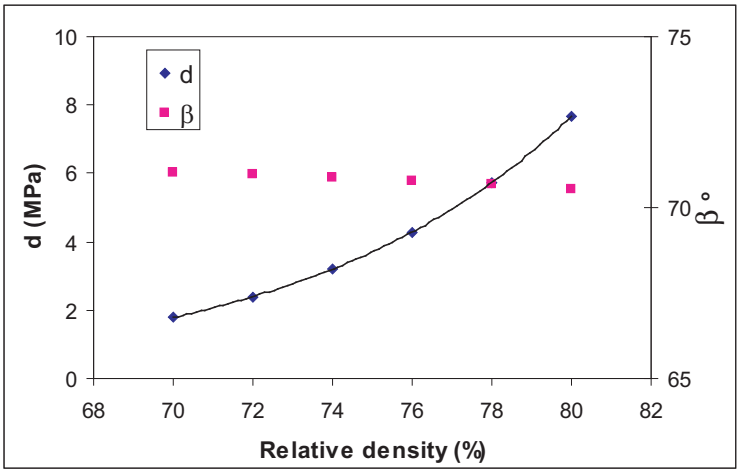

(a) A1000C iron powder + 1% Acrawax C

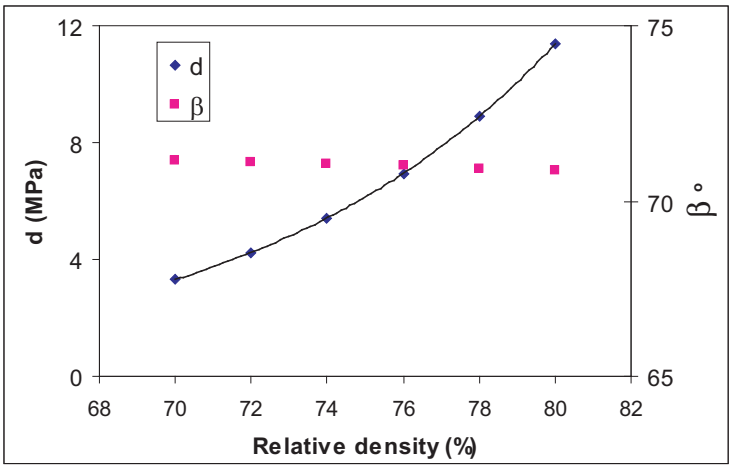

(b) 316L stainless steel powder + 1% Acrawax C

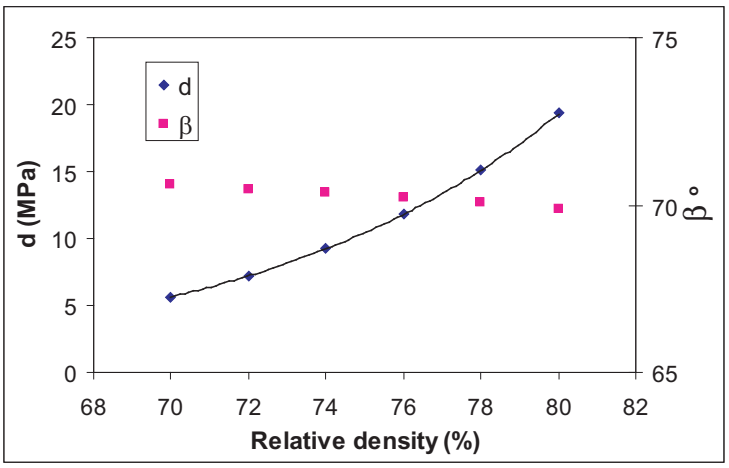

(c) 316L stainless steel powder + 1% EVA

Figure 4.10. Variation of failure surface parameters with relative density of compact

Chapter 5

Determination of The Cap Eccentricity Parameter

5.1 Introduction

As seen from the sensitivity analysis in chapter 3, the numerically predicted density gradient in a compacted part is most affected by the cap eccentricity parameter that defines the shape of the yield surface (cap). The cap eccentricity parameter is the aspect ratio of the elliptical yield cap (see Figure 3.1). The true triaxial testing method is the most robust technique for characterizing this parameter for a particulate material system. The unavailability of high load triaxial testing facilities and the high cost for set-up of these apparatus for high strength particulate materials such as metal powders makes it difficult to characterize the cap eccentricity parameter for metal powders. This is a particularly demanding challenge for industrial applications where additives, powders, and particle size distributions vary from product to product. In this chapter, a simpler alternative testing method involving a combination of numerical and simple physical experiments is proposed to determine the cap eccentricity parameter for two metal powders undergoing die compaction.

5.2 Experimental set-up

The proposed technique is based on the premise that the yield cap surface is calibrated using the triaxial test in which the material is loaded on different load paths in the $p-q$ plane to get the iso-density curves and die compaction provides a loading path which can be used to approximate the surface of the iso-density curve. Furthermore, Zipse (1997) proposed that the cap eccentricity parameter can be inferred from measured ratios of the radial to the axial pressures (σ_r/σ_z) in the compact during die compaction. Further support of this approach is the work of Doremus et al. (2001). They have used a closed die compaction experiment with an instrumented die to measure the radial stresses and determine the cap eccentricity parameter. While the axial pressure during compaction can be measured from the applied compaction load, measurement of the radial stress is difficult unless the tool is equipped with radial load cells. An experimental set-up involving an instrumented die is costly.

A testing approach which builds from the earlier work of Zipse (1997) and Doremus et al. (2001) but addresses the challenge presented by internally instrumented dies is proposed. To reduce the cost of experimental set-up, a simple tool mounted with resistance strain gages on the outer die wall to measure the hoop strains on the die surface during compaction is investigated in this research. A cylindrical die made of tool steel with an inner diameter of 20.3 mm (0.8 in) and outer diameter of 63.5 mm (2.5 in) was used in this experiment. The die was designed to have enough rigidity to apply the compaction pressures while at the same time being flexible enough to produce measurable strains on the outer die wall. Figure 5.1(a) and (b) show the die dimensions and the schematic set-up of die compaction for hoop strain measurement respectively.

Two powder-lubrication systems were used for compaction during the strain measurement experiment. They were the water atomized A1000C iron powder (Hoeganaes) with 1% Acrawax C lubricant and the water atomized 316L stainless steel powder (*Höganäs*) with 1% Acrawax C lubricant. These systems were selected since both these powders are commonly used in die compaction applications and it is expected that the strength of material affects the yield surface. The samples were compacted on a manual press (Carver Inc.).

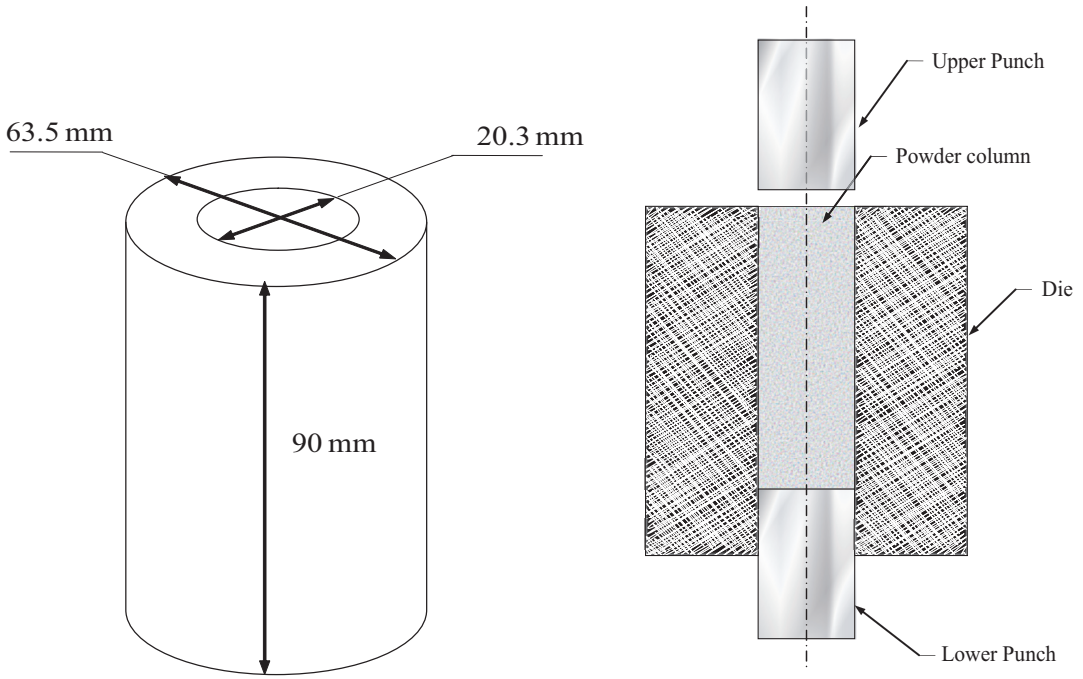

(a) Die dimensions (b) Schematic set-up for compaction

Figure 5.1. Experimental set-up for die compaction

The samples were single compacted to different relative densities ranging from 65% - 75% of the bulk density. Higher densities were not possible since the die was not rigid enough to prevent buckling of the punch.

In order to determine the location to mount the strain gages on the die wall, a preliminary numerical simulation of the experimental process was carried out in ABAQUS. Figure 5.2(a) and (b) show the mesh used to numerically determine the hoop strain at the outer die wall before and after compaction. The single compaction was numerically simulated by prescribing a moving boundary condition on the top node set of the powder while the bottom node sets of the powder and the die are constrained in the axial direction. The axisymmetric geometry was described by using axisymmetric elements and radially constraining the axial nodes of the powder. Figure 5.3 shows the hoop stress contour in the die at the end of compaction. The location for maximum hoop stress and strain was noted approximately 35mm from the bottom of the die.

Based on this preliminary numerical study five CEA-series resistance strain gages (Mea-

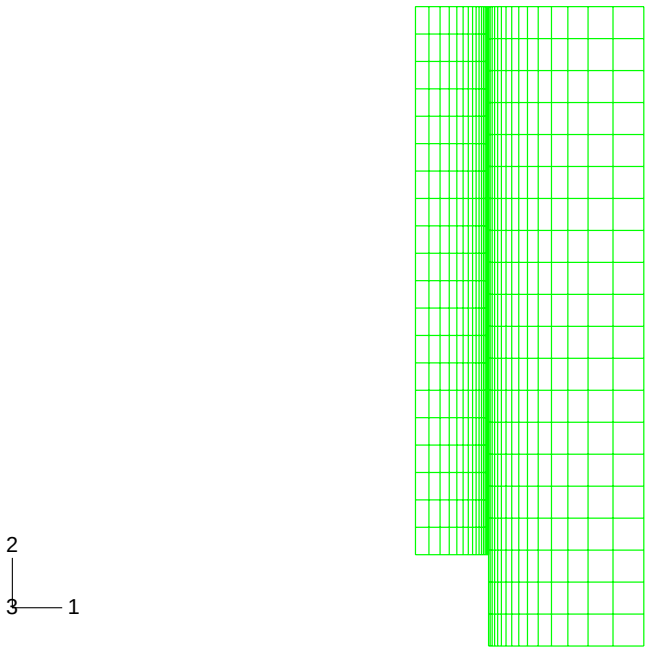

(a) FE mesh before compaction

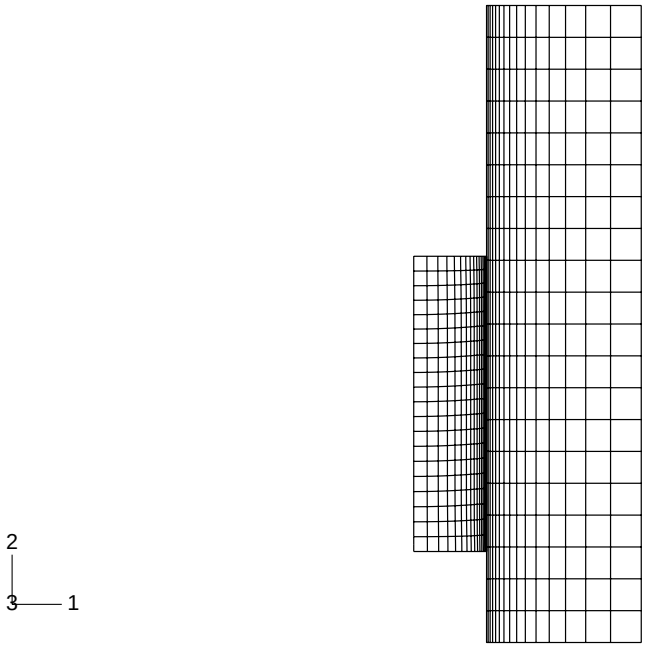

(b) FE mesh after compaction

Figure 5.2. Numerical set-up for measuring hoop strain due to compaction

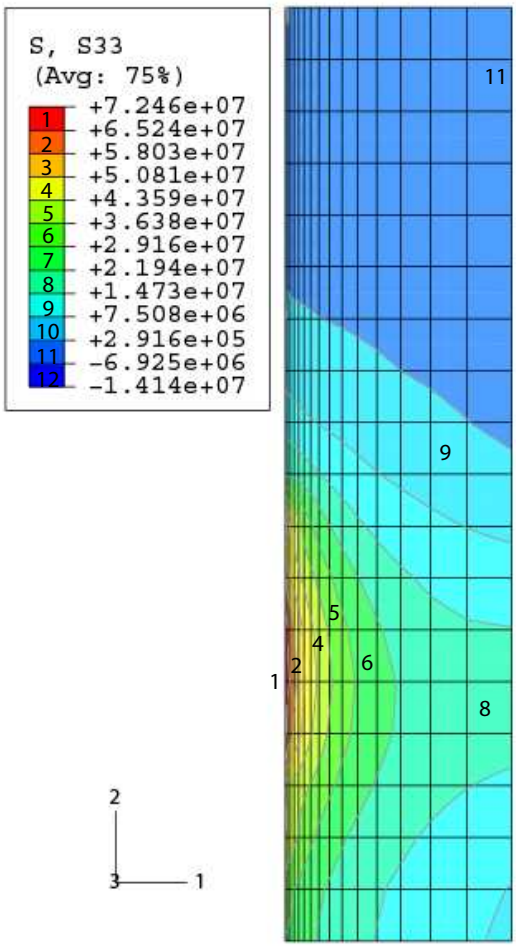

Figure 5.3. Hoop stress contour in die at the end of compaction

surements Group Inc., Raleigh NC) were mounted on the outer die wall. Figure 5.4 shows the schematic set-up of the experimental die with the locations of the five strain gages. Three strain gages were mounted at equal angles (120°) on the plane (35mm from the bottom of the die) where the maximum hoop strain was numerically generated. In addition, two more strain gages were equidistantly mounted above and below this plane to measure the strain profile along the height.

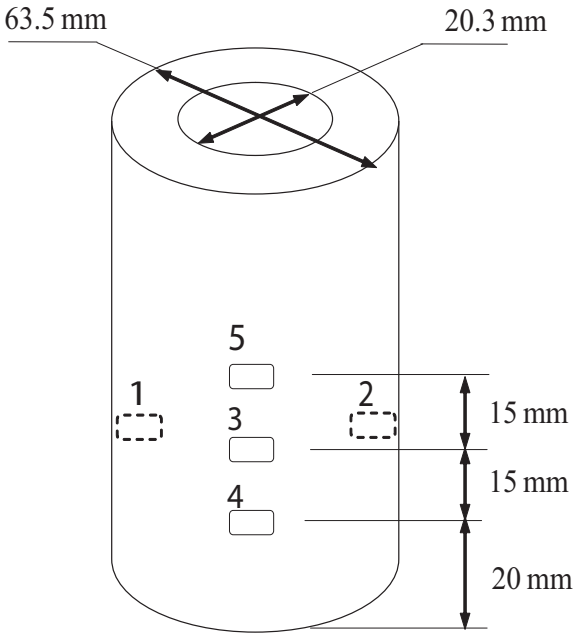

Figure 5.4. Experimental set-up to measure hoop strains at the outer die-wall

5.3 Experimental Results

The hoop strains were recorded using a P-3500 strain indicator and a SB-10 switch and Balance unit (Measurements Group Inc., Raleigh NC) in a quarter Wheatstone's bridge configuration. In order to calibrate the strain gages and the experimental set-up for axial loading, a verification experiment was performed by first loading the die wall axially on the manual press. The cylindrical die was loaded axially and the strains were measured at the gage locations. The theoretical strain on the die wall was calculated by solving the elasticity problem for a thick-walled cylinder (Boresi and Sidebottom, 1984). Since the compaction takes place at room temperature, the temperature change is assumed to be zero. Under such conditions, the deformations of the cylinder are axisymmetric. Assuming axially symmetrical loading on the die wall, the deformations at a cross-section are independent of the axial co-ordinate and a function of the radial co-ordinate only. The hoop strain at the outer die wall is given by

$$\epsilon_{\theta\theta}|_{r=r_o} = \frac{1}{E}[\frac{2p_i{r_i}^2}{{r_o}^2 - {r_i}^2} - \frac{\nu F_{axial}}{\pi({r_o}^2 - {r_i}^2)}] \tag{5.1}$$

where E is the modulus of elasticity,

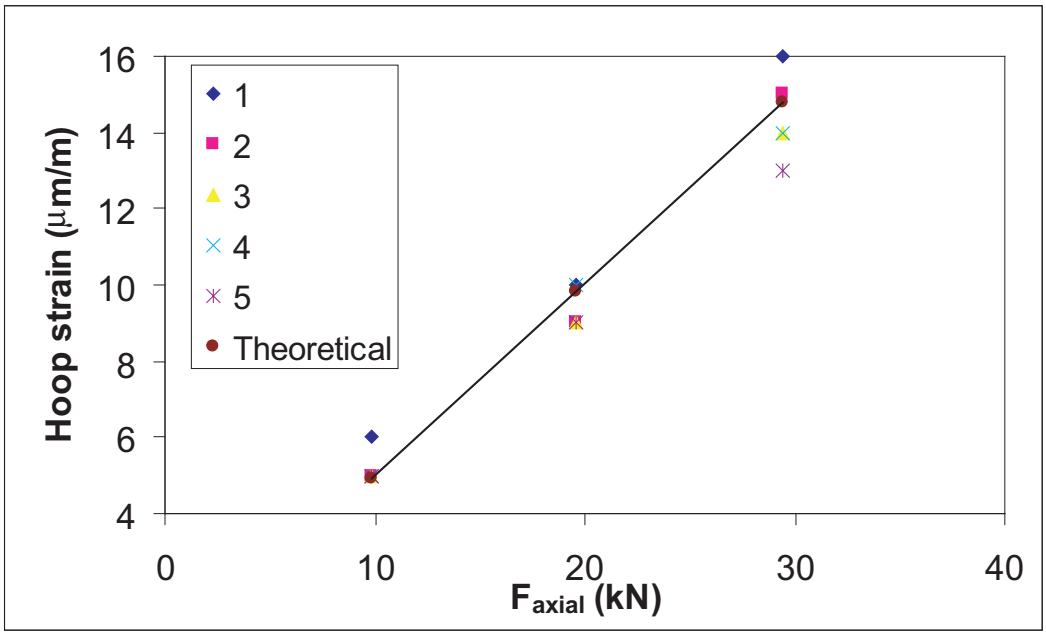

Figure 5.5. Comparison of experimental and theoretical hoop strains for calibration experiment

p_i is the internal radial pressure,
r_i is the inner radius of thick-walled cylinder,
r_o is the outer radius of thick-walled cylinder,
F_{axial} is the axial force on the cylinder.

Since there is no internal pressure acting on the cylinder during the verification experiment, Equation 5.1 reduces to

$$\epsilon_{\theta\theta}|_{r=r_o} = \frac{1}{E}[\frac{-\nu F_{axial}}{\pi({r_o}^2 - {r_i}^2)}] \tag{5.2}$$

where the negative sign implies compression. Figure 5.5 shows the comparison of the theoretical to the experimental hoop strains suggesting a good verification of the experimental set-up. This verification experiment was followed by a series of compaction set-up experiments whereby centering of the tool set-up was achieved to allow for application of axial loads only during compaction. Levels were used to ensure that the upper and lower platens of the manual press were level during compaction allowing for axial loads on the top and bottom punches.

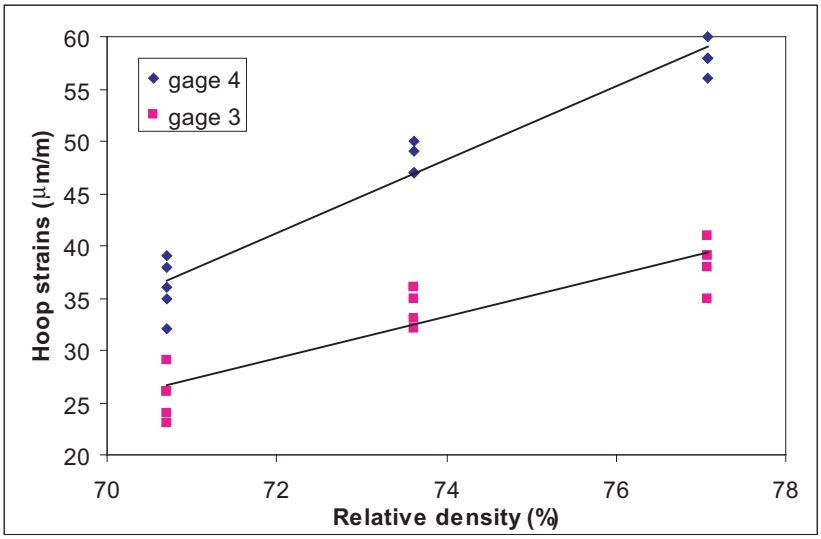

(a) A1000C iron powder + 1% Acrawax C

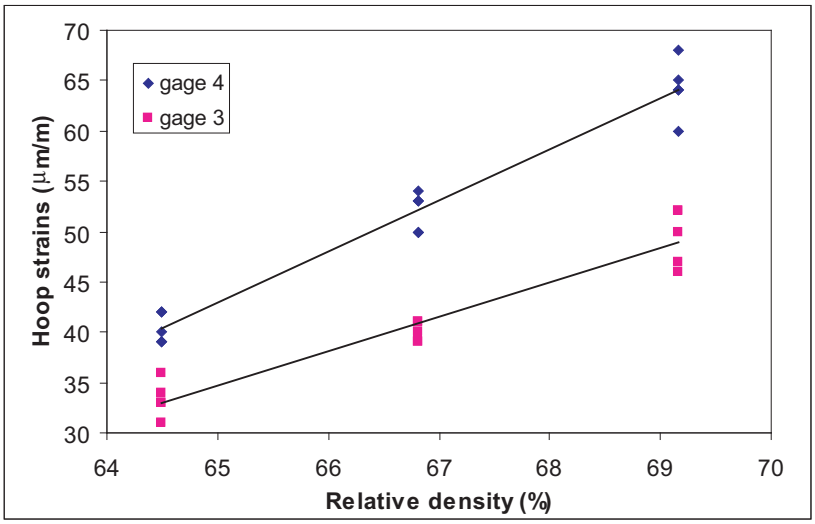

(b) 316L stainless steel powder + 1% Acrawax C

Figure 5.6. Variation of hoop strains with relative density of compact

Equal amount of the admixed powders (50 g) was used for compacting all the samples. The A1000C iron powder samples were compacted to bulk relative densities ranging from 70% to 77% while the 316L stainless steel powder samples were compacted in the bulk relative density range of 64% to 70%. The lower density range for the stainless steel powder compacts was limited by the rigidity of the experimental die. After compacting the sample

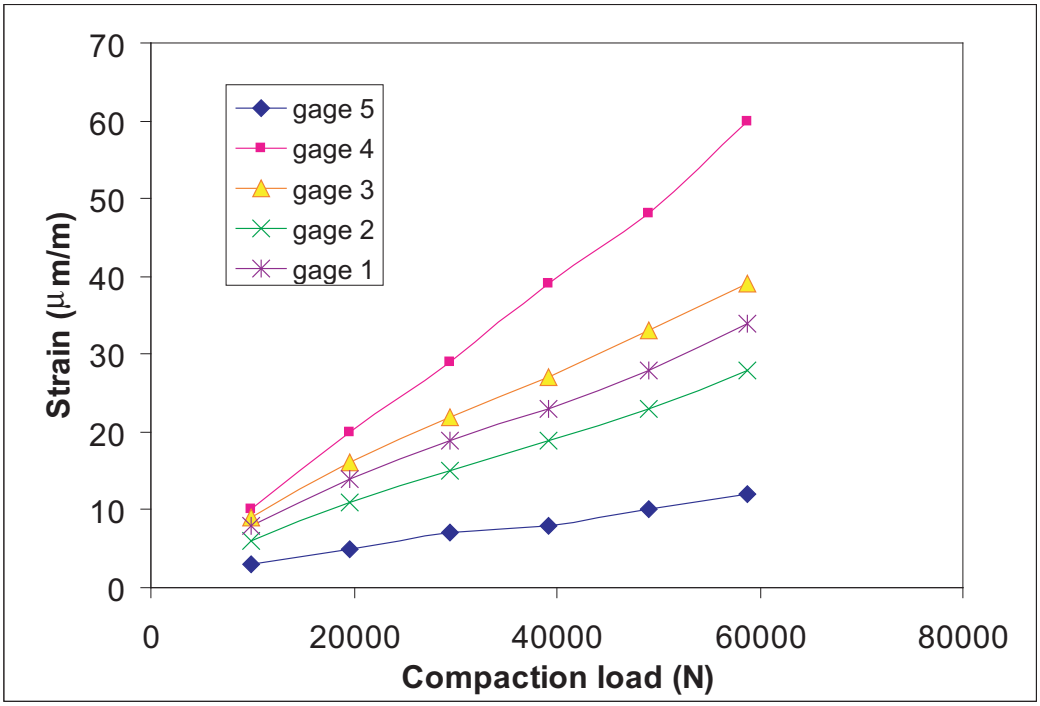

Figure 5.7. Variation of hoop strains with compaction load

to the final bulk relative density, the hoop strains were measured in the strain gages by switching through the different channels on the switch and balance unit.

Figures 5.6(a) and (b) show the variation of hoop strains recorded in strain gages 3 and 4 with the relative density of compaction for the two powder systems. At the final bulk relative density the top surface of the powder compact was below the plane in which the strain gage 5 was located. Hence no radial pressure was applied on the inner die wall in the horizontal plane corresponding to location of strain gage 5; therefore gage 5 recorded very little strain corresponding to the instrument error.

Figure 5.7 shows the variation of the hoop strains (μm/m) with the compaction load in the strain gages for the A1000C iron powder system as the samples were compacted to 78% bulk relative density. The variation of strains along the height of the die wall can be seen from this plot. Since the strain gages 1, 2 and 3 are on the same plane, they indicate the error in the measurement of strains using this experimental set-up.

5.4 Numerical Results

The strain measurement experiment described in the previous section was then simulated using the finite element method. The finite element mesh shown in Figure 5.2(a) was used to simulate the die compaction. The height of the initial powder column was calculated corresponding to the tap density for 50 g of powder. The failure surface parameters, material cohesion (d) and material angle of friction (β), determined from the combination of the Brazilian disk test and uniaxial compression test were the input. The failure surface parameters were varied with the volumetric strain (ε_{vol}^{pl}) corresponding to the variation of the failure surface parameters with relative density as determined from the test (Figures 4.10(a) and (b)). Literature studies (Sinka et al., 2003), (Doremus et al., 2001) indicate that the cap eccentricity parameter varies with density. However for the purposes of this research, the parameter was assumed to be a constant since the aim of the numerical experiment was to determine the approximate value of this parameter for a given powder system. Hence, the cap eccentricity parameter was kept constant for a single experiment and was varied from experiment to experiment until the numerically predicted hoop strains on the outer die wall elements matched the physically measured hoop strains at the locations where the strain gages 3 and 4 were mounted. This process was used to determine the cap eccentricity parameter for the two metal powders (A1000C iron and 316L stainless steel powders with 1% Acrawax C).

5.4.1 A1000C Iron Powder + 1% Acrawax C

Figures 5.8(a), (b) and (c) show the variation of the predicted maximum and minimum relative density gradients with the cap eccentricity parameter with all the other material parameters fixed for parts compacted to 72%, 75% and 77% bulk relative densities respectively. It can be seen that a higher value of the cap eccentricity parameter predicts a larger density gradient.

Figures 5.9(a), (b) and (c) show the variation of the predicted hoop strains on the outer die

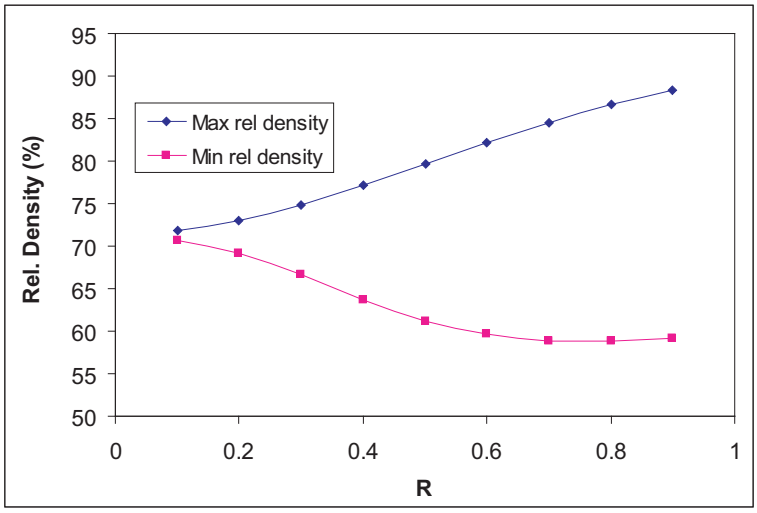

(a) 72% bulk relative density

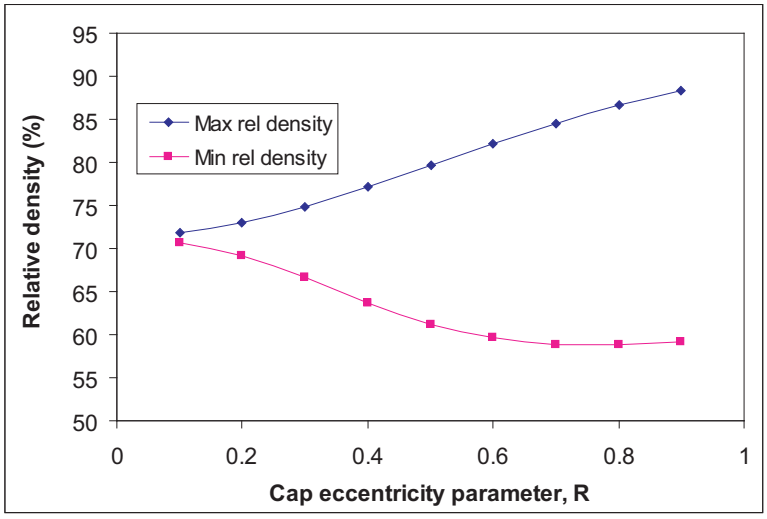

(b) 75% bulk relative density

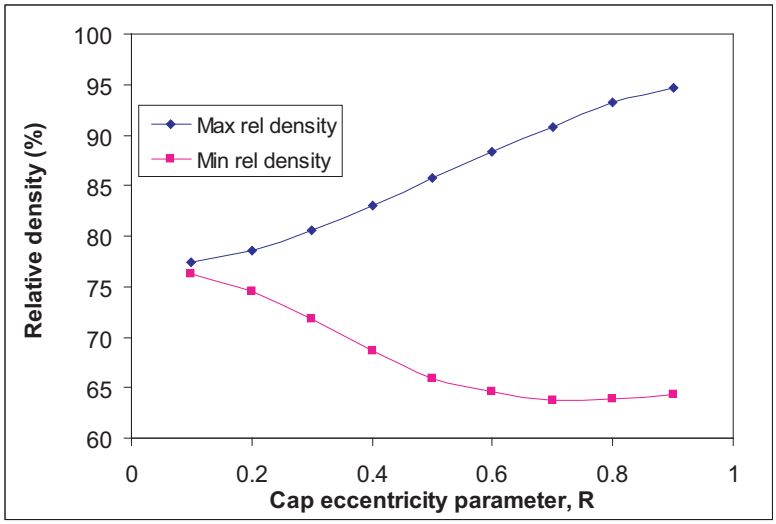

(c) 77% bulk relative density

Figure 5.8. Predicted density gradient variation with R for A1000C

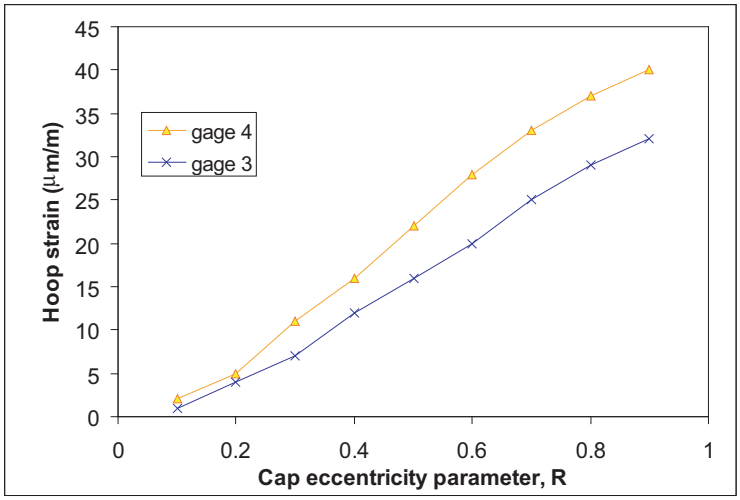

(a) 72% bulk relative density

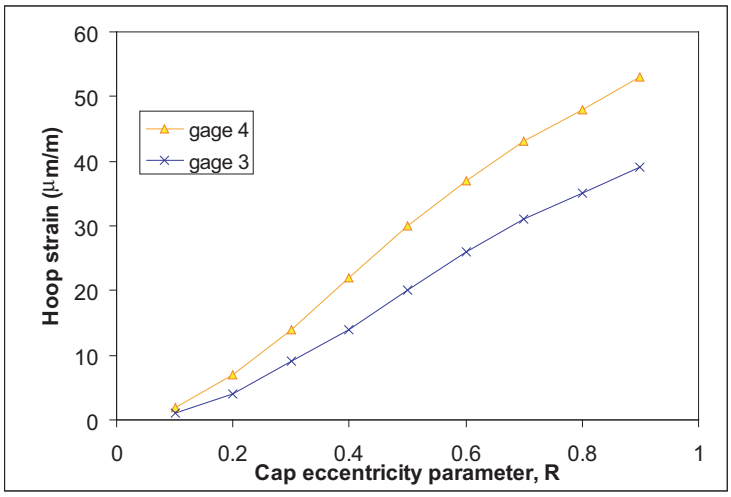

(b) 75% bulk relative density

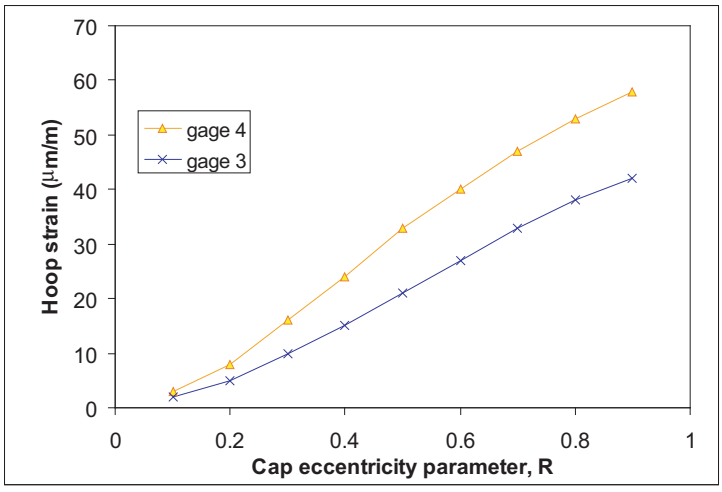

(c) 77% bulk relative density

Figure 5.9. Predicted hoop strain variation with R for A1000C

wall at the nodes corresponding to the location of strain gages 3 and 4 in the experimental set-up (Figure 5.4) at the end of compaction of parts with 72%, 75% and 77% bulk relative densities respectively.

Figure 5.10(a) and (b) shows the comparison of the experimentally determined hoop strains for A1000C iron powder with 1% Acrawax C with the numerically predicted hoop strains for different values of the cap eccentricity parameter at the strain gage locations for gage 3 and gage 4. This indicates that the value of the cap eccentricity parameter, R, lies in the range of 0.8 - 0.9 for the iron powder in the density range of 70% - 80%.

5.4.2 316L Stainless Steel Powder + 1% Acrawax C

Figures 5.11(a), (b) and (c) show the variation of the predicted maximum and minimum relative density gradients with the cap eccentricity parameter with all the other material parameters fixed for parts compacted to 64%, 67% and 69% bulk relative densities respectively. Again the difference between the maximum and the minimum predicted relative densities in the compact increases with the cap eccentricity parameter.

Figures 5.12(a), (b) and (c) show the variation of the predicted hoop strains on the outer die wall at approximate location of strain gages 3 and 4 in the experimental set-up (Figure 5.4) at the end of compaction of parts with 64%, 67% and 69% bulk relative densities respectively.

Figure 5.13(a) and (b) shows the comparison of the experimentally determined hoop strains for 316L stainless steel powder with 1% Acrawax C with the numerically predicted hoop strains for different values of the cap eccentricity parameter at the strain gage locations for gage 3 and gage 4. This indicates that the value of the cap eccentricity parameter, R, lies in the range of 0.5 and 0.6 for the stainless steel powder for the experimental density range.

From the results for both metal powders, it can be concluded that the alternative method using a combination of numerical and simple physical experiments can be used to get an es-

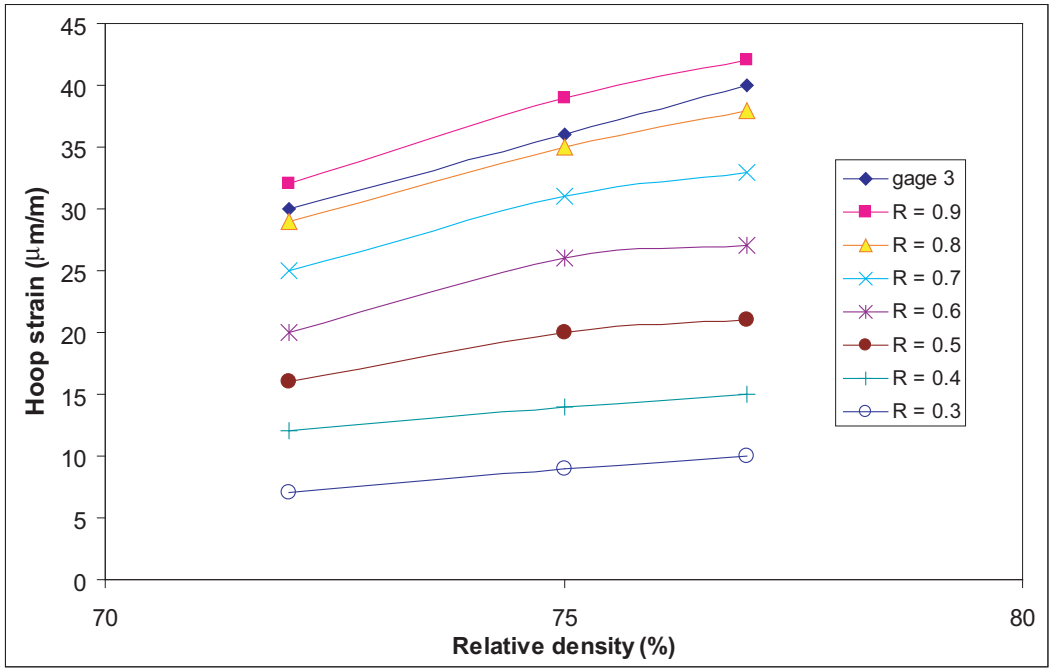

(a) Strain gage 3 location

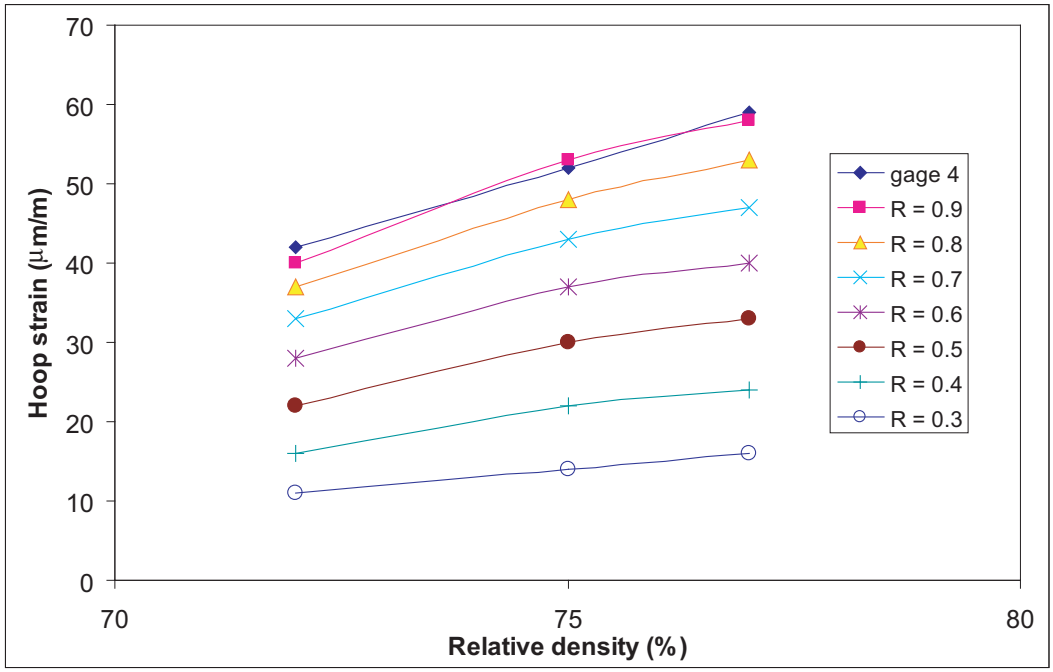

(b) Strain gage 4 location

Figure 5.10. Experimental vs numerical hoop strains for A1000C iron powder

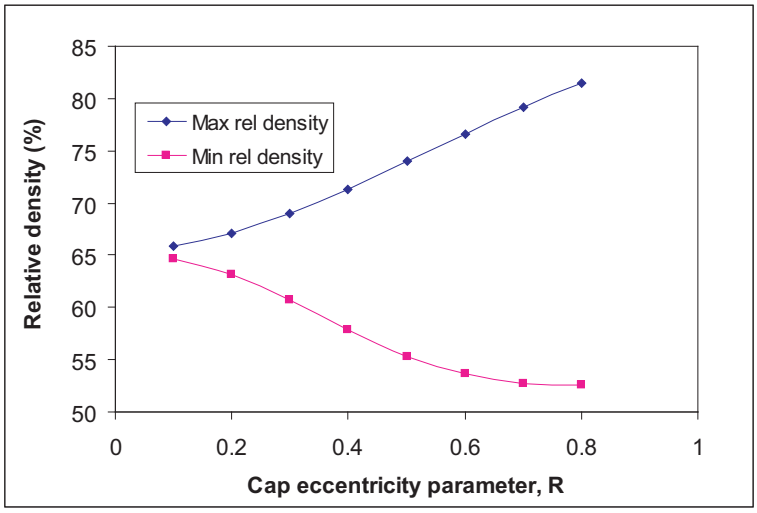

(a) 64% bulk relative density

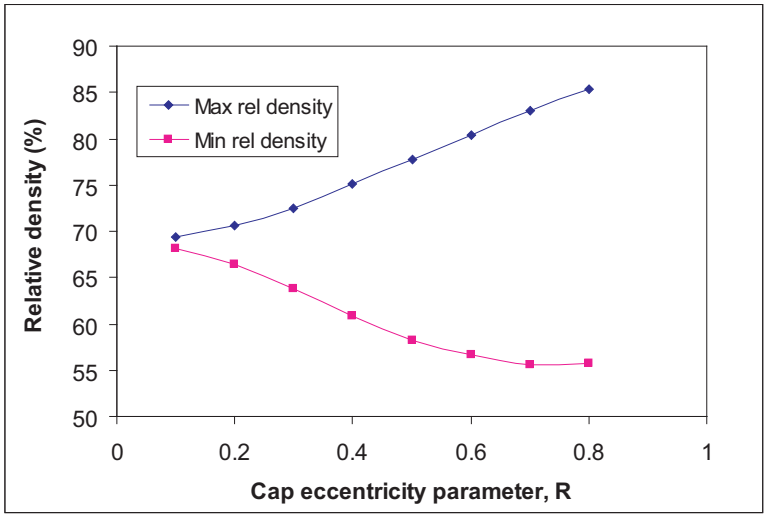

(b) 67% bulk relative density

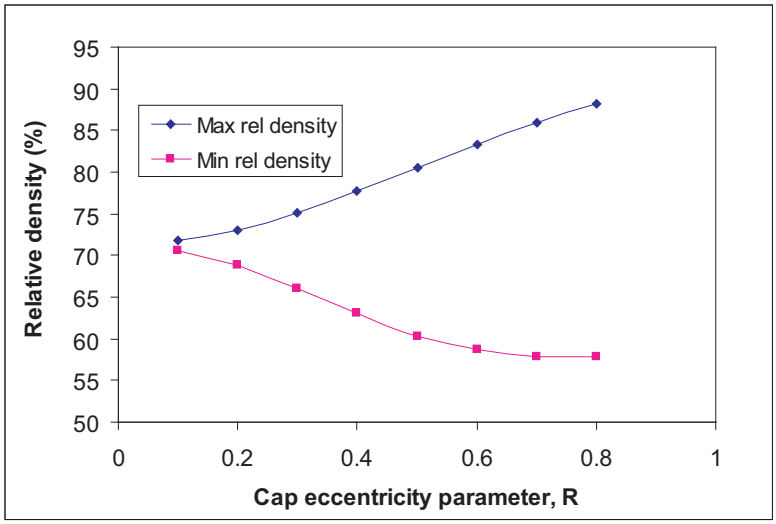

(c) 69% bulk relative density

Figure 5.11. Predicted density gradient variation with R for 316LSS

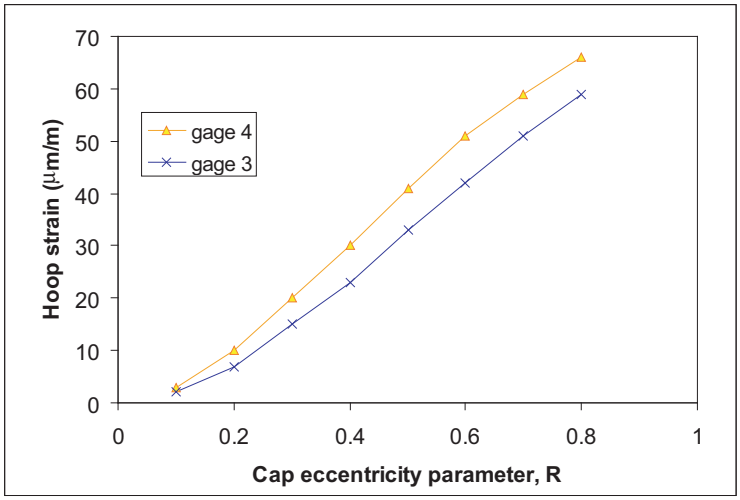

(a) 64% bulk relative density

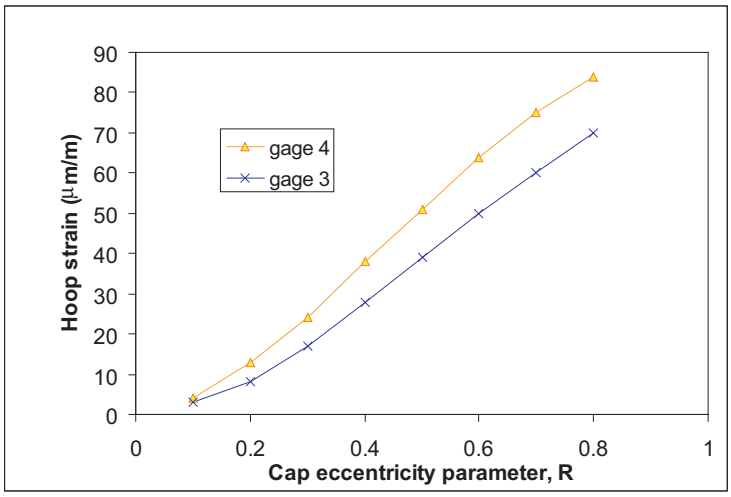

(b) 67% bulk relative density

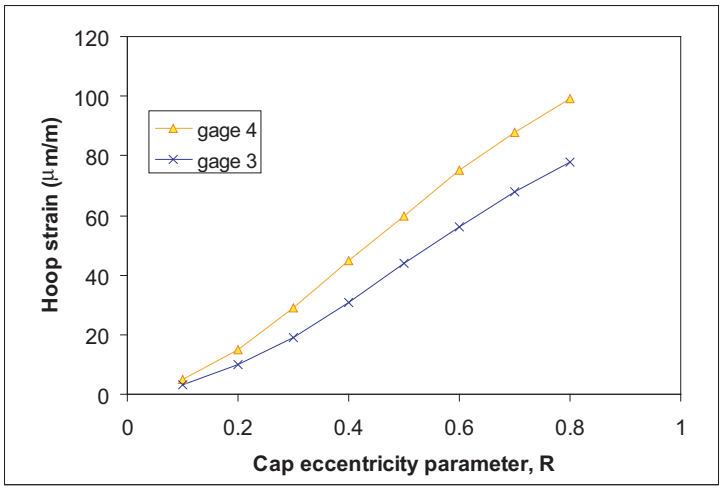

(c) 69% bulk relative density

Figure 5.12. Predicted hoop strain variation with R for 316LSS

timate of the cap eccentricity parameter for the densities at which the tests are performed. While the technique is not as robust as the triaxial test, the experiments can be easily performed at very low cost and without a sophisticated experimental set-up. Values of R = 0.9 for A1000C iron powder and R = 0.5 for 316L stainless steel powder are used in the numerical model to predict the density gradients in compacted parts made from these powders.

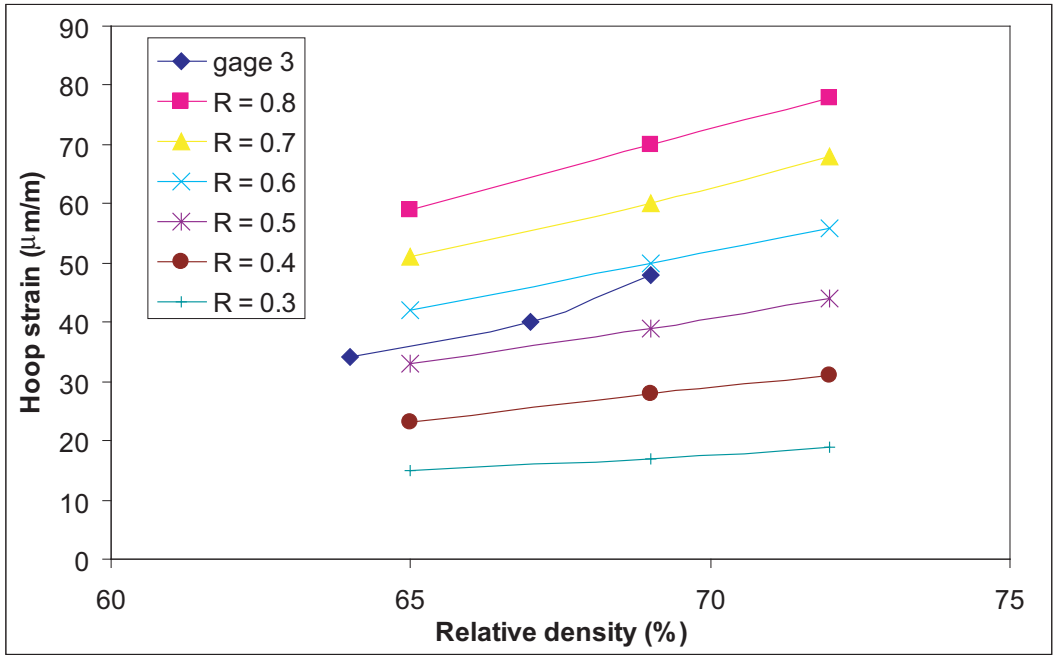

(a) Strain gage 3 location

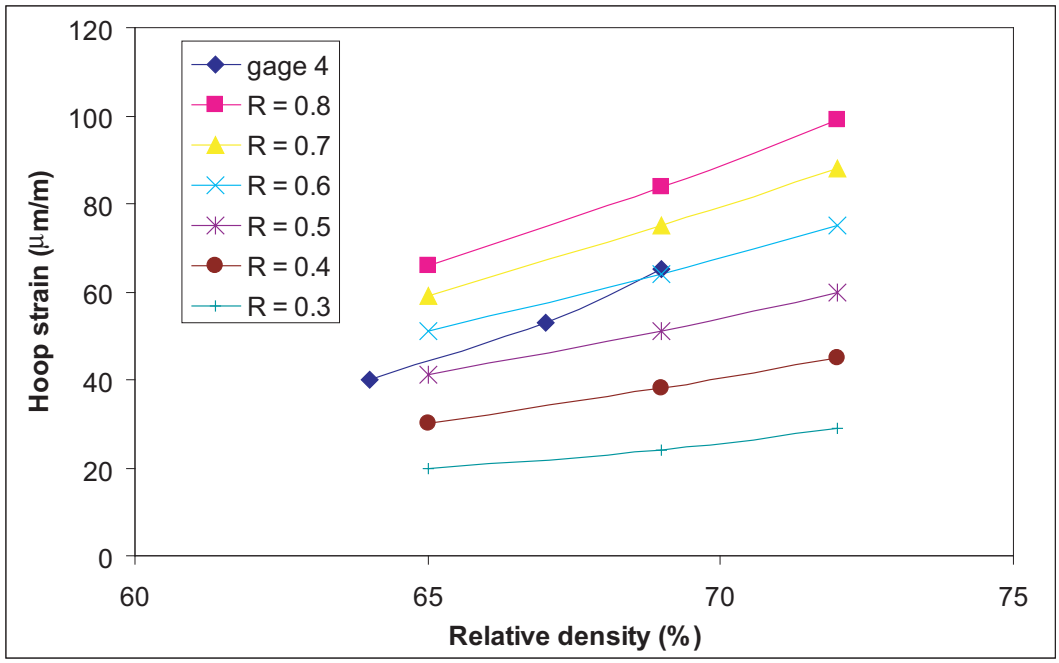

(b) Strain gage 4 location

Figure 5.13. Experimental vs numerical hoop strains for 316L stainless steel powder

Chapter 6

Numerical Model Verification

6.1 Introduction

A numerical model with the parameters characterized using the alternative testing methods described in previous sections is verified for application to predict density gradients in a die compacted part by comparing the numerically predicted density distribution to the density field obtained from physical measurements.

6.2 Experimental Density Distribution

Different techniques have been developed to experimentally determine the local density in a green part. Weber and Brown (1992) and Riera and Prado (1994) have used the micro-hardness testing technique by correlating hardness to the density of the material. Hersey et al. (2000) used an ultrasonic tomography technique to analyze the density distribution in green iron parts. In this research, the experimental density data was obtained from Wagle (2000), He (2002) and Gurson and Bono (1996). The techniques used by the respective work is described briefly along with the experimental results in the following subsections.

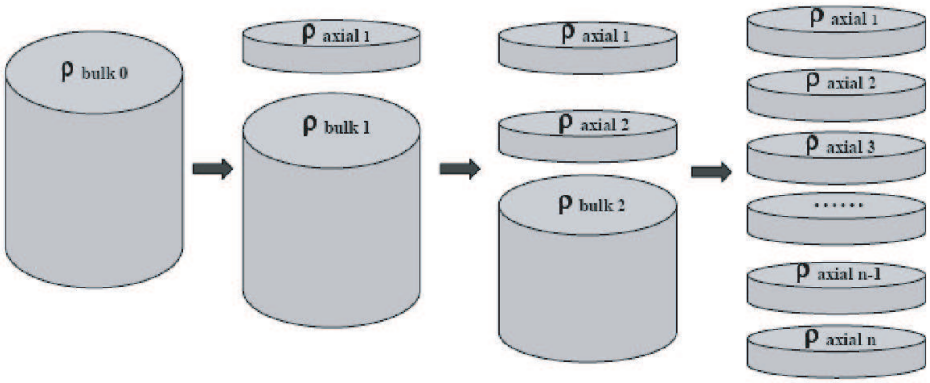

(a) Axial density measurement

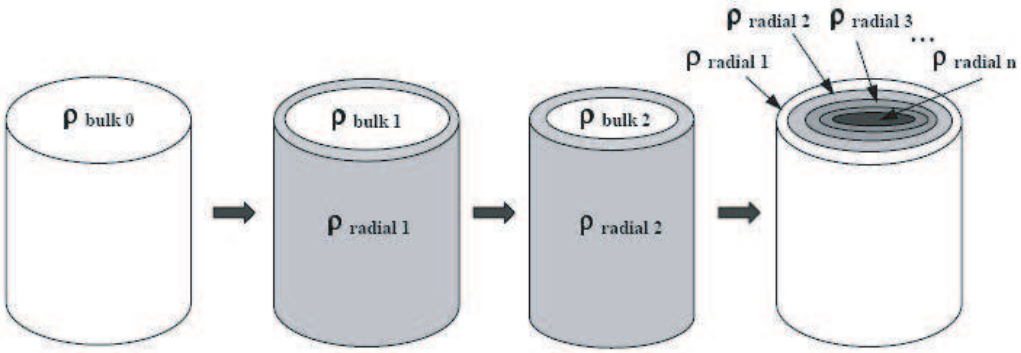

(b) Radial density measurement

Figure 6.1. Schematic of the density measurement technique(Ref: Wagle (2000)

6.2.1 Wagle (2000)

Wagle (2000) used a mass/volume measurement technique by machining green parts made with Hoeganaes A1000C iron powder using a double compaction process. Axial and radial layers of the specimen were machined using axial grinding and turning. The mass and volume of each removed layer were measured to determine the densities of the removed layer. To facilitate machining of the compacts, the green parts were pre-sintered in a reducing atmosphere at 700°C prior to machining. Figures 6.1(a) and (b) show a schematic of the density measurement procedure using the machining technique (Ref: Wagle (2000)). The axial and radial density plots were then combined using a reconstruction algorithm developed by Hersey et al. (2000) to provide a 3-dimensional density field for the specimen.

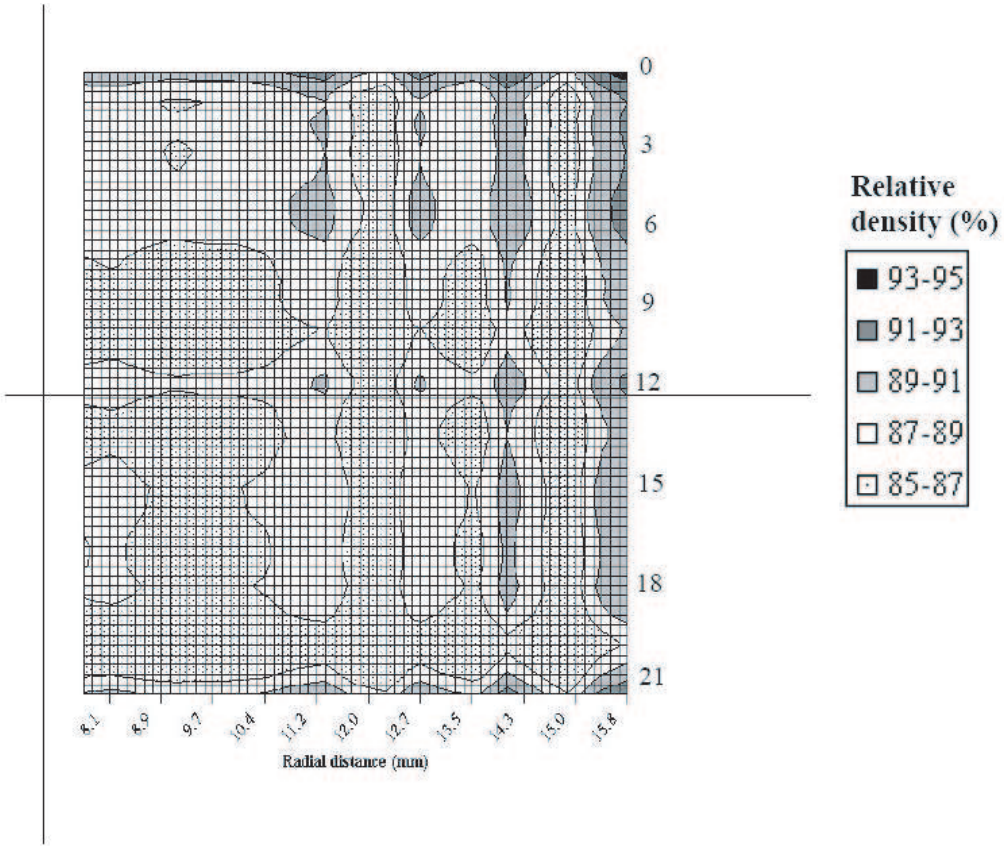

Figure 6.2. Physical density plot in 87% bulk density iron compact(Ref: Wagle (2000))

Due to constraints in machining, the physical density plots were determined for only a part of the compact. Figure 6.2 shows the physical density plot for a green iron powder compact with a bulk relative density of 87%. The maximum relative density of 95% was determined at the corner with the die and the upper punch while the bulk of the part shows a density of 87%.

6.2.2 He (2002)

He (2002) used an optical image analysis technique to measure the local density in a compact made with *Höganäs* 316L stainless steel powder. The area fraction of porosity on a cut and polished sample surface was correlated to the density in a part. The green compacts were presintered in an environment of hydrogen to provide strength to the compact

for the cutting and polishing operations. Three sections which are 1/8 of the cylindrical specimen were measured for each sample. The cut surfaces were mounted in epoxy and the surface was ground and polished. An image analysis software was used to measure the area fraction which was used to get the physical density plots.

It was determined that the maximum density occurred at the corner formed by the punch face and the die wall for each surface measured. Areas near the midpoint along the die wall indicated lower density. For a stainless steel powder compact with bulk relative density of 79% a density gradient of 74% - 84% was measured by this technique. It was seen that a density gradient of 74% - 84% was measured close to the die wall, away from the wall, a density gradient from 78% to 81% was noted.

6.2.3 Gurson and Bono (1996)

An incremental machining method was also employed by Gurson and Bono (1996). Ancorsteel AS1000 steel powder (with 0.75% Acrawax C lubricant) compacted cylindrical specimen with a diameter of 19.05 mm (0.75 in) and a final height of 19.05 mm (0.75 in) was used in the machining procedure. The specimen was set in a lathe and a small ring of 1.5875 mm (0.0625 in) radial and axial length was machined off. The mass of the specimen before and after machining was recorded to calculate the average density of the ring. The process was repeated to get a density mapping of the specimen. The density plot was obtained for the bulk of the specimen except the center section due to difficulty of accurate machining at smaller radii.

The density plot obtained by this machining technique for an 83% bulk relative density indicated a density gradient from 75% to 85%. Once again the maximum density was located at the corner of the die wall and punch face.

Table 6.1 summarizes the experimental density gradient data used in this research to validate the numerical model.

Table 6.1. Experimental density distribution data

Reference	**Wagle (2000)**	**He (2002)**	**Gurson and Bono (1996)**
Powder	Hoeganaes A1000C iron	*Höganäs* 316L stainless steel	Ancorsteel AS1000 S steel
Lubricant	1% Acrawax C	1% Acrawax C	0.75% Acrawax C
Diameter (mm)	31.75	31.75	19.05
Fill height (mm)	45	50	40
Compaction	double-action	double-action	single-action
Bulk relative density	87%	79%	83%
Density gradient	85% - 95%	74% - 84%	75% - 85%

6.3 Numerical Simulation of Density Gradients

6.3.1 Finite Element Mesh

To model the cylindrical specimen in die compaction, a simple axisymmetric model was used. The powder compact was modeled using a 300-element mesh made up of axisymmetric 8-noded bi-quadratic elements. The mesh dimensions were prescribed as per the dimensions of the specimen used for experimental density measurement as listed in Table 6.1. The die wall was modeled as a rigid surface. A clearance of 0.001mm was prescribed between the compact and die-wall. The friction between the boundary elements and the die wall was modeled as a friction surface interaction with a classical isotropic Coulomb friction model. Figure 6.3 shows the mesh along with the boundary conditions. For each analysis, half of the cylinder was modeled to account for the symmetry about the longitudinal axis. For double-action compaction equal displacement boundary conditions were specified on both the top and bottom model surfaces while for a single-action compaction, a displacement

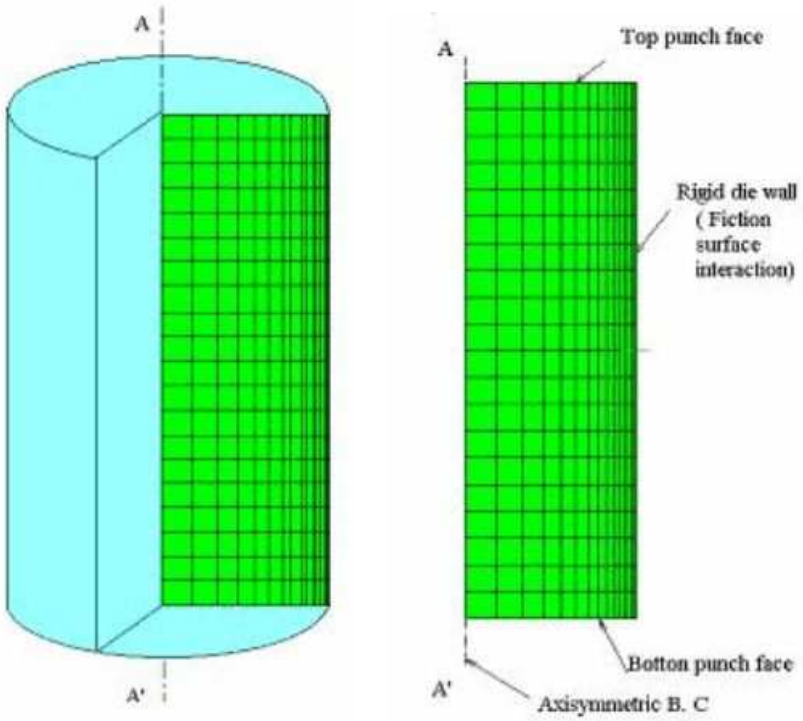

(a) Cylindrical model (b)Finite element mesh

Figure 6.3. ABAQUS finite element mesh to simulate die compaction

boundary condition was prescribed only for the top surface. The boundary displacement was prescribed to simulate die compaction to the desired bulk relative density of the specimen.

6.3.2 Material Parameters

Table 6.2 shows the values of the Drucker-Prager "cap" model parameters used in the simulation. Since the material angle of friction does not vary significantly with density as seen from chapter 4 and is almost same for both iron and stainless steel powders, the failure surface parameters and the cap eccentricity parameter are kept constant for the simulation. Since AS1000 S steel powder is also a water atomized steel powder, the parameters used to define the material are taken same as those obtained for 316L stainless steel using the

Table 6.2. Drucker-Prager "cap" model parameters used in numerical simulation to verify numerical tool against experimental results

Parameters	**Wagle (2000)**	**He (2002), Gurson and Bono (1996)**
Material cohesion, d	0.01 MPa	0.01 MPa
Matl. angle of friction, β	71.5°	71.5°
Cap eccentricity, R	0.9	0.5
Hardening law	A1000C	316L st. steel
Transition parameter, α	0.01	0.01
Initial vol. pl. strain, $\varepsilon_{vol}^{pl}\|_0$	0.01	0.01

the alternate testing methods.

6.3.3 Numerically Predicted Density Distributions

Figure 6.4(a) shows the predicted relative density distribution in a green part compacted numerically as per the specifications of a specimen used to measure the experimental density fields in Wagle (2000) (Table 6.1). The numerical model using the parameters determined using the simple testing technique predicts a density gradient of 74% - 96% for a 87% bulk relative density part. While the maximum relative density and bulk relative density is same as that measured experimentally, the minimum relative density predicted is lower than its experimentally determined counterpart (74% compared to 85%). Figure 6.4(b) shows the corresponding ratio of radial stress to axial stress in the compact predicted by the model. It can be seen that the stress ratio profile matches the density gradient implying that the stress ratio is directly proportional to density of the part.

Using the specifications for compacted specimen from He (2002) (Table 6.1), the numerical model predicts the density distribution shown in Figure 6.5. The relative density range for numerical prediction is 67% - 85% while the experimentally determined density field varied from 74% - 84%. It can also be seen that away from the die wall the density gradient varies from 78% to 81% which is similar to that determined experimentally.

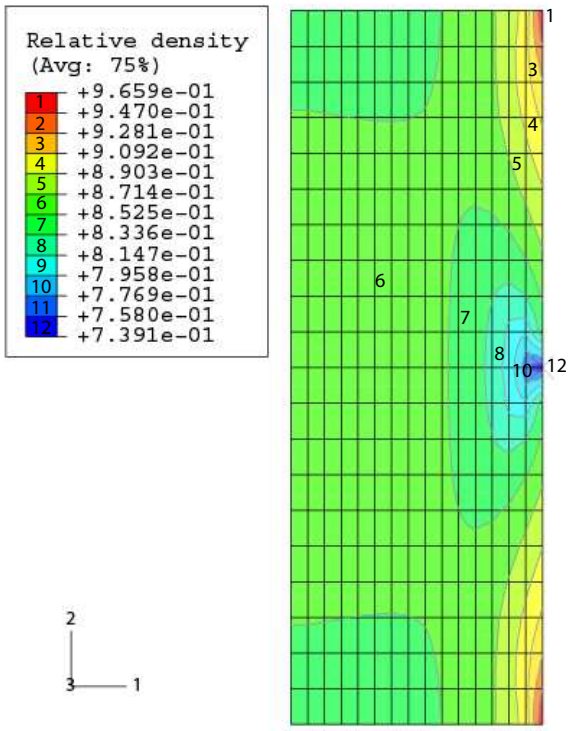

(a) Density distribution

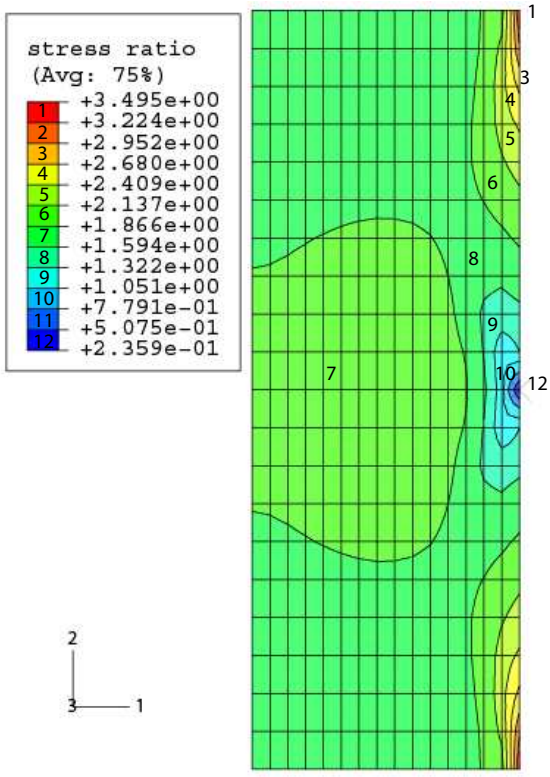

(b) Ratio of radial to axial stress

Figure 6.4. Numerical model predictions for Wagle (2000) green part

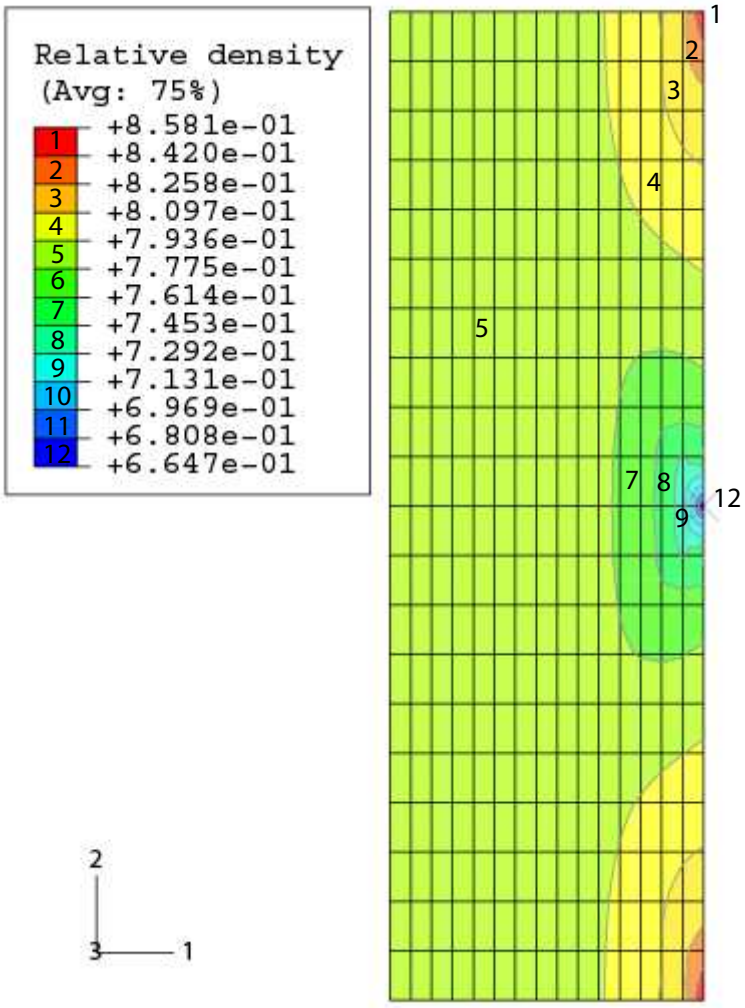

Figure 6.5. Predicted relative density distribution for He (2002) green part

Gurson and Bono (1996) measured a density gradient of 75% - 85% for their 83% bulk relative density single-action AS1000 S steel powder compact. The numerical model using "cap" model parameters determined for 316L stainless steel powder predicts a relative density distribution shown is Figure 6.6. The predicted relative density in the compact varies from 68% - 94% which is a significantly larger range compared to the experimental results. Away from the die wall the density variation is 79% - 85% both numerically as well as experimentally.

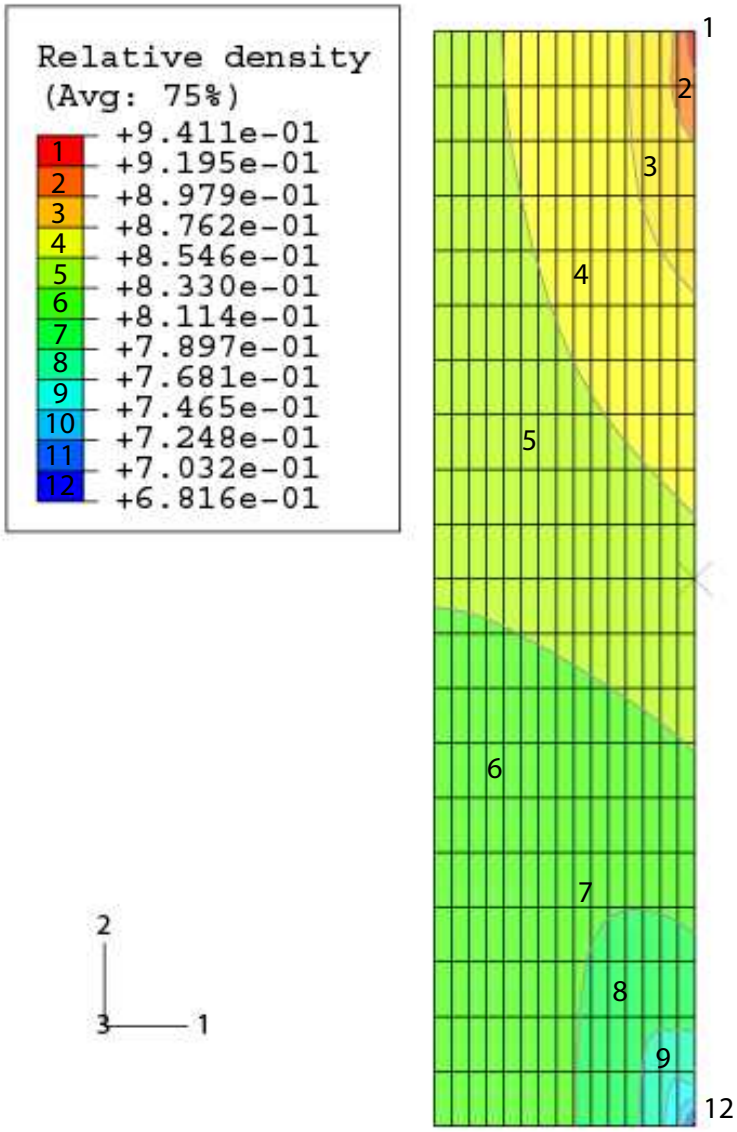

Figure 6.6. Predicted relative density distribution for Gurson and Bono (1996) green part

Table 6.3 summarizes the findings of the verification process for the three cases. It is seen that the numerical model predicts the density gradient with sufficient accuracy for both iron and stainless steel powder compacts.

In summary, the predictive capability is better for the systems that were characterized by the alternate testing techniques used in this research (e.g. A1000C iron powder and 316L

Table 6.3. Numerically predicted densities versus experimentally determined density results

Study	**Wagle (2000)**		**He (2002)**		**Gurson and Bono (1996)**	
Material	A1000C iron		316L stainless steel		AS1000 S steel	
Relative density	Expt.	Pred.	Expt.	Pred.	Expt.	Pred.
bulk	87	87	79	79	83	83
max. (%)	95	96	84	85	85	94
min. (%)	85	74	74	67	75	68

stainless steel powder). Specifically the numerically predicted maximum relative density and bulk relative density are in good agreement with the physical measurements whereas the numerical model underestimates the predicted minimum relative density compared to the actual minimum. Possible sources of error may be accounted for by

- Error in experimental density measurement technique for lower relative densities. These could be attributed to particle pull out during the machining process.
- Extreme sensitivity of the numerical model to the cap eccentricity parameter, R, which is assumed constant but which may vary with density.

Chapter 7

Conclusions and Recommendations

Numerical modeling of the powder metallurgy die compaction process provides a cost-effective and efficient method to establish protocols to attain desired compact properties. Constitutive material models developed to study soil behavior under consolidation loads can be used to define the behavior of the material under compaction loads. The modified Drucker-Prager "cap" model with a plastic shear failure surface and work hardening yield surfaces that evolve with plastic volumetric strain can describe the loose powder response and the particle deformation. The Drucker-Prager "cap" model was used to predict density gradients in a green part and an efficient technique was developed to characterize the material model parameters for industrial applicability of the numerical tool. The testing protocol is presented here along with suggestions for future work in developing the tool.

7.1 Conclusions

Water atomized A1000C iron powder and 316L stainless steel powder were selected for this research due to their wide industrial application. A numerical model using the modified Drucker-Prager "cap" plasticity model has been formulated in the commercially available finite element software ABAQUS (2001) to model the die compaction process. While the model is formulated for a simple axisymmetric geometry, it can be easily extended to more complex geometries. The complex material model that describes the response of powder through the compaction process has been discussed to illustrate its origin and describe its current use for powder compaction. A procedure for conducting numerical sensitivity

analysis of the parameters that define the model has been developed to identify the parameters that are significant in predicting density gradients. The procedure allowed for the interaction effects between model parameters to be studied. Since the model surfaces interact, this sensitivity analysis is more robust and practical than an analysis determining the sensitivity for one parameter at a time. The analysis indicates that out of the seven parameters that are needed to define the model, the density field prediction is most sensitive to only two of the parameters, namely the cap eccentricity parameter, R, and the material angle of friction, β.

The recommended testing method to determine the model parameters is the triaxial testing method and the hydrostatic compression test. Since the methods are expensive and difficult to perform, simple alternative testing methods proposed by researchers were investigated for ease in industrial application. The alternative test method proposed by Coube and Riedel (2000) was used to characterize the failure surface for the two metal powders. The results indicate that the material cohesion, d, increases with density but one of the identified significant parameter, the material angle of friction (β) does not vary much with density. Also the parameter does not vary significantly between the two material systems.

Alternate testing methods proposed to the triaxial tests for characterization of the yield surfaces in literature suggest the use of instrumented dies, i.e. dies equipped with internal load cells or sensors to measure the radial stresses developed during compaction. A simpler testing method involving a combination of numerical and physical experiments has been developed. The experimental set-up uses low-cost commercially available strain gages mounted on the outer surface of the die wall to measure hoop strains during die compaction. The numerical experiment simulates the die compaction process in this test. The unknown cap eccentricity parameter, R, is varied until the predicted hoop strain matched the physically measured value. The technique was implemented for the iron and stainless steel powders to determine the cap eccentricity parameter.

Table 7.1 lists the values of the material parameters for A1000C iron powder and 316L stainless steel powder. Numerically predicted density gradients for green parts compacted using the listed parameters for the two materials show a remarkable consistency with the experimentally measured density field distributions. Based on results of this research, a

Table 7.1. Drucker-Prager "cap" model parameters for A1000C iron powder and 316L stainless steel powder

Parameters	**A1000C iron powder**	**316L stainless steel powder**
Material cohesion, d	0.01 MPa	0.01 MPa
Material angle of friction, β	71.5°	71.5°
Cap eccentricity, R	0.9	0.5
Hardening law	Figure 7.1(a)	Figure 7.1(b)
Transition parameter, α	0.01	0.01
Initial vol. pl. strain, $\varepsilon_{vol}^{pl}\|_0$	0.01	0.01

simple test protocol has been developed for characterizing the material parameters for defining the Drucker-Prager "cap" model for any given powder material as shown in Figure 7.2. Comparisons between the simulation and experimental results in association with detailed understanding of the parameters that define the model helps provide a robust numerical finite element model for simulating the die compaction process for iron and stainless steel powders.

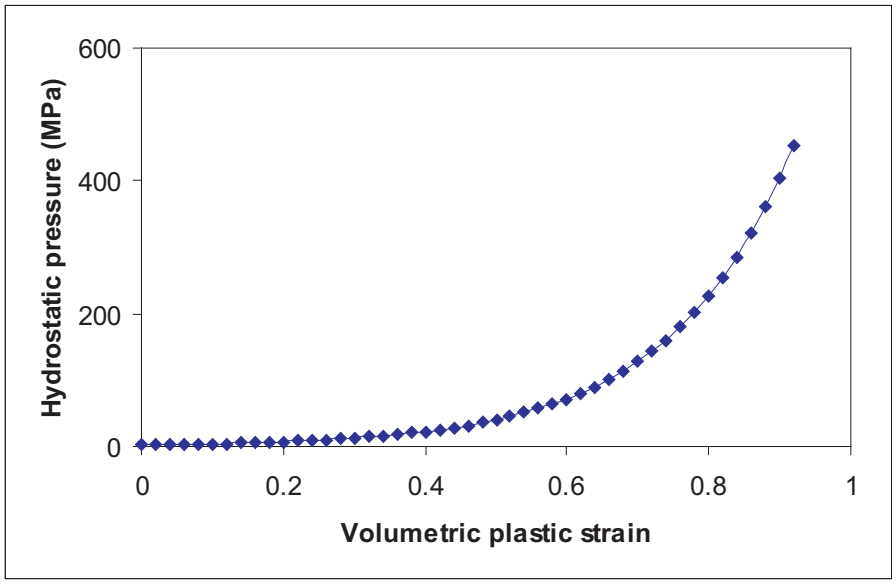

(a) A1000C iron powder

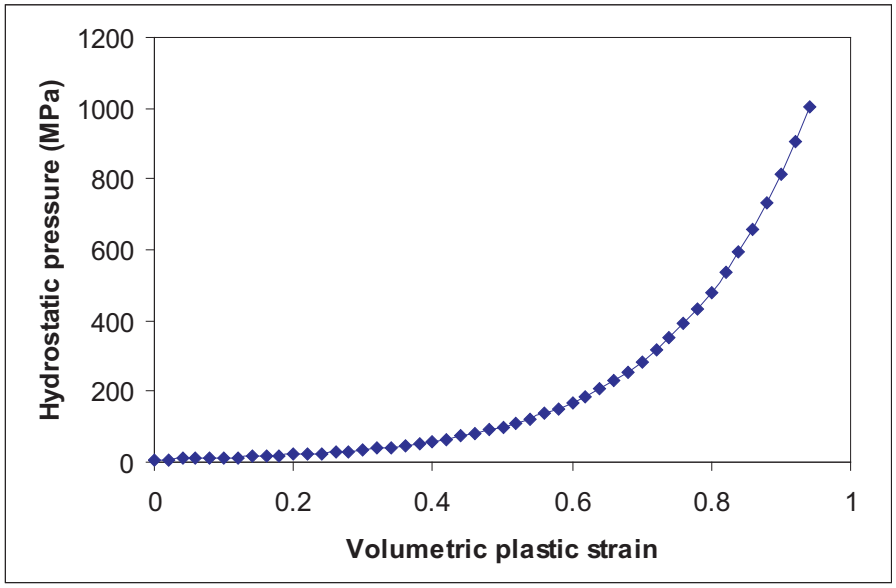

(b) 316L stainless steel powder

Figure 7.1. Hardening law used in Table 7.1

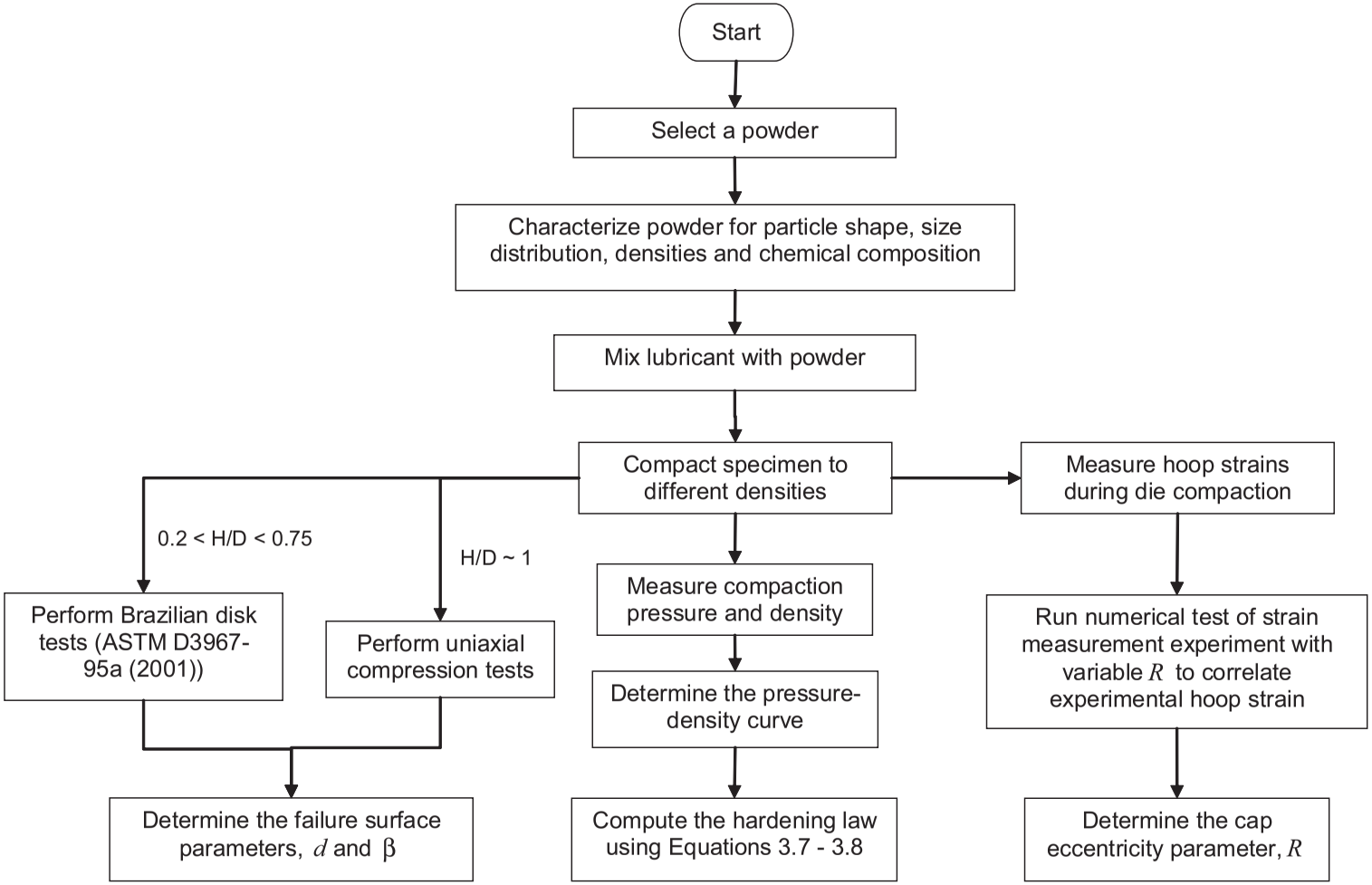

Figure 7.2. Proposed test protocol for characterizing material parameters for Drucker-Prager "cap" model

7.2 Recommendations for Future Work

The experimental set-up using strain gages was shown to be an efficient method of determining the material parameters. However the set-up has inherent limitations. The die was designed so that it was rigid enough to provide a radial constraint during the die compaction process but at the same time flexible enough to undergo elastic strains. This limited the compaction load that could be applied and hence the density of compacts. As seen from the data the 316L stainless steel powder could be characterized only at low densities. In order to increase the range of density (compaction load), a slightly more rigid die needs to be designed. This would cause the induced hoop strains to be lower. In such a case the accuracy of the strain measurement technique will need to be improved by possibly using a bridge amplifier. Mounting more strain gages on the die wall and measuring the continuous variation of strain data with compaction loads instead of the discrete strain recordings in this work would lead to lot more data points that can be compared with the numerical experiments to give a better characterization of the cap eccentricity parameter and its variation with density.

The protocol needs to be applied to a wider range of powders to verify and refine the technique. Further research work is suggested on the study of the relation between the the model parameters and the powder characteristics such as particle shape, size, etc. to provide possible correlations that could further reduce the number of tests to characterize the parameter for families of powder materials.

Parts with complex geometry often develop cracks due to high stresses that are introduced early in the manufacturing, specifically during compaction. Appendix B shows evidence of the benefits to applying knowledge of the load paths and constitutive parameters when specifying tool motions for numerically compacting complex. Two different tool motions are numerically applied to predict the density and stress fields for a complex part. A clear understanding of the constitutive model and the material response in the critical regions in complex shapes can assist in tool designs and processing protocols. Therefore, additional research to investigate the use of the numerical tool to optimize tool design and process specification for three-dimensional applications with complex geometric shapes is recommended. Ideally, three-dimensional applications with complex geometric shapes for which

experimental density distribution data is readily available could be considered in the next set of investigations.

Bibliography

ABAQUS. *Standard User's Manual*. Hibbitt, Karlsson and Sorensen, Inc., Rhode Island, 2001.

ASTM Standard D3967-95a. Standard Test Method for Splitting Tensile Strength of Intact Rock Core Specimens. *ASTM*, 2001.

ASTM Standard D4767-95. Standard Test Method for Consolidated Undrained Triaxial Compression for Cohesive Soils. *ASTM*, 1995.

I. Aydin, B. J. Briscoe, and K. Y. Sanhturk. The Internal Form of Compacted Ceramic Components: A Comparison of a Finite Element Modelling with Experiment. *Powder Technology*, 89:239–254, 1996.

A. P. Boresi and O. M. Sidebottom. *Advanced Mechanics of Materials*, chapter 11, pages 492–504. John Wiley & Sons, Inc., New York, N.Y., 4^{th} edition, 1984.

S. Brown and G. Abou-Chedid. Yield Behavior of Metal Powder Assemblages. *Journal of the Mechanics and Physics of Solids*, 42(3):383–399, 1994.

W. F. Chen. *Constitutive Equations for Engineering Materials; Volume 2: Plasticity and Modeling*, chapter 8, pages 1024–1029. Elsevier Science B. V., Amsterdam, The Netherlands, 1994.

H. Chtourou, A. Gakawaya, and M. Guillot. Assessment of the Predictive Capabilities of the Cap Material Model for Simulating Powder Compaction Problems. *Advances In Powder Metallurgy & Particulate Materials*, 7:245–255, 1996.

O. Coube and H. Riedel. Numerical Simulation of Metal Powder Die Compaction with Special Consideration of Cracking. *Powder Metallurgy*, 43:123–131, 2000.

C. S. Desai and H. J. Siriwardane. *Constitutive Laws for Engineering Materials*. Prentice Hall, Inc., Englewood Cliffs, NJ, 1984.

F. L. DiMaggio and I. S. Sandler. Material Model for Granular Soils. *Journal of Engineering Mechanics Division, ASCE*, 97(EM3):935–950, 1971.

P. Doremus, F. Toussaint, and O. Alvain. Simple Tests and Standard Procedure for the Characterisation of Green Compacted Powder. *Proceedings of the NATO Advanced Research Workshop on Recent Developments in Computer Modeling of Powder Metallurgy Processes*, pages 29–41, May 2001.

D. C. Drucker. Some Implications of Work Hardening and Ideal Plasticity. *Quarterly of Applied Mathematics*, 7:411–418, 1950.

D. C. Drucker, R. E. Gibson, and D. J. Henkel. Soil Mechanics and Work-Hardening Theories of Plasticity. *Transactions American Society of Civil Engineers*, 112:338–346, 1957.

D. C. Drucker and W. Prager. Soil Mechanics and Plastic Analysis or Limit Design. *Quarterly of Applied Mathematics*, 10:157–165, 1952.

R. K. Enneti. *Thermal Analysis and Evolution of Shape Loss Phenomena During Polymer Burnout in Powder Metal Processing.* Ph.D. Thesis, The Pennsylvania State University, University Park, PA, 2005.

R. M. German. *Powder Metallurgy Science.* Metal Powder Industries Federation, Princeton, N.J., 2^{nd} edition, 1994.

A. L. Gurson. Continuum Theory of Ductile Rupture by Void Nucleation and Growth: Part I - Yield Criteria and Flow Rules for Porous Ductile Material. *Transactions of the ASME, Journal of Engineering Materials and Technology*, 99:2–15, January 1977.

A. L. Gurson and E. S. Bono. A Modeling System to Simulate the Compaction of Powder Metals. *Advances in Powder Metallurgy & Particulate Materials*, 2:443–455, 1996.

Y. He. Numerical Simulation For 316L Stainless Steel Powder Die Compaction. M.S. Thesis, The Pennsylvania State University, University Park, PA, 2002.

Y. He, R. S. Engel, N. J. Salamon, S. Lindner, and P. Lu. Numerical simulation for 316l stainless steel powder die compaction process. In J. H. Adair, V. M. Puri, K. S. Haris, and C. C. Huang, editors, *Proceedings of the International Conference on Fine Powder Processing Conference*, pages 271–278, 2001.

R. K. Hersey, J. L. Rose, R. S. Engel, and R. M. German. Ultrasonic Tomographic Image Reconstruction of Green and Sintered Powder Metal Compacts. *Proceedings of the 2000 Conference on Powder Metallurgy, PM^{2}TEC 2000*, 2000.

H. A. Kuhn. Uniaxial compression testing. *ASM Handbook*, 8, Mechanical Testing and Evaluation:143–151, 2000.

P. V. Lade. Elasto-Plastic Stress-Strain Theory for Cohesionless Soil with Curved Yield Surfaces. *International Journal of Solids and Structures*, 13:1019–1035, 1977.

D. C. Montgomery. *Design and Analysis of Experiments*. John Wiley, 2001.

E. Pavier and P. Doremus. Triaxial Characterisation of Iron Powder Behaviour. *Powder Metallurgy*, 42(4):345–352, 1999.

W. Prager. Recent Developments in Mathematical Theory of Plasticity. *Journal of Applied Physics*, 20(3):235–241, March 1949.

M. D. Riera and J. M. Prado. Modeling of Cold Compaction Process of Metal Powders. *Proceedings of the 1994 Powder Metallurgy World Congress PM 94, Paris, France*, pages 685–688, 1994.

K. H. Roscoe, A. N. Schofield, and C. P. Wroth. On the Yielding of Soils. *Geotechnique*, 8:22–53, 1925.

J. Secondi. Modeling Powder Compaction from a Pressure-Density Law to Continuum Mechanics. *Powder Metallurgy*, 45(3):213–217, 2002.

S. Shima and M. Oyane. Plasticity Theory for Porous Metals. *International Journal of Mechanical Science*, 18:285–291, 1976.

I. C. Sinka, J. C. Cunningham, and A. Zavaliangos. The Effect of Wall Friction in the Compaction of Pharmaceutical Tablets with Curved Faces: a Validation Study of the DruckerPrager Cap model. *Powder Technology*, 133:33–43, 2003.

S. P. Timoshenko and Goodier. *Theory of Elasticity*, pages 122–127. McGraw Hill, 3^{rd} edition, 1969.

G. S. Wagle. Numerical Investigation Of Constitutive Models For The Powder Compaction Process. M.S. Thesis, The Pennsylvania State University, University Park, PA, 2000.

G. S. Wagle, R. S. Engel, R. M. German, and Y. Liu. Numerical Investigation of Constitutive Models for the Powder Compaction Process. *Advances in Powder Metallurgy and Particulate Materials*, 1:13–24, 2000.

G. G. Weber and S. B. Brown. Simulation of the Compaction of Powder Components. *Advances in Powder Metallurgy & Particulate Materials*, 1:105–118, 1992.

D. H. Zeuch, J. M. Grazier, J. G. Arguello, and K. G. Ewsuk. Mechanical Properties and Shear Failure Surfaces for Two Alumina Powders in Triaxial Compression. *Journal of Materials Science*, 36:2911–2924, 2001.

H. Zipse. Finite-element Simulation of the Die Pressing and Sintering of Ceramic Component. *Journal of the European Ceramic Society*, 17:1707–1713, 1997.

Appendix A

Procedure for Numerical Calculation

A.1 Specifications

- **Finite Element Package:** ABAQUS Version 6.4.2 (Hibbit, Karlsson & Sorensen, Inc.)
- **Platform used:** Microsoft Windows XP edition
- **Hardware specifications:** Dell Computer with Intel Pentium M Processor 725 (1.6GHz) 512 MB RAM, 40GB Harddrive
- **Execution time:** Approximately 4 min

A.2 Sample Input File

```
**********************************************
*HEADING
A1000 C strain measurement
**********************************************
** Node Generation
**********************************************
*NODE
101, 0.0, 0.0, 0.0
```

131, 0.01016, 0.0, 0.0

4101, 0.0, 0.049, 0.0

4131, 0.01016, 0.049, 0.0

2101, 0.0, 0.0245, 0.0

2131, 0.01016, 0.0245, 0.0

151, 0.010161, -0.01272, 0.0

181, 0.03175, -0.01272, 0.0

3751, 0.010161, 0.07632, 0.0

3781, 0.03175, 0.07632, 0.0

1951, 0.010161, 0.0245, 0.0

1981, 0.03175, 0.0245, 0.0

****

** Powder Node Set Generation

****

*NGEN, NSET=BOTTOM

101, 131

*NGEN, NSET=TOP

4101, 4131

*NGEN, NSET=AXIS

101, 4101, 100

*NGEN, NSET=EDGE

131, 4131, 100

*NGEN, NSET=MIDPL

2101, 2131

*NFILL, NSET=ALL, BIAS=1.1

AXIS, EDGE, 30, 1

*NFILL, NSET=ALL, BIAS=1.0

BOTTOM, MIDPL, 20, 100

MIDPL, TOP, 20, 100

****

** Die Generation

****

*NGEN, NSET=DIEBOTTOM

```
151, 181
*NGEN, NSET=DIETOP
3751, 3781
*NGEN, NSET=DIEINNER
151, 3751, 100
*NGEN, NSET=DIEOUTER
181, 3781, 100
*NGEN, NSET=DIEMIDPL
1951, 1981
*NFILL, NSET=DIE, BIAS=0.9
DIEINNER, DIEOUTER, 30, 1
*NFILL, NSET=DIE, BIAS=1.0
DIEBOTTOM, DIEMIDPL, 18, 100
DIEMIDPL, DIETOP, 18, 100
**********************************************
**ELEMENT GENERATION
**********************************************
*ELEMENT, TYPE=CAX8R
101, 101, 103, 303, 301, 102, 203, 302, 201
*ELGEN, ELSET=ALL
101, 15, 2, 1, 20, 200, 100
**********************************************
**ELEMENT SET GENERATION
**********************************************
*ELSET, ELSET=EDGE, GENERATE
115, 2015, 100
*ELSET, ELSET=BOT, GENERATE
101, 115, 1
*ELSET, ELSET=TOP, GENERATE
2001, 2015, 1
**********************************************
**DIE ELEMENT SET GENERATION
**********************************************
```

*ELEMENT, TYPE=CAX8R

151, 151, 153, 353, 351, 152, 253, 352, 251

*ELGEN, ELSET=DIEALL

151, 15, 2, 1, 18, 200, 100

*ELSET, ELSET=DIEOUTER, GENERATE

165, 1865, 100

*ELSET, ELSET=DIEINNER, GENERATE

151, 1851, 100

*ELSET, ELSET=DIEBOT, GENERATE

151, 165, 1

*ELSET, ELSET=DIETOP, GENERATE

1851, 1865, 1

*ELSET, ELSET=STR6

465, 565

*ELSET, ELSET=STR9

765, 865

*ELSET, ELSET=STR10

1065, 1165

****

**FRICTION BOUNDARY CONDITION SPECIFICATION

****

*SURFACE, NAME=POWDEREDGE

EDGE, S2

*SURFACE, NAME=DIE

DIEINNER, S4

*CONTACT PAIR, INTERACTION=DIEROUGH

POWDEREDGE, DIE

*SURFACE INTERACTION, NAME=DIEROUGH

*FRICTION

0.4

****

** DIE MATERIAL PROPERTY DEFINITION

****

```
*SOLID SECTION, ELSET=DIEALL, MATERIAL=DIEWALL
*MATERIAL, NAME=DIEWALL
**ELASTIC PROPERTIES
*ELASTIC
2.1E11, 0.3
**********************************************
**INITIAL CONDITION
**********************************************
**APARENT DENSITY
*INITIAL CONDITIONS, TYPE=RATIO
ALL,1.5
*INITIAL CONDITIONS, TYPE=STRESS, GEOSTATIC
ALL, -500, 0.0, -500, 0.049, 1.0
**********************************************
**MATERIAL PROPERTY DEFINITION
**********************************************
*SOLID SECTION, ELSET=ALL, MATERIAL=SOIL
*MATERIAL, NAME=SOIL
**ELASTIC PROPERTIES
*POROUS ELASTIC
0.01, 0.29
**PLASTIC PROPERTIES
*CAP PLASTICITY, DEPENDENCIES = 1
1.0E6, 71.5, 0.5, 0.01, 0.01, 1.0, , 0.0
3.0E6, 71.05, 0.5, 0.01, 0.01, 1.0, , 0.35
5.9E6, 70.55, 0.5, 0.01, 0.01, 1.0, , 0.55
*CAP HARDENING
1.957E6,0
2.196E6,0.02
2.465E6,0.04
2.766E6,0.06
3.104E6,0.08
3.484E6,0.1
```

3.909E6,0.12

4.387E6,0.14

4.924E6,0.16

5.526E6,0.18

6.201E6,0.2

6.960E6,0.22

7.811E6,0.24

8.766E6,0.26

9.837E6,0.28

11.040E6,0.3

12.390E6,0.32

13.905E6,0.34

15.605E6,0.36

17.513E6,0.38

19.654E6,0.4

22.057E6,0.42

24.753E6,0.44

27.780E6,0.46

31.176E6,0.48

34.988E6,0.5

39.266E6,0.52

44.067E6,0.54

49.455E6,0.56

55.501E6,0.58

62.287E6,0.6

69.902E6,0.62

78.449E6,0.64

88.040E6,0.66

98.804E6,0.68

110.885E6,0.7

124.442E6,0.72

139.657E6,0.74

156.732E6,0.76

175.894E6,0.78

197.400E6,0.8

221.535E6,0.82

248.620E6,0.84

279.017E6,0.86

313.131E6,0.88

351.416E6,0.9

394.381E6,0.92

442.600E6,0.94

496.714E6,0.96

557.444E6,0.98

625.600E6,1

*USER DEFINED FIELD

*DEPVAR

1

****

*BOUNDARY

DIEBOTTOM, 2

AXIS, XSYMM

BOTTOM, 2

****

*STEP, NLGEOM, UNSYMM=YES, INC=1000

*STATIC

0.05, 10.0

*CONTROLS, PARAMETERS=TIME INCREMENTATION

90, 500, , , , , 80

*CONTROLS, PARAMETERS=LINE SEARCH

4

*BOUNDARY

TOP, 2, , -0.0215

*OUTPUT, FIELD, FREQUENCY=1

*ELEMENT OUTPUT, ELSET=ALL

VOIDR, S

```
*ELEMENT OUTPUT, ELSET=DIEALL
E, S, EE
*NODE OUTPUT, NSET=ALL
U, RF, CF
*NODE PRINT, NSET=TOP, FREQUENCY=10
U2
*ELPRINT, ELSET=ALL, FREQUENCY=10
VOIDR
*ELPRINT, ELSET=STR6, POSITION= AVERAGED AT NODES, FREQUENCY=10
S33, E33
*ELPRINT, ELSET=STR9, POSITION= AVERAGED AT NODES, FREQUENCY=10
S33, E33
*ENDSTEP
**********************************************
```

A.3 User subroutine for parameter variation with volumetric strain

```
      subroutine usdfld(field,statev,pnewdt,direct,t,celent,time,dtime,
     1      cmname,orname,nfield,nstatv,noel,npt,layer,kspt,kstep,kinc,
     2      ndi,nshr,coord,jmac,jmatyp,matlayo,laccflg)
c
        include 'aba param.inc'
c
        character*80 cmname,orname
        character*3 flgray(15)
        dimension field(nfield),statev(nstatv),direct(3,3),t(3,3),time(2)
c
        dimension array(15),jarray(15),coord(*),jmac(*),jmatyp(*)
c
c     Get strains from previous increment
```

```
      call getvrm('E',array,jarray,flgray,jrcd,
     *    jmac, jmatyp, matlayo, laccflg)
c
      statev(1) = ABS(ARRAY(1)+ARRAY(2)+ARRAY(3))
c     If error, write comment to .dat file
      IF (JRCD.NE.0) THEN
      WRITE(6,*) 'REQUEST ERROR IN USDFLD FOR ELEMENT NUMBER ',
      *
      ENDIF
c
      return
      end
```

Appendix B

Compaction of a Flanged Part: Simulation

B.1 Case 1: Compaction Using a Simple Tool Motion

An application of the developed numerical model would be to prescribe tool motions in the compaction of a powder metallurgy part with more complex geometry. The dual compaction of a flanged cylindrical part is simulated firstly using a simple tool motion with an upper punch and a single lower punch as shown by the schematic of the finite element model in Figure B.1. The material parameters used for the simulation are those determined using the test protocol for 316L stainless steel powder as prescribed in Table 7.1. To understand the motion of powder particles during compaction at the corner formed by the flange, the loading path was plotted in the $p - q$ plane for the three critical elements forming the corner as shown in the schematic.

Figure B.2(a) shows the relative density predictions in the flanged part after compaction. It can be seen that flanged section of the part has a very high density while the hub section has very low density. In such a case, there would be a very high chance of cracks developing where the flanged section meets the hub section. This is verified by the loading paths for the three critical elements as shown in Figure B.2(b) which shows that for element 1510 the loading path has crossed the shear failure surface implying that the material would undergo shear failure at that point.

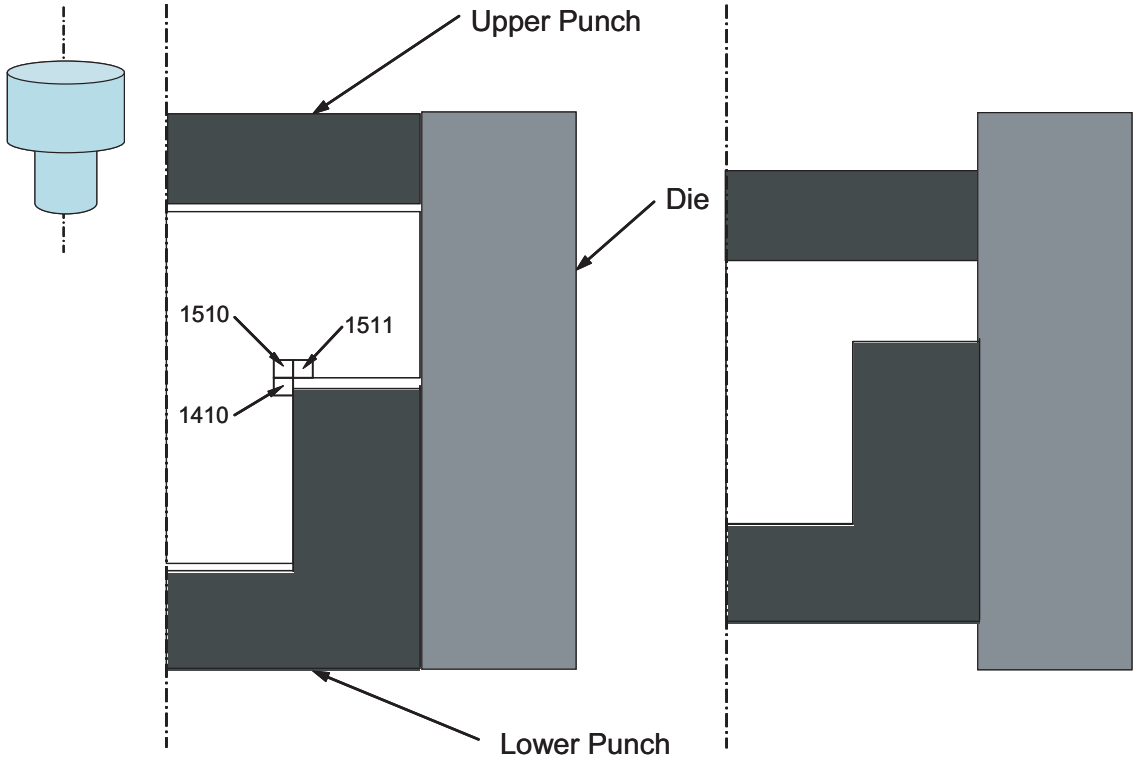

Figure B.1. Case 1: Schematic of flanged part compaction using simple tool motion

B.2 Case 2: Complex Tool Motion

In the second case, a more complex tool motion is used to compact the flanged part to a more uniform relative density. The numerical model used to simulate the more complex tool motion uses two lower punches with relative motion between them as shown by the schematic in Figure B.3. Again the material parameters used for the simulation are those determined using the test protocol for 316L stainless steel powder as prescribed in Table 7.1. The dual compaction is achieved by moving the two lower punches by different amounts in addition to the movement of the upper punch.

The results of the simulation for complex tool motion suggests a more uniform prediction in relative density distribution in the part after compaction as shown in Figure B.4(a). The

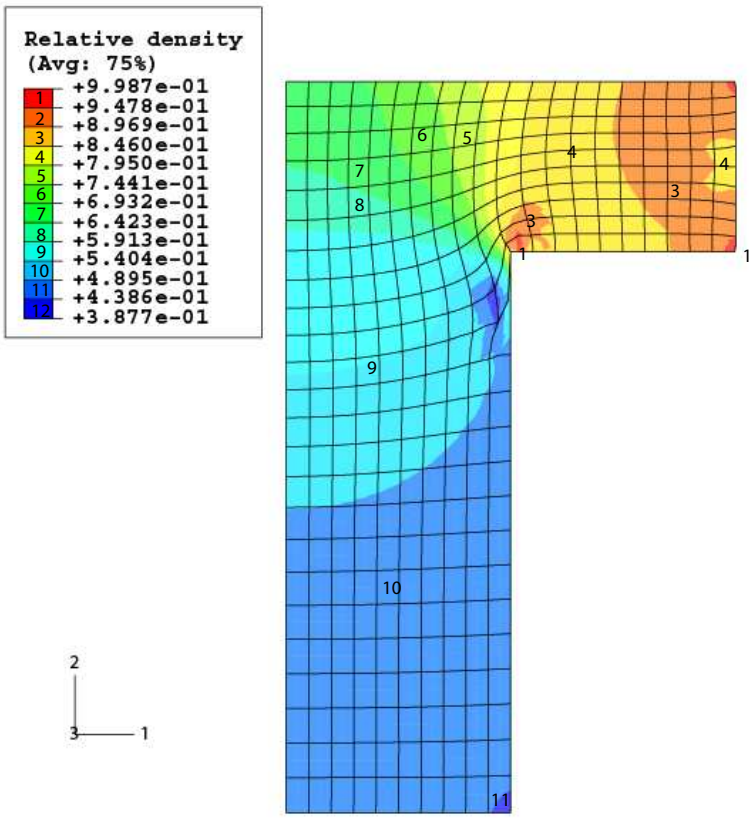

(a) Predicted relative density distribution in the flanged part

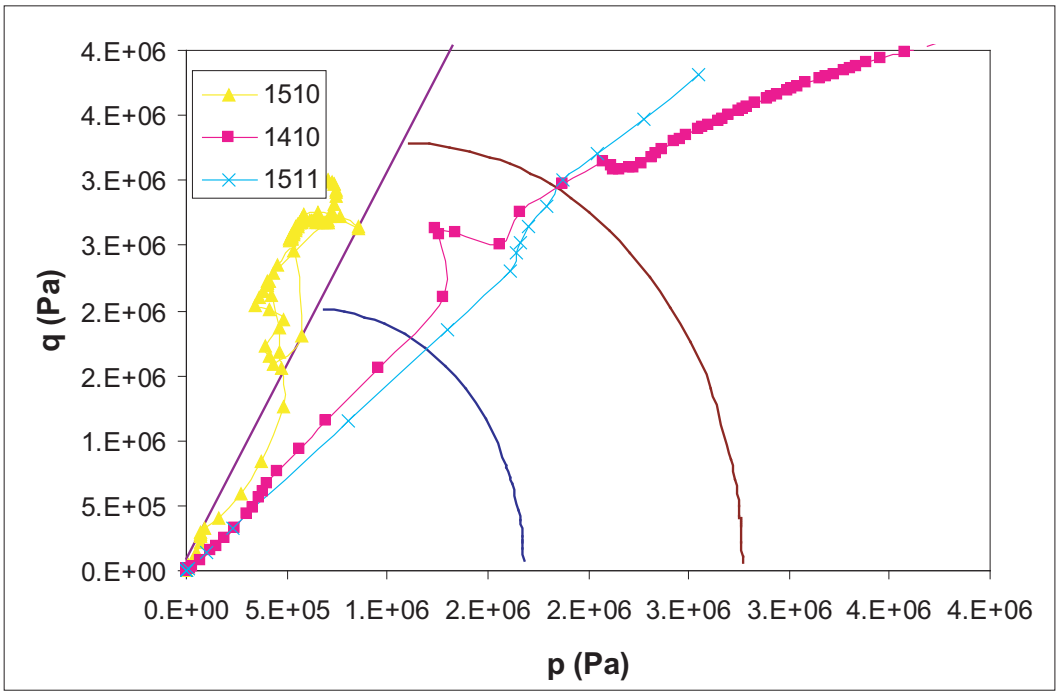

(a) Loading path for critical elements indicating shear failure at corner

Figure B.2. Case 1: Simulation results for flanged part using simple tool motion

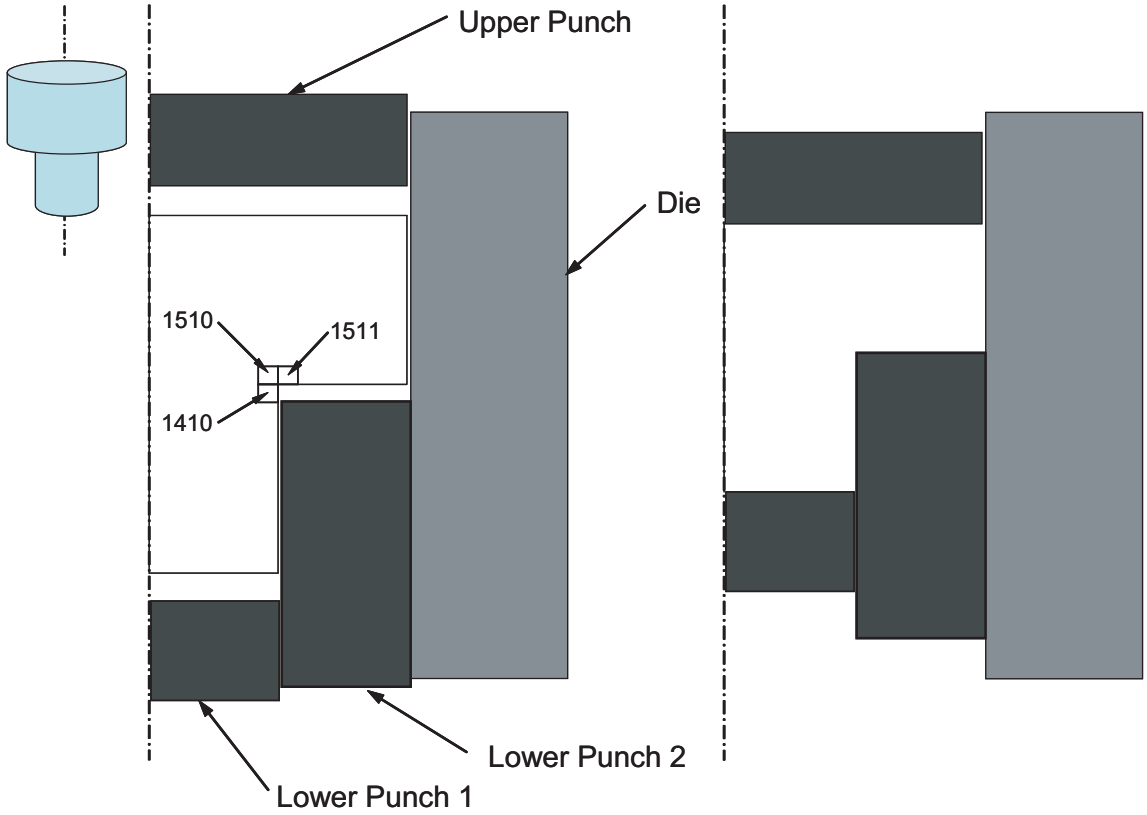

Figure B.3. Case 2: Schematic of flanged part compaction using complex tool motion

loading paths for the three critical elements shown in Figure B.4(b) show that the material at the corner is not loaded to shear failure and hence compaction of the flanged part using this tool motion would not produce any cracks in the part after compaction.

This application thus highlights the predictive capabilities of the numerical model to determine protocols for compaction of complex powder metallurgy parts using a simple material model.

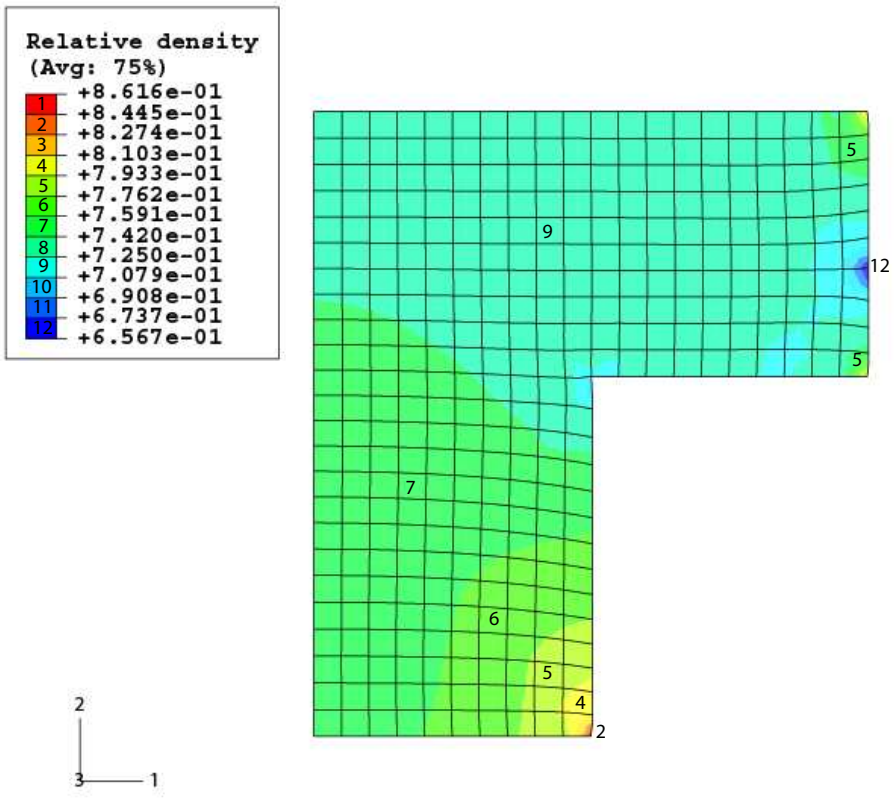

(a) Predicted relative density distribution in the flanged part

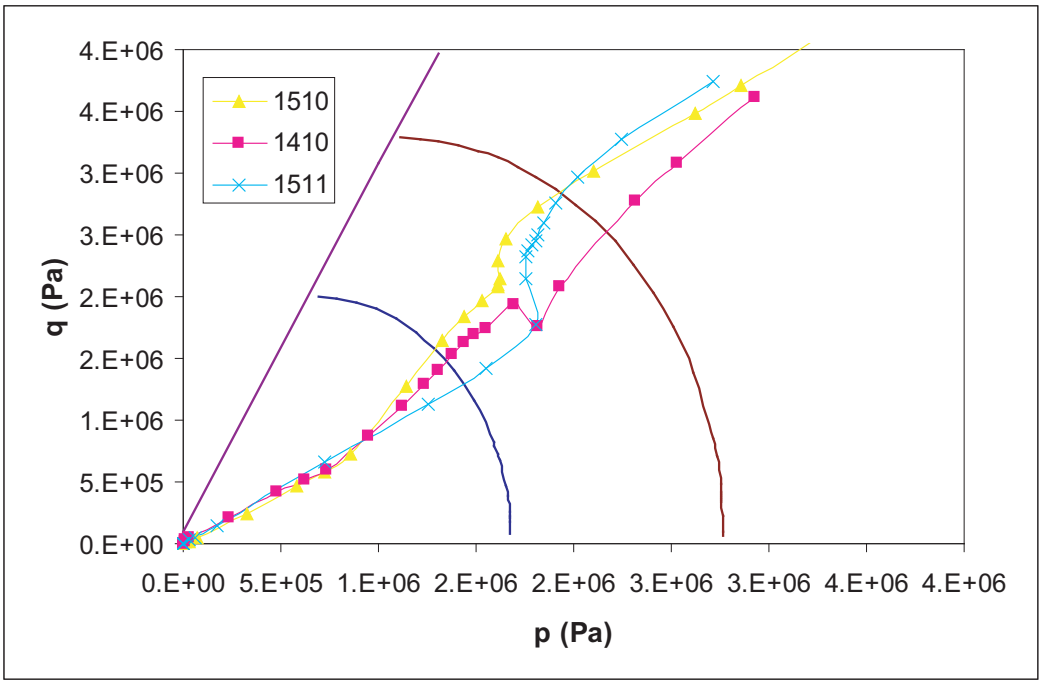

(a) Loading path for critical elements indicating shear failure at corner

Figure B.4. Case 2: Simulation results for flanged part using complex tool motion

Appendix C

NonTechnical Abstract

Powder Metallurgy is the science of manufacturing parts out of metal powders. The die compaction process is a shaping technique in powder metallurgy in which metal powder is pressed in a rigid tool cavity called the die to form a medium density weak part with loose particle bonding. To impart strength and increase density, the part is subjected to a thermal process called sintering in which the particles bond together to form the final desired part. The increase in density due to bonding of particles leads to shrinkage in this stage. During compaction, friction between the powder and the die causes the applied pressure to reduce along the die wall leading to a pressure gradient which results in a compacted part with density gradient. During the subsequent sintering of a part with density gradients, the shrinkage is non uniform and can lead to dimensional distortion. To understand the distortion it is necessary to determine the density and the density gradients formed as a result of compaction. Computer modeling of the process provides a cost-effective technique to determine the properties of the part after compaction.

Numerical modeling of a process involves mathematically quantifying the physics of the process, including the material behavior when subjected to mechanical loads. During the initial stages of compaction, the powder particles are rearranged; this is followed by permanent deformation of the particles under higher pressure as they pack together. The behavior of the particle system as the loose powder is shaped into a weak solid part is described by a material model with parameters that characterize various aspects of the response, e.g., the cohesion between particles, inter particle friction and strength of the powder material. Thus, modeling the process requires both the selection of an appropriate material

model as well as the determination of each of the models parameters. The recommended testing procedures to determine these parameters can be expensive making it difficult for industrial applications. This research looks at ways of simplifying the application of a well defined complex material model. A test procedure involving simple physical and numerical experiments has been developed to quantify the material model for commonly used metal powders. The model and the test procedure predict density and density gradient results that are in good agreement with physical measurements of density fields in compacted parts.

Vita

Gautam S Wagle

Education

B.E. (Mechanical Engineering), May 1997, V.J.T.I., University of Mumbai, India.

M.S. (Engineering Mechanics), Aug 2000, The Pennsylvania State University, University Park, PA.

Ph.D. (Engineering Science and Mechanics), Dec 2006, The Pennsylvania State University, University Park, PA.

Work Experience

Graduate Research Assistant, Engineering Science and Mechanics Dept., The Pennsylvania State University, University Park, PA, 2001 – 2005.

Angel.com Support Engineer, Microstrategy Inc., Vienna, VA, 2000 –2001.

Graduate Engineer Trainee (Preplanning Engineer), M/s Larsen & Toubro Ltd., Mumbai, India, 1997 – 1998.

Publications

Wagle, G. S., Engel, R. S., German, R. M., Bollina, R., "Statistical Analysis of Modified Drucker-Prager Cap Model Parameters for Application to Modeling Die Compaction", Advances in Powder Metallurgy and Particulate Material, vol. 1, 2003.

Wagle, G. S., Engel, R. S., Liu, Y., German, R. M., "Numerical Investigation of Constitutive Models for the Powder Compaction Process", Advances in Powder Metallurgy and Particulate Materials, vol. 1, pp. 13-24, 2000.

Lissenden, C. J., Wagle, G. S., Salamon, N. J., "Applications of Finite Element Analysis for Undergraduates", Proceedings of the 2002 ASEE Annual Conference & Exposition, Montreal, Canada, 2002.

Lissenden, C. J., Wagle, G. S., Salamon, N. J., "Design Project for Advanced Mechanics of Materials", Proceedings of the 2002 ASEE Annual Conference & Exposition, Montreal, Canada, 2002.